Final Report

Shoreline Movement and Beach and Dune Volumetrics along the Texas Gulf Coast, 1930s to 2019

Jeffrey G. Paine, Tiffany Caudle, and John R. Andrews

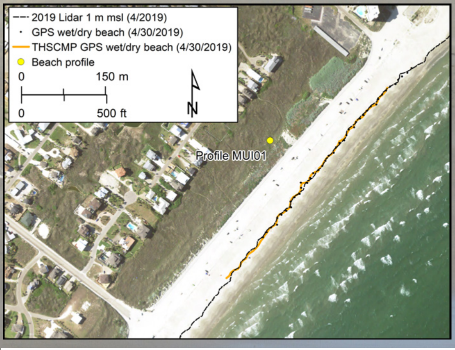

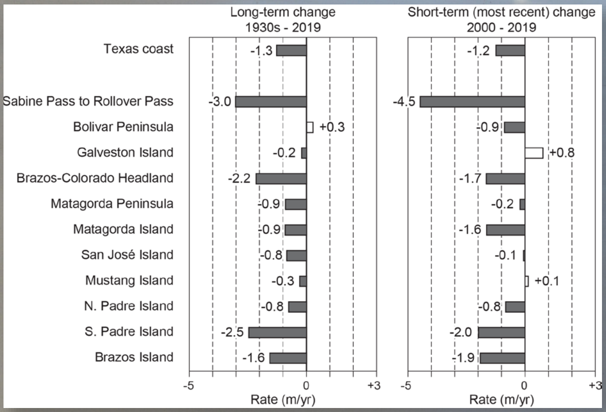

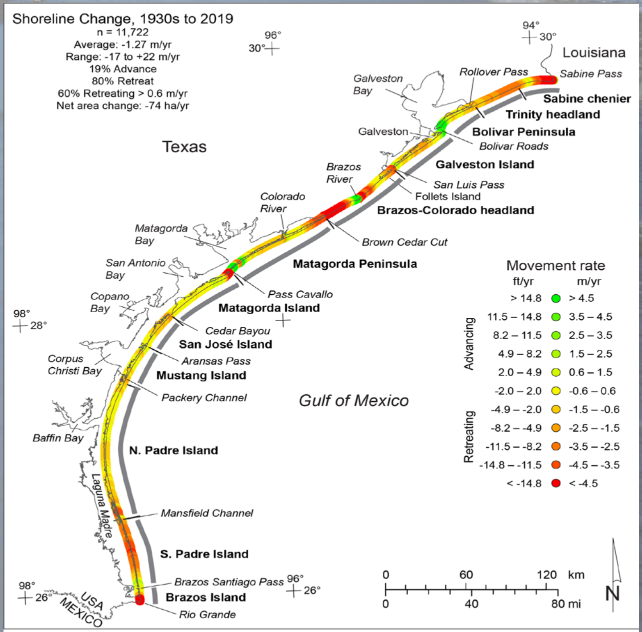

Bureau of Economic Geology
Scott W. Tinker, Director
Jackson School of Geosciences
The University of Texas at Austin
Austin, Texas 78713-8924

March 2021

Report prepared for
General Land Office under
contract no. 16-201-000,
CEPRA Project No. 1662,
Work Order No. B428.

QAe9095

Page intentionally blank

SHORELINE MOVEMENT AND BEACH AND DUNE VOLUMETRICS ALONG THE TEXAS GULF COAST, 1930s to 2019

by

Jeffrey G. Paine, Tiffany L. Caudle, and John R. Andrews

Bureau of Economic Geology
John A. and Katherine G. Jackson School of Geosciences
The University of Texas at Austin
University Station, Box X
Austin, Texas 78713

Corresponding author
jeff.paine@beg.utexas.edu
(512) 471-1260
TBPG License No. 3776

Final Report Prepared for the General Land Office
under Contract No. 16-201-000, Work Order No. B428
CEPRA Project No. 1662

March 2021

Page intentionally blank

CONTENTS

Abstract . . . vii

Introduction . . . 1

- Relative Sea Level . . . 5
- Tropical Cyclones . . . 8

Methods . . . 11

- Sources of Shorelines . . . 14
- Positional Verification . . . 19
- 2019 Volumetrics and the Landward Dune Boundary . . . 27

Texas Gulf Shoreline Movement through 2019 . . . 29

- Recent Gulf Shoreline Movement, 2000 to 2019 . . . 31
- Upper Texas Coast (Sabine Pass to San Luis Pass) . . . 35
- Brazos–Colorado Headland and Adjacent Peninsulas (San Luis Pass to Pass Cavallo) . . . 40
- Middle Texas Coast (Pass Cavallo to Packery Channel) . . . 44
- Lower Coast (Padre Island and Brazos Island) . . . 48

Late Pleistocene to Holocene Context . . . 52

Using Postglacial Rates to Predict Shoreline Movement . . . 55

Beach and Foredune Volumetrics . . . 58

- Volumetrics on the Upper Texas Coast (Sabine Pass to San Luis Pass) . . . 64
- Volumetrics along the Brazos–Colorado Headland and Adjacent Peninsulas . . . 69
- Volumetrics on the Middle Texas Coast (Pass Cavallo to Packery Channel) . . . 73
- Volumetrics on the Lower Coast (Padre Island and Brazos Island) . . . 78

Conclusions . . . 83

Acknowledgments . . . 84

References . . . 85

Appendix A: 2019 Airborne Lidar and Imagery survey . . . 91

Appendix B: Selected Nourishment and Restoration Projects . . . 95

FIGURES

1. Map of the Texas coastal zone 2
2. Sea-level trend at selected Texas tide gauges through 2019 6
3. Sea-level trend at Galveston Pier 21, 1904 to 2019 7
4. Location of 2019 Gulf shoreline, bay beach, and offshore lidar survey areas, ground GPS base stations, and shoreline position verification sites 15
5. Shoreline position comparison at Bolivar Peninsula profile BOL03 20
6. Shoreline position comparison at Galveston Island State Park site BEG02 21
7. Shoreline position comparison at Surfside Beach site SURF2 22
8. Shoreline position comparison at Matagorda Peninsula site MAT02 23
9. Shoreline position comparison at Mustang Island sites (a) MUI01 and (b) MUI03 24
10. Shoreline position comparison on southern Padre Island at site SPI 25
11. Shoreline position comparison on the upper Texas coast at Sea Rim State Park 26
12. Shoreline position comparison at Cedar Bayou on the middle Texas coast 26
13. Shoreline position comparison on the lower Texas coast at Mansfield Pass 27
14. Net rates of long-term movement for the Texas Gulf shoreline, 1930s to 2019. 30
15. Net rates of recent, short-term movement for the Texas Gulf shoreline, 2000 to 2019. . .33
16. Comparison of long-term and most recent short-term net rates of shoreline movement. .35
17. Net rates of long-term movement for the upper Texas Gulf shoreline, 1930s to 2019 . . .36
18. Net rates of recent, short-term movement for the upper Texas Gulf shoreline, 2000 to 2019 39
19. Net rates of long-term movement for the Texas Gulf shoreline from San Luis Pass to Pass Cavallo, 1930s to 2019 40
20. Net rates of recent, short-term movement for the Texas Gulf shoreline from San Luis Pass to Pass Cavallo, 2000 to 2019 43
21. Net rates of long-term movement for the middle Texas Gulf shoreline from Pass Cavallo to Packery Channel, 1930s to 2019 44
22. Net rates of recent, short-term movement for the middle Texas Gulf shoreline from Pass Cavallo to Packery Channel, 2000 to 2019 47
23. Net rates of long-term movement for the lower Texas Gulf shoreline from Packery Channel to the Rio Grande, 1930s to 2019 49

24. Net rates of recent, short-term movement for the lower Texas Gulf shoreline from Packery Channel to the Rio Grande, 2000 to 2019 51

25. Postglacial Gulf of Mexico sea-level curves 52

26. Major bathymetric contours on the Texas continental shelf and transect locations. 53

27. Relationship between postglacial rates of relative sea-level rise and approximate long-term shoreline retreat rates 56

28. Peak beach and foredune elevation along the Texas Gulf shoreline, 2019 59

29. Percentage of the Texas Gulf shoreline having peak beach and foredune elevations above threshold elevations ranging from 1 to 9 m. 60

30. Normalized beach and foredune volume above 1 m elevation for the Texas Gulf shoreline. 61

31. Normalized beach and foredune volume above 1 to 9 m elevation for the Texas Gulf shoreline and for major coastal segments.. 62

32. Peak beach and foredune elevation along the upper Texas coast, 2019 64

33. Percentage of the upper Texas coast shoreline having peak beach and foredune elevations above threshold elevations ranging from 1 to 9 m 66

34. Normalized beach and foredune volume above 1 m elevation along the upper Texas coast 67

35. Normalized beach and foredune volume above 1 to 9 m elevation on the upper Texas coast 68

36. Peak beach and foredune elevation between San Luis Pass and Pass Cavallo, 2019 69

37. Percentage of the shoreline between San Luis Pass and Pass Cavallo having peak beach and foredune elevations above threshold elevations ranging from 1 to 9 m 70

38. Normalized beach and foredune volume above 1 m elevation between San Luis Pass and Pass Cavallo 71

39. Normalized beach and foredune volume above 1 to 9 m elevation between San Luis Pass and Pass Cavallo 72

40. Peak beach and foredune elevation along the middle Texas coast, 2019 73

41. Percentage of the middle Texas coast shoreline having peak beach and foredune elevations above threshold elevations ranging from 1 to 9 m 75

42. Normalized beach and foredune volume above 1 m elevation along the middle Texas coast 76

43. Normalized beach and foredune volume above 1 to 9 m elevation on the middle Texas coast 77

44. Peak beach and foredune elevation along the lower Texas coast, 2019 79

45. Percentage of the lower Texas coast shoreline having peak beach and foredune elevations above threshold elevations ranging from 1 to 9 m 80

46. Normalized beach and foredune volume above 1 m elevation on the lower Texas coast . 81

47. Normalized beach and foredune volume above 1 to 9 m elevation on the lower Texas coast 82

A1. The Bureau's Chiroptera airborne lidar and imagery system 91

B1. Locations of beach nourishment and dune restoration projects on the upper Texas coast 98

B2. Locations of beach nourishment and dune restoration projects between San Luis Pass and Pass Cavallo 99

B3. Locations of beach nourishment and dune restoration projects on the middle Texas coast 100

B4. Locations of beach nourishment and dune restoration projects on the lower Texas coast 101

TABLES

1. Long-term rates of relative sea-level rise at select Texas tide gauges through 2018. 7

2. Tropical cyclones affecting the Texas coast between 1990 and 2020 10

3. Shoreline source dates and types used to calculate shoreline movement rates 13

4. Net shoreline and land-area change between the 1930s and 2019 for the Texas Gulf shoreline and major geomorphic areas 31

5. Net shoreline and land-area change between 2000 and 2019 for the Texas Gulf shoreline and major geomorphic areas 34

6. Late Pleistocene and Holocene net shoreline retreat rates for the Texas coast 54

7. Estimated total volume in the beach and foredune system above threshold elevations between 1 and 9 m 63

A1. Flight dates, survey areas flown, and GPS base stations used for the 2019 airborne lidar survey of the Texas coast 93

B1. Partial list of beach nourishment, dune restoration, and nearshore dredge material placement projects along the Texas Gulf of Mexico shoreline 95

ABSTRACT

Long-term rates of Gulf shoreline movement along the Texas coast have been determined through 2019 from a series of shoreline positions that includes those depicted on aerial photographs from the 1930s to 2007, ground GPS surveys from the 1990s, and airborne lidar surveys in 2000, 2012, and 2019. Net rates of long-term shoreline movement measured at 11,722 sites spaced at 50 m (164 ft) along the 590 km (367 mi) of Texas shoreline fronting the Gulf of Mexico average 1.27 m/yr (4.2 ft/yr) of retreat. Net shoreline retreat occurred along 80 percent of the Texas Gulf shoreline, resulting in an estimated net land loss of 6,627 ha (16,375 ac) since 1930 at an average rate of 74 ha/yr (184 ac/yr). Average rates of movement are more recessional on the upper Texas coast (net retreat at 1.71 m/yr [5.6 ft/yr] from Sabine Pass to the Colorado River) than they are on the middle and lower coast (net retreat at 0.97 m/yr [3.2 ft/yr] from the Colorado River to the Rio Grande).

Areas undergoing significant net retreat include: (1) the muddy marshes on the upper Texas coast between Sabine Pass and High Island; (2) segments on the sandy barrier-island shoreline on Galveston Island; (3) most of the combined fluvial and deltaic headland constructed by the Brazos and Colorado rivers; (4) sandy, headland-flanking barriers northeast (Follets Island) and southwest (Matagorda Peninsula) of the Brazos–Colorado headland; (5) San José Island, a sandy barrier island on the middle Texas coast; (6) the northern end and much of the southern half of Padre Island, a sandy barrier island on the lower coast; and (7) the sandy Brazos Island barrier peninsula and the Rio Grande fluvial and deltaic headland. Significant net shoreline advance occurred in more limited areas (1) adjacent to the jetties that protect dredged channels at Sabine Pass, Bolivar Roads, Aransas Pass, and Brazos Santiago Pass; (2) near tidal inlets at the western ends of Galveston Island and Matagorda Peninsula; (3) southwest of the mouth of the Brazos River; (4) along part of Matagorda Island; and (5) on central Padre Island.

Shoreline change rates measured for the most recent short-term period (2000 to 2019) are similar to those calculated for the longer period (1930s to 2019), averaging 1.25 m/yr (4.1 ft/yr) of net retreat. These rates are significantly lower than late Pleistocene to early Holocene rates that range from 3 to 55 m/yr (8 to 181 ft/yr) estimated from bathymetric contour shoreline proxies and past sea-level positions, but are similar to mid- to late Holocene retreat rates of 0.1 to 1.7 m/yr (0.4 to 5.4 ft/yr). A statistical relationship between postglacial relative sea-level rise rates and retreat

rates calculated from the bathymetric shoreline proxy suggests that each millimeter per year of sea-level rise translates to 0.8 to 1.8 m/yr (3 to 6 ft/yr) of shoreline retreat. This relationship provides an empirical approach to estimating future shoreline retreat rates under sea-level rise scenarios that may be similar to those observed during postglacial sea-level rise.

Elevations and sediment volumes in the beach and foredune corridor determined from the 2019 airborne lidar survey generally correlate well with shoreline movement trends. Rapidly retreating shoreline segments have lower peak beach and foredune elevations than do segments where shorelines are more stable or advancing. Peak beach and foredune elevations are below 4.5 m (15 ft) elevation along nearly 50 percent of the Texas Gulf shoreline and are below 3 m (10 ft) elevation along about 20 percent of the shoreline. Areas of very low peak beach and foredune elevations and low sediment volumes above 1 m (3.3 ft) elevation include the Sabine chenier and Trinity headland on the upper Texas coast, the Brazos–Colorado headland, and parts of Matagorda Peninsula and Matagorda Island. Beach and foredune sediment volume above 1 m (3.3 ft) elevation is estimated to be nearly 133,000,000 m^3 (174,000,000 yd^3) along the Texas Gulf shoreline, of which more than half is on Padre Island. Peak elevations and volumes above various threshold elevations can be used to identify shoreline segments where little sediment is available to offset sediment lost by erosion and segments vulnerable to breaching and washover during storm surge associated with tropical cyclone passage.

Shoreline change rates and beach and foredune elevation and volumetric statistics were calculated using the latest coast-wide airborne lidar data and imagery acquired in spring 2019. Updated rates and elevation and volume statistics include the effects (erosion, deposition, and nearly two years of recovery) associated with Hurricane Harvey, which struck the middle Texas coast in August 2017 and strongly impacted beach and dune morphology from Mustang Island to the Brazos–Colorado headland. Tropical cyclones affecting the Texas coast since the 2019 survey include Tropical Storm Imelda in 2019 and Tropical Storm Beta, Hurricane Hanna, and Hurricane Laura in 2020.

INTRODUCTION

The Texas coastal zone (fig. 1) is among the most dynamic geologic environments on earth. Shoreline position is a critical parameter that reflects the balance among several important processes, including sea-level rise, land subsidence, sediment influx, littoral drift, and storm frequency, intensity, and recovery. Because the Texas coast faces ongoing developmental pressures as the coastal population grows, an accurate and frequent analysis of shoreline movement serves as a planning tool to identify areas of habitat loss, better quantify threats to residential, industrial, and recreational facilities and transportation infrastructure, and help understand the natural and anthropogenic causes of shoreline movement.

The Texas Gulf shoreline forms the seaward boundary along a series of Holocene geomorphic features (fig. 1) that include barrier islands, strandplains, fluvial and deltaic headlands, and chenier plains (Aronow and others, 1982; Brown, Brewton, and McGowen, 1975; Brown and others, 1975, 1976; LeBlanc and Hodgson, 1959). Three major rivers, including the Brazos and Colorado on the upper (northeastern) Texas coast and the Rio Grande on the lower (southern) Texas coast, directly discharge into the Gulf of Mexico, although their contribution to the overall coastal sediment budget has diminished with the construction of dams for flood control, water supply, and recreation in each river basin in the 20th century. Coastal embayments such as Galveston Bay formed landward of the Holocene barrier islands and peninsulas in late Pleistocene river valleys submerged during the Holocene transgression (LeBlanc and Hodgson, 1959), and shore-parallel lagoons such as Laguna Madre and eastern Matagorda Bay formed as barrier islands and peninsulas aggraded and expanded laterally along the coast. Tidal exchange between the bays, lagoons, and the Gulf of Mexico occurs through tidal passes and channels at Sabine Pass, Rollover Pass (closed in 2019-2020), Bolivar Roads, San Luis Pass, Brown Cedar Cut, Pass Cavallo, Cedar Bayou, Aransas Pass, Packery Channel, Mansfield Channel, and Brazos Santiago Pass (fig. 1). Prevailing onshore, southeasterly winds generate littoral currents in the northwestern Gulf of Mexico that carry sediments toward a longshore convergence zone along

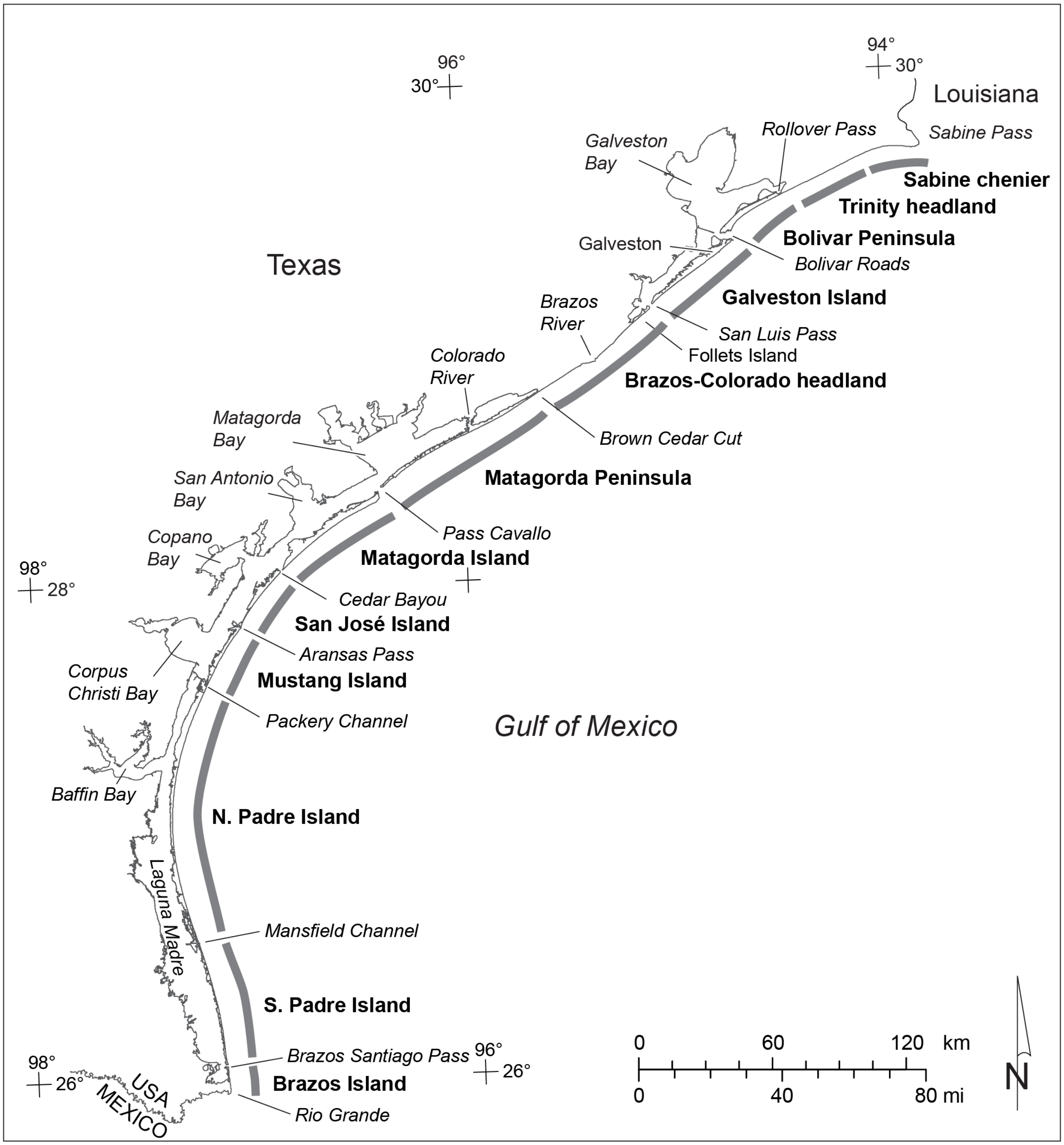

Figure 1. Map of the Texas coastal zone showing principal geomorphic features (bold) and coastal counties. Shaded segments parallel to the shoreline indicate the approximate extent of major barrier islands, peninsulas, fluvial and deltaic headlands, and strandplains.

Padre Island between the Rio Grande deltaic headland to the south and the Brazos–Colorado headland to the northeast. Similarly, a smaller convergence zone occupies the embayment between the Brazos–Colorado headland and the Trinity headland along the upper Texas coast.

The latest trends in shoreline change rates are a critical component in understanding the potential impact that sea level, subsidence, sediment supply, and coastal engineering projects have on the coastal population and sensitive coastal environments such as beaches, dunes, and wetlands. Rapidly eroding shorelines threaten habitat and recreational, residential, transportation, and industrial infrastructure and can also significantly increase the vulnerability of communities to tropical storms. Periodic analyses of shoreline position, rates of movement, and factors contributing to shoreline change give citizens, organizations, planners, and regulators an indication of expected future change and help determine whether those changes are accelerating, decelerating, or continuing at the same rate as past changes.

Historical change rates for the Texas Gulf shoreline were first determined by the Bureau of Economic Geology (Bureau) in the 1970s and presented in a series of publications separated at natural boundaries along the 590 km (367 mi) shoreline (Morton, 1974, 1975, 1977; Morton and Pieper, 1975a, 1975b, 1976, 1977a, 1977b; Morton and others, 1976). This publication series presented net long-term change rates determined from shoreline positions documented on 1850 to 1882 topographic charts published by the U.S. Coast and Geodetic Survey (Shalowitz, 1964) and aerial photographs acquired between about 1930 and 1975. Rates of change for the entire Gulf shoreline were updated through 1982 based on aerial photographs (Paine and Morton, 1989; Morton and Paine, 1990). Updates for subsets of the Texas Gulf coast include the upper coast between Sabine Pass and the Brazos River through 1996 (Morton, 1997), the Brazos River to Pass Cavallo (Gibeaut and others, 2000) and Mustang and northern Padre Island through 2000 (Gibeaut and others, 2001). Shoreline positions in 2000–2001, established using an airborne lidar topographic mapping system, were used in Bureau studies and as part of a Gulf-wide assessment of shoreline change that included the Texas coast (Morton and others, 2004). Coast-wide rates of historical shoreline change were updated using 2007 aerial photographs, the most recent coast-wide coverage predating Hurricane Ike in 2008 (Paine and others, 2011, 2012). Short-term shoreline movement, and its relationship to long-term trends, was determined from annual shoreline positions extracted from airborne lidar surveys conducted in 2010, 2011, and 2012 (Paine and others, 2013, 2017). The most recent update to historical Texas Gulf shoreline change rates used shoreline positions extracted from the 2012 airborne lidar survey (Paine and others, 2014).

This report describes the 2019 update to long- and short-term shoreline movement rates that are published as a GIS data set and displayed online on the Bureau's interactive shoreline movement web viewer (https://coastal.beg.utexas.edu/shorelinechange2019/), the latest update to the Bureau's long-term Texas Shoreline Change Project series (http://www.beg.utexas.edu/research/programs/coastal/the-texas-shoreline-change-project). These rates were calculated from selected shoreline vintages that began in most areas with the 1930s aerial photographs and included ground-based GPS surveys conducted in select areas during the mid-1990s and coast-wide airborne lidar surveys acquired in 2000, 2012, and 2019. For the lidar surveys, we use a carefully chosen elevation contour extracted from digital elevation models (DEMs) as the shoreline proxy that best matches the wet-beach/dry-beach shoreline position interpreted from aerial photographs. For this most current shoreline change update, we used airborne lidar survey data acquired by the Bureau in April to June 2019. Shorelines extracted from the 2019 lidar data represent conditions 20 to 22 months after Hurricane Harvey, a major tropical cyclone that made landfall on the middle Texas coast in late August 2017. Tropical Storm Imelda made landfall in September 2019 after the 2019 lidar survey was completed and is not included in this analysis of shoreline movement.

Relative Sea Level

Changes in sea level relative to the ground surface have long been recognized as a major contributor to shoreline change (*e.g.* Bruun, 1954, 1962, 1988; Cooper and Pilkey, 2004). Rising sea level inundates low-relief coastal lands causing shoreline retreat by submergence, and elevates dynamic coastal processes (currents and waves) that can accelerate shoreline retreat by physical erosion. Changes in relative sea level include both changes in the ocean-surface elevation ("eustatic" sea level) and changes in the elevation of the ground caused by subsidence or uplift. Eustatic sea-level change rates, established by monitoring average sea level at long-record tide gauge stations around the world and more recently using satellite altimetry, vary over a range of about 1 to 4 mm/yr. Gutenberg (1941) calculated a eustatic rate of 1.1 mm/yr from tide gauge data. Estimates based on tide gauge data since then have ranged from 1.0 to 1.7 mm/yr (Gornitz and others, 1982; Barnett, 1983; Gornitz and Lebedeff, 1987; Church and White, 2006), although Emery (1980) supported a higher global average of 3.0 mm/yr that is comparable to more recent globally averaged rates based on satellite altimetry. Attempts to remove postglacial isostatic uplift or subsidence and geographical bias from historical tide gauge records resulted in eustatic estimates as high as 2.4 mm/yr (Peltier and Tushingham, 1989). Recent studies that include satellite altimetry data acquired since 1993 indicate that global rates of sea-level rise average 2.8 mm/yr to 3.3 mm/yr with postglacial rebound removed (Cazenave and Nerem, 2004; Leuliette and Willis, 2011; Church and White, 2011; Church and others, 2013; Cazenave and others, 2014). Much of this recent rise is interpreted to result from thermal expansion of the oceans with a possible contribution from melting of glaciers and polar ice (Cazenave and Nerem, 2004; FitzGerald and others, 2008; Leuliette and Miller, 2009). The most recent analyses of satellite-based radar altimetry data interpret a 0.08 mm/yr^2 acceleration in sea-level rise rate since 1993 (Nerem and others, 2018).

In major sedimentary basins such as the northwestern Gulf of Mexico, eustatic sea level rise is exacerbated by subsidence. Published rates of relative sea-level rise measured at tide gauges along the Texas coast are higher than eustatic sea-level rates (Swanson and Thurlow, 1973; Lyles and others, 1988; Penland and Ramsey, 1990; Paine, 1991, 1993). The most recent relative sea-level rise rates from selected Texas tide gauges range from 3.60 to 6.55 mm/yr (fig. 2; table 1). These rates were calculated from data acquired by the National Oceanic and Atmospheric

Administration through 2019 from periods of record that begin between 1904 (Galveston Pier 21) and 1983 (Corpus Christi). The highest rates (above 4 mm/yr) are calculated for upper and middle Texas coast tide gauges at Sabine Pass, Galveston, Freeport, Rockport, and Corpus Christi. The southernmost gauges have the lowest long-term rates of 3.60 at Port Mansfield and 4.10 mm/yr at Port Isabel.

Galveston Pier 21 has the longest period of record on the Texas coast. Long-term rate of sea-level rise calculated from monthly averages of sea level between 1904 and 2019 (fig. 3) is 6.55 mm/yr. Sea-level rise at this gauge has not been constant; calculations of average rate of change over a rolling 19-year window (chosen to match the duration of the 19-year National Tidal Datum Epoch and centered on the mid-date) show multiyear oscillations in average rate that range from

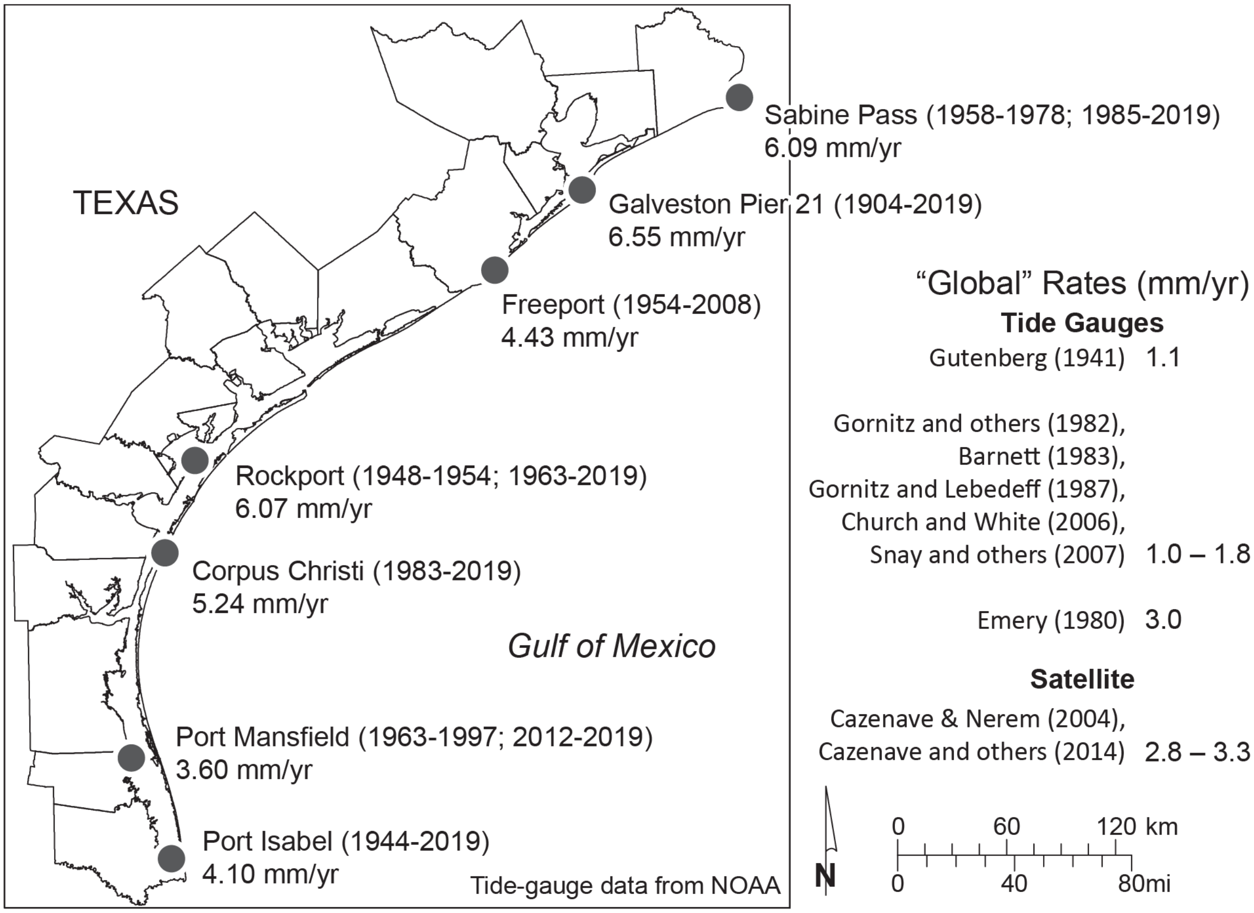

Figure 2. Sea-level trend at selected Texas tide gauges through 2019 and "global" rates determined from tide-gauge and satellite data. Texas tide-gauge data from National Oceanic and Atmospheric Administration.

Table 1. Long-term rates of relative sea-level rise at select Texas tide gauges (fig. 2) through 2018. Data from National Oceanic and Atmospheric Administration.

Tide gauge	**Beginning year**	**Duration (yr)**	**Rate (mm/yr)**	**95% confidence interval (+/-, mm/yr)**
Sabine Pass	1958	60	5.86	0.74
Galveston Pier 21	1904	114	6.51	0.22
Galveston Pleasure Pier (removed 2011)	1957	54	6.62	0.69
Freeport (removed 2008)	1954	54	4.43	1.05
Rockport	1937	81	5.62	0.48
Port Mansfield	1963	55	3.19	0.73
Padre Island (through 2006)	1958	48	3.48	0.75
Port Isabel	1944	74	4.00	0.33

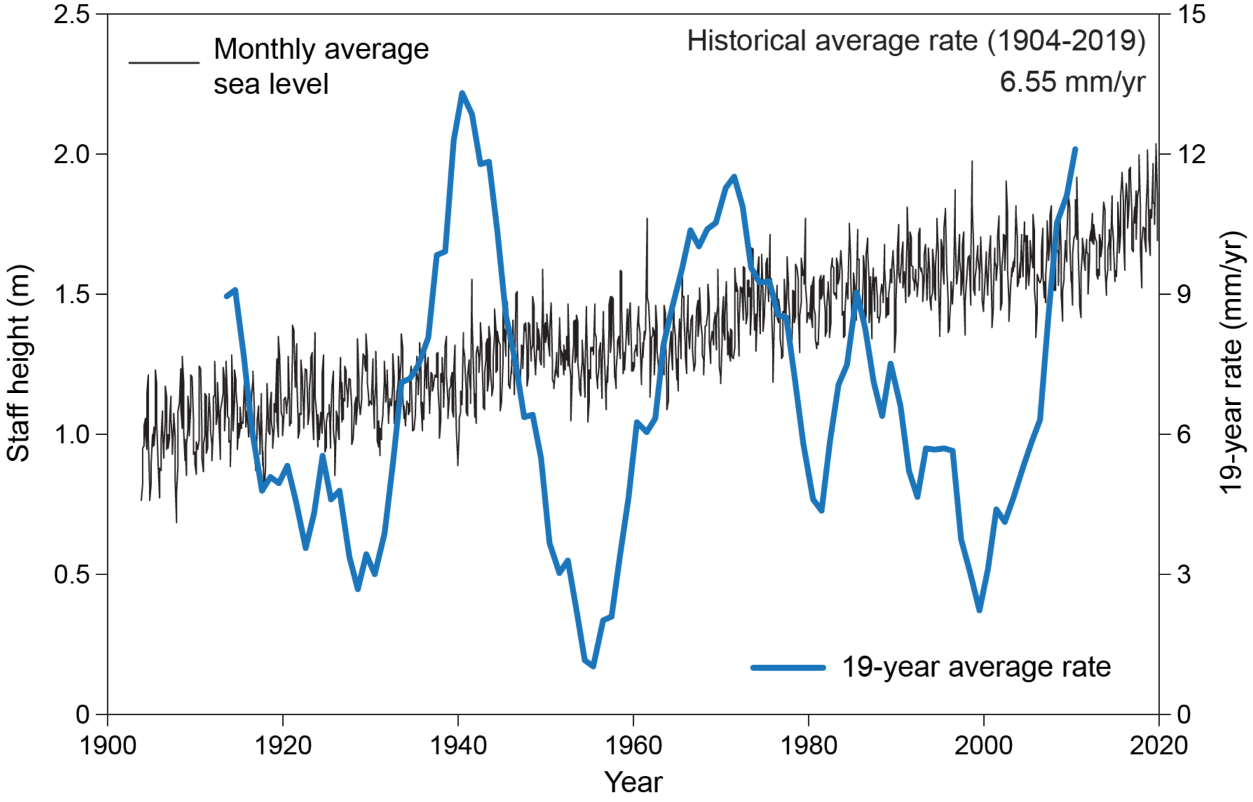

Figure 3. Sea-level trend at Galveston Pier 21, 1904 to 2019. Thin black line is monthly average sea level. Thick blue line is the average sea level change rate measured over a 19-year period (the tidal datum epoch) and plotted at the center date of the period. Data from National Oceanic and Atmospheric Administration.

1.0 to 13.3 mm/yr (fig. 3). Most recently, average rates (since about 2000) have increased from 2.2 to 12.1 mm/yr.

Tide-gauge data represent single points along the coast and may not be representative of relative sea-level rise along the entire coast. Geodetic releveling data obtained from the National Geodetic Survey at benchmarks along the Texas coast from Galveston Bay to the Rio Grande show local variation in subsidence rates that would produce average rates of relative sea-level rise ranging from about 2 to more than 20 mm/yr. These rates are significantly higher than both the estimated long-term subsidence rate of 0.05 mm/yr or less since the last interglacial at about 100 ka (Paine, 1993) and global sea-level rise estimates, but are lower than average rates of postglacial sea-level rise during the early to middle Holocene (Shepard, 1960; Balsillie and Donoghue, 2004; Milliken and others, 2008; Paine and others, 2012). Despite the wide range in estimated subsidence rates, most of the rates fall within the range observed for the long-term Texas tide gauges, suggesting that the gauges are representative regional indicators of relative sea-level rise.

Tropical Cyclones

There are numerous examples of the significant impact that tropical cyclones (tropical storms and hurricanes) have on the Texas Gulf shoreline (*e.g.* Price, 1956; Hayes, 1967; Morton and Paine, 1985). Cyclones include tropical storms (sustained winds between 62 and 118 km/hr, or 39 and 73 mi/hr) and hurricanes that are classified following the Saffir/Simpson system (Simpson and Riehl, 1981). Category 1 hurricanes have sustained winds of 119 to 153 km/hr (74 to 95 mi/hr); Category 2: 154 to 177 km/hr (96 to 110 mi/hr); Category 3: 178 to 208 km/hr (111 to 129 mi/hr); Category 4: 209 to 251 km/hr (130 to 156 mi/hr); and Category 5: greater than 252 km/hr (157 mi/hr). In general, minimum central pressure decreases and pressure- and wind-driven storm surge increases as the categories increase. Two critical parameters that influence the erosion potential of a tropical cyclone are surge height and surge duration: the longer sea level is elevated above normal during storm passage, the greater the potential for redistribution of sediment eroded from the beach. Beach and dune recovery after storm passage follows several distinct stages and can extend beyond two years after storm landfall (Morton and Paine, 1985; Morton and others, 1994). The ending date (2019) for this update of shoreline change rates allowed nearly eleven years for recovery from Hurricane Ike (2008), which was a large Category 2 storm that severely eroded upper Texas coast beaches and dunes, and nearly two years for recovery from Hurricane Harvey (2017), a Category 4 storm that made landfall on the middle Texas coast. Tropical Storm Imelda made landfall near Freeport in September 2019, three months after the 2019 airborne lidar survey was completed for this update. Three tropical cyclones affected the Texas coast during the extremely active 2020 hurricane season, including Hurricane Hanna, a Category 1 hurricane that made landfall on central Padre Island in July 2020, Hurricane Laura, a Category 4 hurricane that made landfall in southwestern Louisiana in August 2020, and Tropical Storm Beta, which made landfall on Matagorda Peninsula in September 2020.

Historical lists (Roth, 2010) and records maintained by the National Oceanic and Atmospheric Administration indicate that 66 hurricanes and 63 tropical storms have struck the Texas coast from 1850 through 2020. On average, four hurricanes and four tropical storms make landfall in Texas per decade. The longest hurricane-free period in Texas extended nearly 10 years from October 1989 to August 1999 (Roth, 2010).

From 1990 through 2018, the period most applicable to this update (Tropical Storm Imelda made landfall in September 2019, after the 2019 lidar survey), 21 tropical cyclones crossed the Texas coast (table 2). Included are 14 tropical storms and 7 hurricanes that ranged in strength from Category 1 to Category 4 at landfall. Only 1 hurricane and 4 tropical storms affected Texas during the 1990s. From 2000 to 2018, there were 6 hurricanes and 10 tropical storms, a combined cyclone frequency that is slightly higher than the historical average. Storm frequency was higher between 2000 and 2009 (5 hurricanes and 6 tropical storms) than it was between 2010 and 2018 (1 hurricane and 4 tropical storms). The most severe storms in the last two decades were Hurricanes Bret, Rita, Ike, and Harvey. Hurricane Bret was a former Category

Table 2. Tropical cyclones affecting the Texas coast since 1990. TD = tropical depression; TS = tropical storm; H = hurricane; number following H designates numeric strength according to the Saffir/Simpson scale (Simpson and Riehl, 1981). Data from the National Oceanic and Atmospheric Administration and Roth (2010).

Year	Category	Name	Begin date	End date	Landfall
1993	TS	Arlene	6/18/1993	6/21/1993	Northern Padre Island
1995	TS	Dean	7/28/1995	8/2/1995	Freeport
1998	TS	Charley	8/21/1998	8/24/1998	Aransas Pass
1998	TS	Frances	9/8/1998	9/13/1998	Matagorda Island
1999	H4	Bret	8/18/1999	8/25/1999	Padre Island (weakened)
2001	TS	Allison	6/5/2001	6/17/2001	Freeport
2002	TS	Bertha	8/4/2002	8/9/2002	Northern Padre Island
2002	TS	Fay	9/5/2002	9/8/2002	Matagorda Peninsula
2003	H1	Claudette	7/8/2003	7/17/2003	Matagorda Peninsula
2003	TS	Grace	8/30/2003	9/2/2003	Galveston Island
2005	H5	Rita	9/18/2005	9/26/2005	Sabine Pass (H3 at landfall)
2007	TS	Erin	8/15/2007	8/17/2007	San José Island
2007	H1	Humberto	9/12/2007	9/14/2007	Upper Texas coast
2008	H2	Dolly	7/20/2008	7/25/2008	Southern Padre Island
2008	TS	Edouard	8/3/2008	8/6/2008	Upper Texas coast
2008	H4	Ike	9/1/2008	9/15/2008	Galveston (H2 at landfall)
2010	TS	Hermine	9/5/2010	9/9/2010	Rio Grande area
2011	TS	Don	7/27/2011	7/29/2011	Baffin Bay area (TD at landfall)
2015	TS	Bill	6/15/2015	6/16/2015	Matagorda Island
2017	TS	Cindy	6/20/2017	6/23/2017	Port Arthur to Cameron, LA
2017	H4	Harvey	8/17/2017	9/1/2017	Rockport area
2019	TS	Imelda	9/17/2019	9/19/2019	Freeport area
2020	H1	Hanna	7/23/2020	7/27/2020	Padre Island
2020	H4	Laura	8/20/2020	8/28/2020	Southwestern LA
2020	TS	Beta	9/17/2020	9/22/2020	Matagorda Peninsula

4 storm that weakened before landfall on Padre Island in August 1999. Hurricane Rita was a Category 5 storm that weakened to Category 3 before landfall in the Sabine Pass area in September 2005. Hurricane Ike was a Category 4 storm that weakened to a very large Category 2 storm before landfall in September 2008. It produced an unusually high and long-duration storm surge that heavily impacted upper Texas coast beaches. Hurricane Harvey rapidly intensified to Category 4 as it approached the middle Texas coast before making landfall near Rockport on

August 25, 2017 (Blake and Zelinsky, 2018). Hurricane Harvey is the most recent storm prior to the shoreline position considered in this update, making landfall 20 to 22 months before the 2019 airborne lidar survey of the Texas Gulf shoreline.

METHODS

Shoreline change rates were calculated after including the 2019 lidar- and imagery-derived shoreline position into the set of shoreline positions that has been used to determine long-term Texas Gulf shoreline change rates presented in the Bureau's shoreline change publication series. Shoreline vintages were selected for change-rate analysis to conform with shorelines chosen for earlier calculations of shoreline change rate and to result in reasonably regular intervals between shorelines along a given transect. Shoreline rates presented in the publications before 2000 were listed as net, or average, rates of change between two end-point dates (the net distance the shoreline moved divided by the elapsed time). More recently, rates have also been calculated using linear regression analysis of all included shoreline positions. In the 2019 update, we present both rates in the data files and on the web viewer, but discuss net values in this report for historical consistency. In most cases, these rates are similar and either rate could be used.

Shoreline change rates were calculated following several steps, including:

(1) importing the 2019 shoreline position (extracted as a carefully chosen elevation contour from a 1-m resolution digital elevation model constructed from high-resolution lidar data) into a geographic information system data base (ArcMap, v. 10.4);

(2) checking the consistency of the chosen elevation contour with the position of the wet- and dry-beach boundary as depicted on 2016 and 2018 National Agricultural Imagery Program (NAIP) georeferenced aerial photographs and 2019 Bureau aerial imagery;

(3) selecting the shoreline vintages to use in the calculation of change rates (table 3), which include the earliest photograph-derived shoreline from the 1930s Tobin aerial photographs

along with geographically extensive coastal photography from the 1950s, 1960s, 1974, 1990s, and 2007; GPS-derived shoreline positions from 1996 and 1998; and shoreline positions from airborne lidar surveys conducted by the Bureau in 2000, 2012, and 2019;

(4) creating shore-parallel baselines from which shore-perpendicular transects were cast at 50-m intervals along the shoreline using the GIS-based extension software Digital Shoreline Analysis System version 5.0 (DSAS; Himmelstoss and others, 2018);

(5) calculating rates of change and associated statistics for the long-term (1930s to 2019), medium-term (1950s to 2019) and most recent short-term (2000 to 2019) periods using the transect locations and the selected shorelines within DSAS; and

(6) determining the intersection of the transect lines with the 2019 shoreline and creating GIS shape files containing (a) the rates and statistics of shoreline change measurements and (b) the measurement transects bounded by the most landward and seaward historical shoreline position for each measurement site (the shoreline change envelope).

Rates were calculated as both net (average) rates and linear-regression rates. For consistency with previous studies, only net rates are discussed in this report and displayed graphically on the accompanying web viewer. For comparison purposes, both net rates and linear-regression rates (and coefficients of determination) are shown for web viewer queries and in the accompanying GIS data set. Where regression coefficients of determination are relatively high (closer to 1.0), rates calculated using the linear regression method reasonably express the movement of the shoreline. Where coefficients are low (closer to 0), regression rates do not reasonably reflect the movement of the shoreline, perhaps because of inconsistent movement rates over time, including possible reversals of movement direction. Net rates, calculated as the distance between the shoreline position at the end and beginning of the monitoring period, divided by elapsed time, are analyzed for multiple periods (1930s to 2019, 1950s to 2019, and 2000 to 2019) to examine potential changes in movement rates over time.

Table 3. Shoreline source dates and types used to calculate shoreline movement rates for each major Gulf of Mexico coastal segment. The 1930s to 1991 shorelines were mapped on aerial photographs, optically transferred to paper topographic maps, and digitized into a GIS database. The 1950s shoreline was also scanned and directly georeferenced to recent imagery. The 1995 and 2007 shorelines were digitized directly from georeferenced aerial photographs. The 1996 and 1998 shorelines were determined by ground GPS surveys. The 2000, 2012, and 2019 shorelines were extracted from airborne lidar surveys conducted by the Bureau. Shoreline segment locations are shown on fig. 1.

Segment	1930s	1950s	1960s	1970s	1990s	2000s	2010s
Sabine Pass to Rollover Pass	1930	1955-56	1965	1974	1996	2000, 2007	2012, 2019
Bolivar Peninsula	1930	1956	1965	1974	1996	2000, 2007	2012, 2019
Galveston Island	1930, 1934	1956	1964-65	1970, 1974	1995, 1996	2000, 2007	2012, 2019
Brazos–Colorado headland	1930, 1934	1956	1965	1974	1991, 1995	2000, 2007	2012, 2019
Matagorda Peninsula	1937	1956	1965	1974	1991	2000, 2007	2012, 2019
Matagorda Island	1937	1956-57	1965	1974	1995	2000, 2007	2012, 2019
San José Island	1931, 1937	1957-58	1965	1974	1995, 1998	2000, 2007	2012, 2019
Mustang Island	1937	1958-59	1965, 1969	1974	1990, 1995	2000, 2007	2012, 2019
N. Padre Island	1937-38	1956, 1959-60	1969	1974-75	1990, 1995	2000, 2007	2012, 2019
S. Padre Island	1934, 1937		1960, 1969	1974-75	1995	2000, 2007	2012, 2019
Brazos Island	1934, 1937		1960	1974	1995	2000, 2007	2012, 2019

Shoreline positions extracted from 2019 lidar data were chosen and verified by visually comparing a range of shoreline proxy contour elevations with the wet- and dry-beach boundary as shown on georeferenced 2016 and 2018 NAIP aerial photographs and imagery acquired during the airborne survey. We also used beach profiles and GPS-mapped shorelines acquired for the Bureau's Texas High School Coastal Monitoring Program (THSCMP; Caudle and Paine, 2012, 2017) near the dates of the lidar survey to compare the observed wet-beach/dry-beach positions at representative long-term monitoring sites on Bolivar Peninsula, Galveston Island, Follets Island, Matagorda Peninsula, Mustang Island, and Padre Island (fig. 4).

Sources of Shorelines

In general, the accuracy of the historical shoreline positions improves with advances in technology. There is some inherent uncertainty as to the precision of the data in the original topographic charts from the 1800s that were prepared by the U.S. Coast Survey. For aerial photography optical resolution, the quality of photographic negatives or digital images, mosaic compilation techniques, and georeferencing accuracy all improved over time between the earliest photographs in the 1930s and the most recent photographs (2007) used in this study. Another potential error is the position of the land-water interface (most consistently expressed as the wet-beach/dry-beach boundary) on aerial imagery. This position depends on the tidal cycle, beach slope, and wind direction, speed, and duration when the image was taken, and can differ according to date and location. For this update, the 1800s shorelines are considered to be the largest source of error and were not used in the calculation of shoreline movement.

As documented in previous Bureau publications, mapped shorelines from the 1800s to early 1990s were originally optically transferred to common paper 7.5-minute topographic base maps at 1:24,000 scale. Shoreline studies in the 1970s until the early 1990s (Morton, 1974, 1975, 1977; Morton and Pieper, 1975a, 1975b, 1976, 1977a, 1977b; Morton and others, 1976; Paine and Morton, 1989; Morton and Paine, 1990) calculated shoreline change rates directly from measurements made on the USGS topographic maps. With the advent of GIS in the 1990s, those

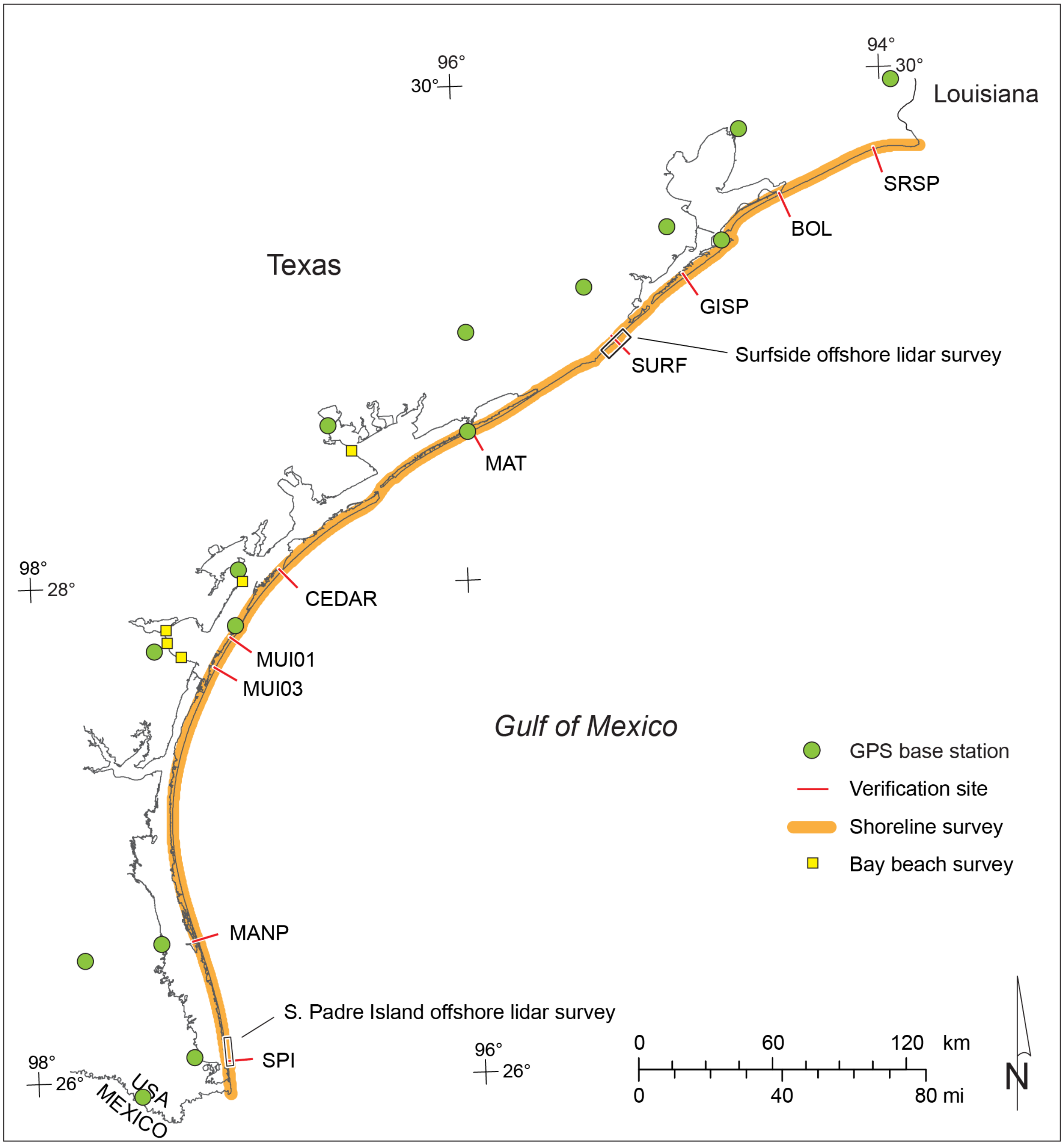

Figure 4. Location of 2019 Gulf shoreline, bay beach, and offshore lidar survey areas, ground GPS base stations, and shoreline position verification sites.

older shoreline positions were digitized from the original paper maps. To reduce potential errors in shoreline position by directly georeferencing the older imagery and reducing the number of transfer steps, the original 1950s quadrangle-scale photomosaics (with mapped shorelines) were scanned at 600 dpi to create a digital image, then directly georeferenced using newer imagery in the NAD83 coordinate system. Photography used to georeference the 1950s photomosaics was 50-cm resolution, natural color, Texas Orthoimagery Program digital imagery photographed in 2015 and 1-m resolution, natural color, National Agricultural Inventory Program digital imagery photographed in 2016. At least 8 control points were used to georeference each of the 1950s photomosaic quadrangles to the newer imagery, matching objects that were visible in both images such as land features, roads, or buildings. The shoreline positions originally mapped on the 1950s photomosaics were then digitized directly in ArcGIS. Directly georeferencing the imagery reduces error that can be introduced through the older optical transfer to paper maps, georeferencing in the superseded NAD27 coordinate system, digitizing shoreline positions from the paper maps, and transforming the shorelines to the newer NAD83 coordinate system.

The 1995 shoreline was digitized directly from georeferenced aerial imagery. The 1996 (upper coast) and 1998 (middle coast) shorelines were surveyed using differentially corrected GPS data acquired from a GPS receiver mounted on a motorized vehicle (Morton and others, 1993; Morton, 1997). The 2000 and 2012 shorelines were surveyed using an Optech ALTM 1225 airborne laser terrain mapping instrument (lidar). Laser range data were combined with differentially corrected aircraft position determined from GPS and an inertial measurement unit to determine land-surface position and elevation. Shoreline position was extracted from the lidar-derived digital elevation model at an elevation of 0.6 m (2.0 ft) above mean sea level (msl), which was determined to be the best match to the wet-beach/dry-beach boundary for those surveys. The 2007 shoreline was mapped within a GIS environment by digitizing the wet-beach/dry-beach boundary as depicted on high-resolution, georeferenced aerial photographs taken in 2007 (Paine and others, 2011).

Studies conducted when the Bureau began to use lidar data for shoreline position extraction, based on lidar data acquired in 2000 and 2001 and beach profiles acquired in 2001, determined that the wet-beach/dry-beach boundary occurred at 0.6 m msl (Gibeaut and others, 2000, 2001, 2002; Gibeaut and Caudle, 2009). Using the most seaward, continuous contour of 0.6 m msl provided a consistent shoreline proxy feature between the lidar datasets and historical mapping practices. During lidar data processing, the elevation values expressed as height above an ellipsoid (HAE) are transformed to North American Vertical Datum of 1988 (NAVD88) orthometric heights by applying a geoid model correction. Lidar datasets acquired by the Bureau between 2000 and 2012 used the National Geodetic Survey's (NGS) Geoid99 model to make the transformation from ellipsoidal heights to NAVD88 elevations. Geoid99 has been superseded by newer geoid models as the NGS produces new geoid models every few years to more accurately represent the equipotential surface and incorporate additional data. Lidar surveys conducted since 2012 use the Geoid12B model to convert elevation values from HAE to elevations with respect to NAVD88, which may cause apparent differences in elevation between surveys. In addition, mean sea level continues to rise relative to NAVD88 (fig. 2 and table 1).

Before 2013, the 0.6 m msl elevation was used as the shoreline proxy from Bureau lidar-derived digital elevation models created using the Geoid99 model. This contour reasonably matched the position of the wet-beach/dry-beach boundary used as a mappable shoreline proxy on aerial imagery for the 2012 airborne lidar survey (Paine and Caudle, 2014). For the 2013 South Padre Island survey (Caudle and others, 2014, 2019), the 0.6 m msl elevation, with HAE transformed to NAVD88 elevations using the newer Geoid12B model, was too low on the shoreface and was discontinuous due to its proximity to the seaward edge of the topographic DEM, indicating the 0.6 m msl elevation was at or below the waterline in places. Beach profiles collected by Bureau staff and Texas High School Coastal Monitoring Program (THSCMP) students between 2000 and 2013, GPS-based shoreline mapping conducted by THSCMP students near the dates of the lidar survey, and comparisons with the position of the wet-beach/dry-beach boundary on aerial imagery acquired during the lidar survey were used to select a proxy elevation of 0.9 m msl that better matched the wet-beach/dry-beach boundary for that area and survey.

The process of rigorously evaluating the shoreline proxy elevation that best matches the wet-beach/dry-beach boundary includes comparing extracted elevation contours with the wet-beach/dry-beach position as expressed on aerial imagery, beach profiles, and the ground-based GPS-mapping relevant to each lidar survey. A similar evaluation process was conducted for the 2016 U.S. Army Corps of Engineers (USACE) and the 2017 post-Harvey lidar surveys.

The 2019 shoreline position was extracted from lidar data acquired by the Bureau between April 2 and June 2 (Appendix). Laser-range data were combined with aircraft position and orientation determined from ground- and aircraft-based GPS and an inertial measurement unit to determine land-surface position and height above the GRS80 ellipsoid. The Geiod12B model was applied to convert elevation values from HAE to elevations with respect to NAVD88.

To determine the shoreline proxy elevation that best matches the wet-beach/dry-beach boundary at the time of the survey, we examined (1) the 2019 Bureau lidar data and aerial imagery; (2) Gulf shoreline (Sargent Beach to Aransas Pass) lidar data collected by the Bureau in 2013, 2014, and 2015 (Paine and others, 2016); (3) the 2016 lidar data acquired by the USACE (USACE, 2017); (4) beach profiles collected by Bureau researchers and students participating in the THSCMP; (5) GPS-based shoreline mapping conducted by THSCMP students; and (6) the 2016 and 2018 NAIP aerial imagery. Through analysis of wet-beach/dry-beach boundary elevations reported in Bureau- and THSCMP-collected beach profiles (1997-2019), several elevation contours were examined to determine the elevation that best represents the shoreline position most consistent with historical mapping practices. A final shoreline position was extracted from the lidar-derived DEM at an elevation of 1.15 m (3.8 ft) NAVD88, which is equivalent to approximately 1 m (3.3 ft) msl.

The extracted elevation contour should be reevaluated with each lidar survey to ensure that the shoreline proxy represents the best approximation of the wet-beach/dry-beach boundary at the time of the survey and not necessarily the elevation that was used during a previous survey. This approach ensures that the extracted elevation best represents current conditions and remains consistent with historical mapping of the shoreline position using the wet-beach/dry-beach boundary as depicted on aerial photographs.

Positional Verification

The georeferencing of shoreline position is one of the principal sources of potential error in determining long-term shoreline change rates (Anders and Byrnes, 1991; Crowell and others, 1991; Moore, 2000). Georeferencing of the 2019 airborne lidar survey data was checked by (a) comparing ground GPS-derived and lidar-derived locations and elevations at Bureau-surveyed calibration targets and (b) comparing equivalent natural and constructed features common to 2019 airborne lidar survey data and georeferenced NAIP photographs taken in 2016 and 2018.

A third positional check, which addressed the relative position of the shoreline proxy (1.0 m [3.3 ft] msl elevation contour) and the wet-beach/dry-beach boundary, was accomplished by superimposing the lidar-derived shoreline proxy and GPS-based, wet-beach/dry-beach boundary data acquired in spring 2019 by Bureau researchers and THSCMP students on georeferenced 2016 and 2018 NAIP imagery. On Matagorda Peninsula, the wet-beach/dry-beach boundary was mapped by THSCMP participants in September 2018 and 2019. These comparisons, in some cases from imagery and ground-based GPS data acquired within a few days or weeks of the lidar survey date, generally showed good agreement (within a few meters) between boundaries interpreted from imagery and ground-based data and those extracted from lidar data. Minor differences (less than 10 m) in the position of the lidar-derived shoreline and the wet-beach/dry-beach boundary are likely to reflect real differences in beach morphology between the dates of the lidar survey and those of the imagery and ground-based GPS surveys in the highly dynamic, low-slope beach environment.

Comparisons of lidar-extracted shoreline and wet-beach/dry-beach positions were conducted for THSCMP beach profile sites at Bolivar Peninsula, Galveston Island State Park, Matagorda Peninsula, Mustang Island, and northern and southern Padre Island (fig. 4). On Bolivar Peninsula (fig. 5) there is good agreement among the wet-beach/dry-beach boundary surveyed by THSCMP students and Bureau staff near profile site BOL03 on April 23, 2019, the 2019 lidar-extracted shoreline, 2019 Bureau aerial imagery, and 2018 NAIP imagery. The GPS-mapped wet beach/dry beach boundary is at a higher elevation (0.05 to 0.15 m) on the beach and is 3 to 10 m farther landward.

At Galveston Island State Park (figs. 4 and 6), there is good agreement between the 2019 lidar-derived shoreline and the GPS-based wet-beach/dry-beach boundary mapped on April 10, 2019

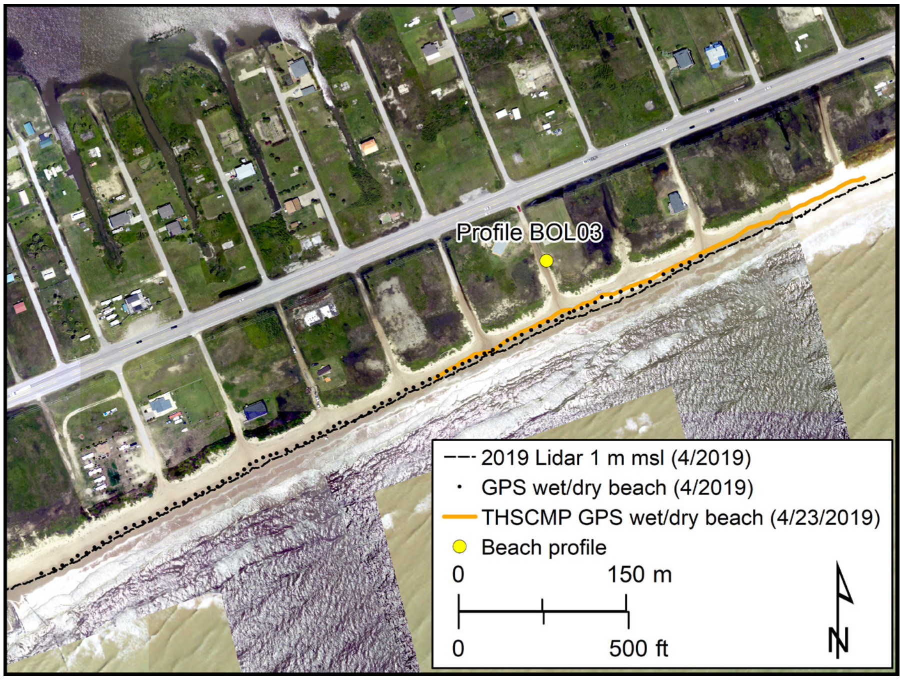

Figure 5. Shoreline position comparison at Bolivar Peninsula profile BOL03 near Rollover Pass (profile site BOL, fig. 4). Shorelines include the wet-beach/dry-beach boundary mapped on April 24, 2019 by THSCMP participants using ground GPS and the 1 m (3.3 ft) msl shoreline proxy extracted from airborne lidar data acquired in spring 2019, superimposed on 2018 NAIP and 2019 Bureau imagery. The NAIP imagery can be seen in the northeastern corner of the image.

(Bureau) and April 25, 2019 (THSCMP) at station BEG02. The lidar-derived shoreline proxy at 1 m (3.3 ft) msl is slightly higher (more landward) than the boundary between the wet and dry beach evident on the 2018 NAIP imagery, but coincides with the 2019 Bureau-acquired aerial imagery.

At Surfside Beach (figs. 4 and 7), there is excellent positional agreement between the 2019 lidar-derived shoreline proxy, the wet-beach/dry-beach boundary mapped on April 24, 2019 by THSCMP participants and Bureau staff, and the 2019 aerial imagery. The lidar-derived shoreline position also coincides with the visual wet-beach/dry-beach boundary on the 2018 NAIP imagery.

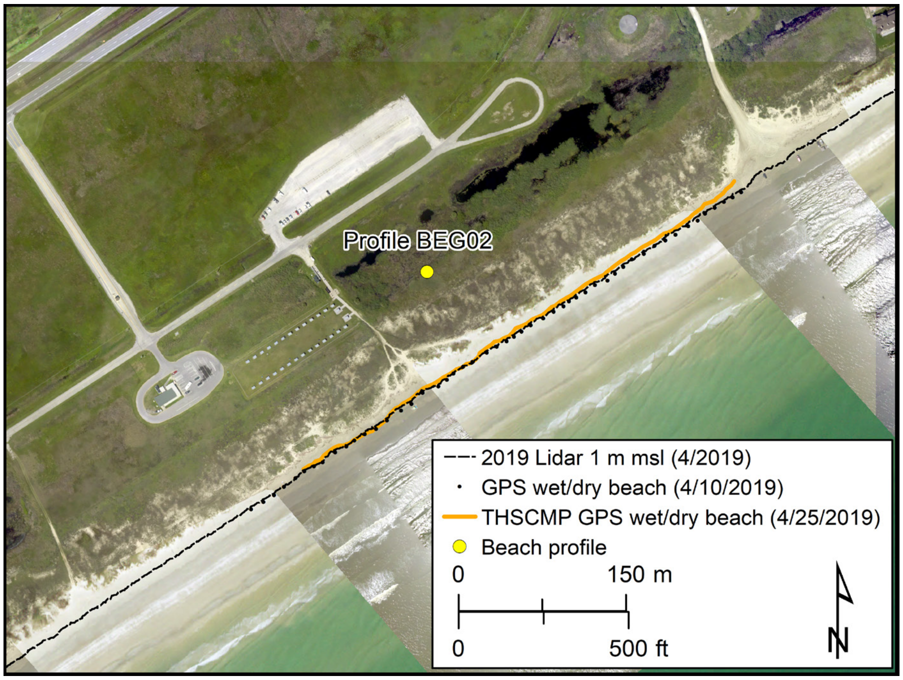

Figure 6. Shoreline position comparison at Galveston Island State Park site BEG02 (profile site GISP, fig. 4). Shorelines include the wet-beach/dry-beach boundary mapped on April 25, 2019 by THSCMP students and April 10, 2019 by Bureau staff using ground GPS and the 1 m (3.3 ft) msl shoreline proxy extracted from airborne lidar data acquired in spring 2019, superimposed on 2018 NAIP and 2019 Bureau imagery. NAIP imagery fills gaps in the Bureau imagery.

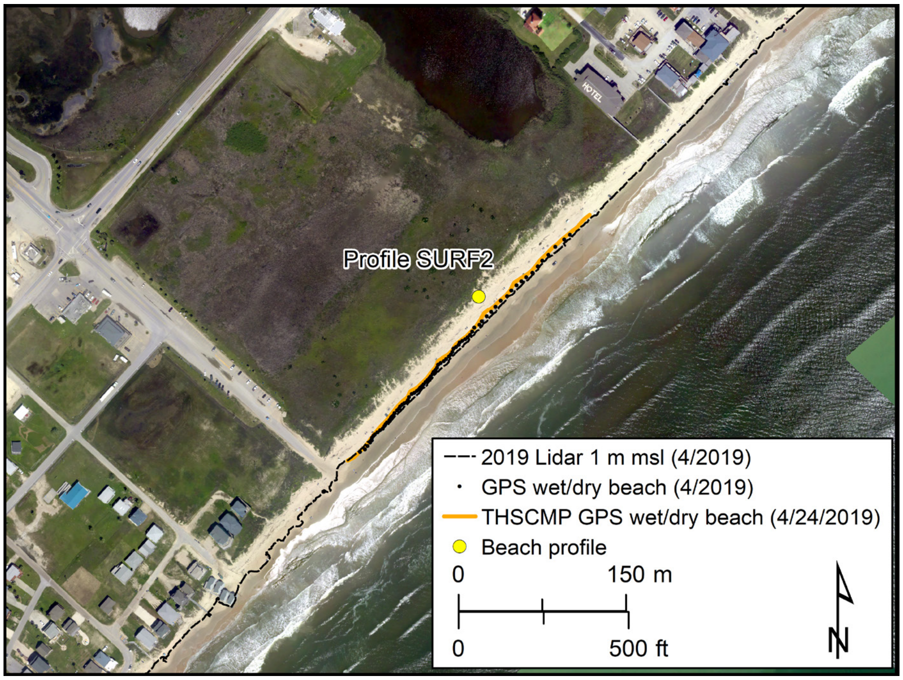

Figure 7. Shoreline position comparison at Surfside Beach site SURF2 (profile site SURF, fig. 4). Shorelines include the wet-beach/dry-beach boundary mapped on April 24, 2019 by THSCMP students and Bureau staff using ground GPS and the 1 m (3.3 ft) msl shoreline proxy extracted from airborne lidar data acquired in spring 2019, superimposed on 2019 Bureau imagery.

On Matagorda Peninsula (site MAT02, figs. 4 and 8), there is good agreement between the lidar-extracted shoreline from the 2019 survey and the position of the wet-beach/dry-beach boundary mapped by THSCMP students on September 27, 2018. A THSCMP GPS-based survey of the wet-beach/dry-beach boundary acquired on September 25, 2019 and the visual wet-beach/dry-beach boundary on the 2019 Bureau aerial photography is slightly landward of the lidar-derived shoreline.

Lidar, imagery, and GPS comparisons on Mustang Island (sites MUI01 and MUI03, figs. 4 and 9) show good agreement between the lidar-extracted shoreline from the 2019 survey and the wet-beach/dry-beach boundary evident on 2018 NAIP imagery and 2019 Bureau imagery. GPS surveys of the shoreline acquired by THSCMP students and the Bureau on April 30, 2019 indicates a shoreline position that coincides with the lidar-extracted shoreline.

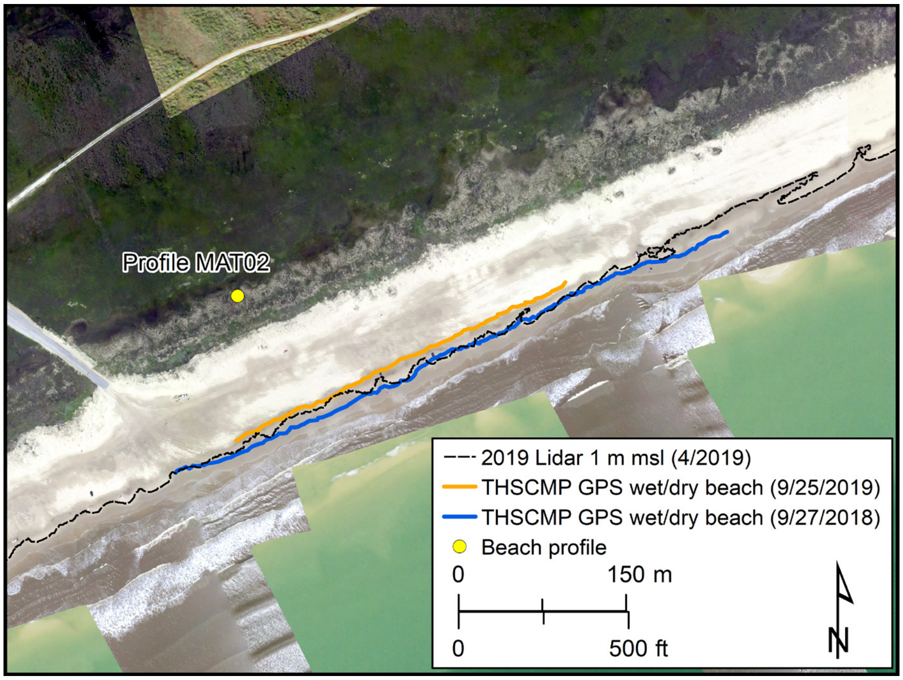

Figure 8. Shoreline position comparison at Matagorda Peninsula site MAT02 (profile site MAT, fig. 4). Shorelines include the wet-beach/dry-beach boundary mapped on September 27, 2018 and September 25, 2019 by THSCMP students using ground GPS and the 1 m (3.3 ft) msl shoreline proxy extracted from airborne lidar data acquired in spring 2019, superimposed on 2018 NAIP and 2019 Bureau imagery. NAIP imagery fills gaps in the Bureau imagery.

On southern Padre Island (site SPI01, figs. 4 and 10), there is excellent positional agreement between the 2019 lidar-extracted shoreline and the wet-beach/dry-beach boundary as depicted on the 2018 NAIP aerial imagery. A GPS survey by THSCMP students and Bureau staff on January 10, 2019 shows good positional agreement between the wet-beach/dry-beach boundary and the lidar-derived shoreline.

We compared lidar-extracted shoreline positions to imagery at other coastal sites where beach surveys were not available. Minor differences between the lidar-derived shoreline and the visual wet-beach/dry-beach boundary can be expected due to variations in the shoreface between the time of the imagery and lidar survey. Examples of these comparisons are located on the upper Texas coast at Sea Rim State Park (site SRSP, fig. 4), the middle Texas coast at Cedar Bayou

(a)

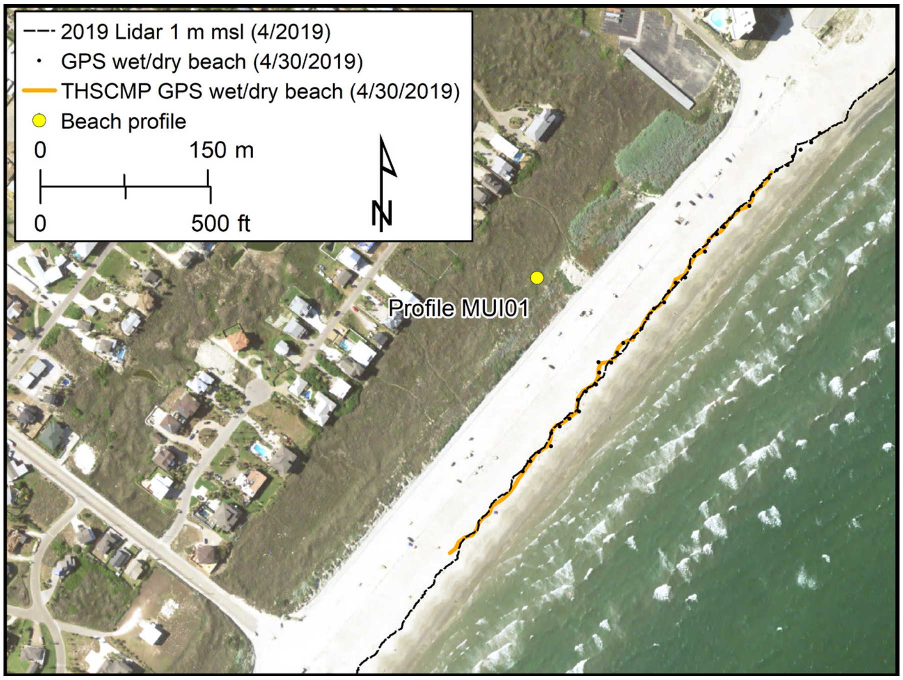

(b)

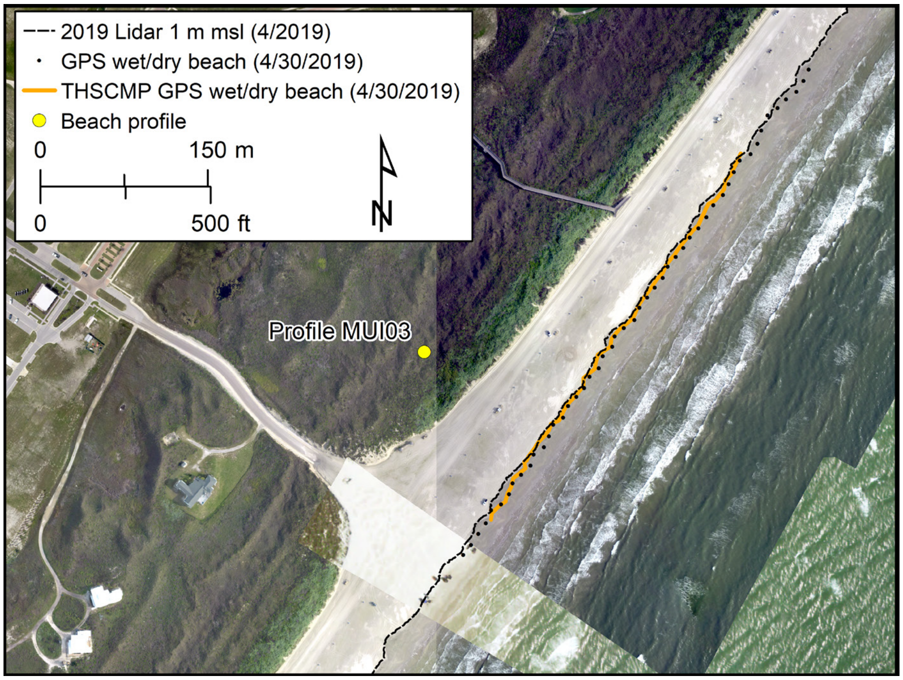

Figure 9. Shoreline position comparison at Mustang Island sites (a) MUI01 and (b) MUI03 (fig. 4). Shorelines include the wet-beach/dry-beach boundary mapped on April 30, 2019 by THSCMP students and Bureau staff using ground GPS and the 1 m (3.3 ft) msl shoreline proxy extracted from airborne lidar data acquired in spring 2019, superimposed on 2018 NAIP and 2019 Bureau imagery. NAIP imagery fills gaps in the Bureau imagery. MUI01 is shown on NAIP imagery only.

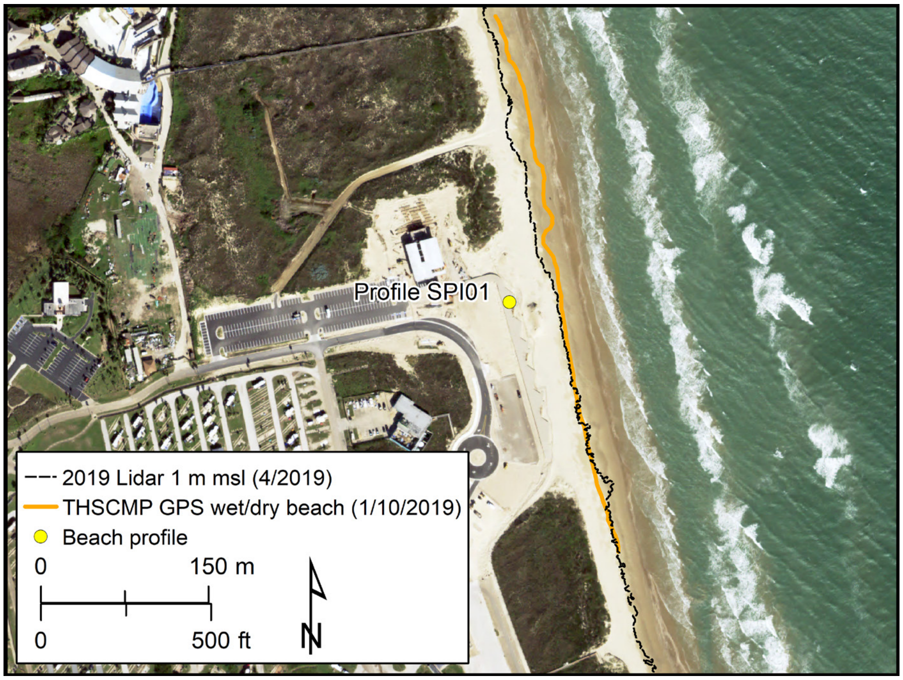

Figure 10. Shoreline position comparison on southern Padre Island at site SPI (fig. 4). Shorelines include the wet-beach/dry-beach boundary mapped on January 10, 2019 by THSCMP students and Bureau staff using ground GPS and the 1 m (3.3 ft) msl shoreline proxy extracted from airborne lidar data acquired in spring 2019, superimposed on 2018 NAIP imagery.

between San José and Matagorda Islands (site CEDAR, fig. 4), and the lower Texas coast adjacent to Mansfield Pass on Padre Island (site MANP, fig. 4). At Sea Rim State Park (fig. 11) and Cedar Bayou (fig. 12), the extracted 1-m (3-ft) shoreline determined from airborne lidar data coincides well with the wet-beach/dry-beach boundary depicted on the 2019 Bureau imagery. Although not shown, the lidar-derived shoreline at Cedar Bayou closely coincides with the wet-beach/dry-beach boundary depicted on 2018 NAIP aerial imagery. On Padre Island near Mansfield Pass, agreement is good between lidar-derived shoreline position and the wet-beach/dry-beach boundary on the 2018 NAIP imagery (fig. 13). Similar reasonable agreement between lidar-extracted shoreline position and shoreline features depicted on aerial imagery acquired in 2016, 2018, and 2019 was observed along all major segments of the Texas coast.

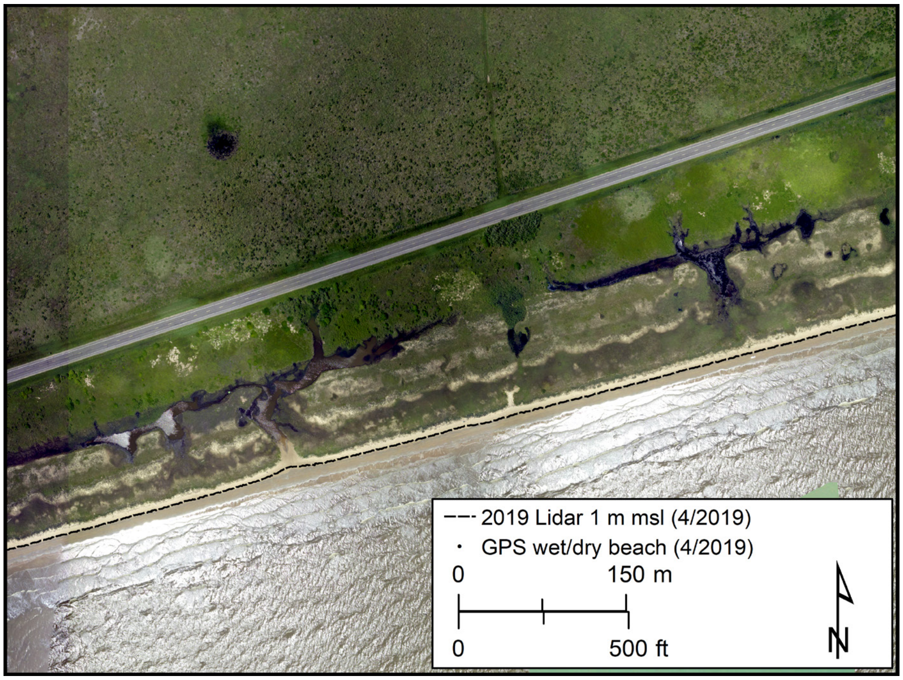

Figure 11. Shoreline position comparison on the upper Texas coast at Sea Rim State Park (SRSP, fig. 4). The 1 m (3.3 ft) msl shoreline proxy extracted from spring 2019 lidar data is superimposed on 2019 Bureau imagery.

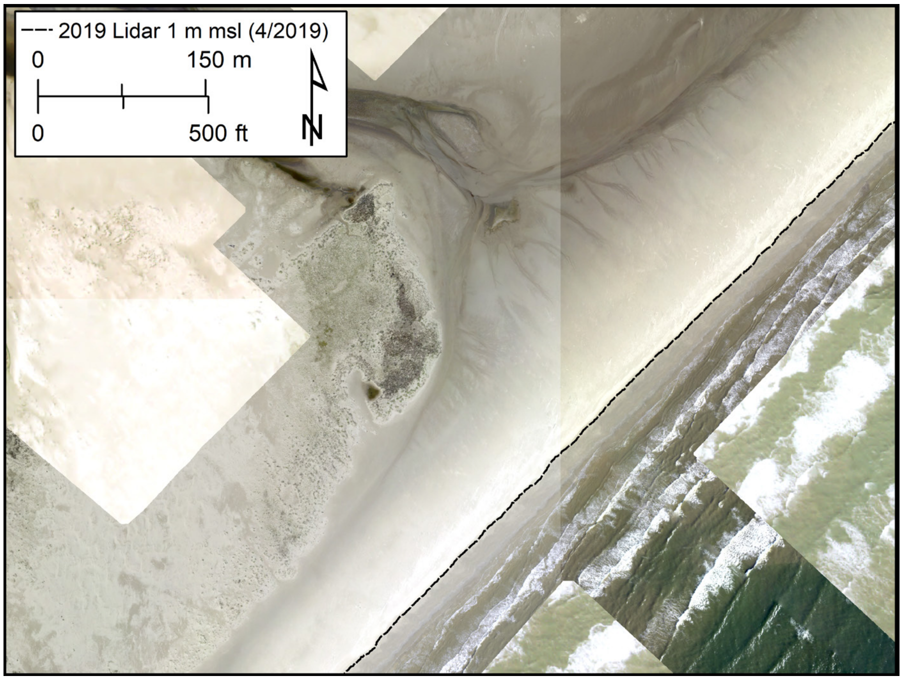

Figure 12. Shoreline position comparison at Cedar Bayou on the middle Texas coast (site CEDAR, fig. 4). The 1 m (3.3 ft) msl shoreline proxy extracted from spring 2019 lidar data is superimposed on 2019 Bureau imagery.

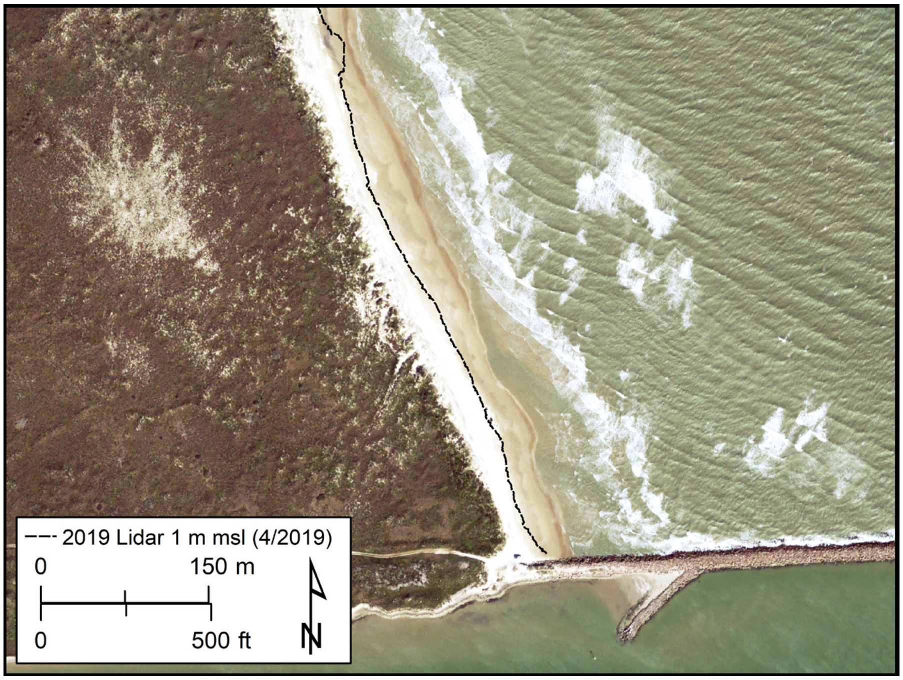

Figure 13. Shoreline position comparison on the lower Texas coast at Mansfield Pass (site MANP, fig. 4). The 1 m (3.3 ft) msl shoreline proxy extracted from spring 2019 lidar data is superimposed on 2018 NAIP imagery.

2019 Volumetrics and the Landward Dune Boundary

Beyond extracting shoreline position and determining shoreline movement rates, lidar-based elevation data from the beach and dune system allow greater analysis of beach and dune elevation patterns and volumetrics. These three-dimensional data can be used to quantify sediment volumes, examine relationships to shoreline movement, and identify beach segments that may be susceptible to breaching or overwash during tropical cyclone passage.

We used a program written at the Bureau to calculate dune heights and sediment volumes for the 2019 airborne lidar survey of the Texas Gulf shoreline. Beach and dune transects (the same ones used to calculate shoreline movement at 50-m [164-ft] spacings) and the landward dune boundary are imported into the program along with lidar-derived, 1-m resolution DEMs. The landward dune boundary and an approximate shoreline are used to generate a mask to remove areas extraneous to beach and foredune volume determinations. For each transect, sediment volumes above threshold elevations are calculated within the beach and foredune area at 0.5 m (1.6 ft) intervals, beginning with 1 m (3.3 ft) NAVD88 through 9.5 m (31 ft). All DEM cells within 25 m (82 ft) of the transect are included in this calculation. The highest elevation value is recorded as the maximum dune height. These data are compiled and merged, analyzed, and exported to a GIS shapefile using a Python script.

The position of the landward dune boundary is an important factor in defining the foredune complex for volumetric and geomorphic analysis. It is also helpful for use in determining design setback distances or creating dune restoration projects. Selection of the landward dune boundary is a manual process that takes into account several criteria. These include: being at or near a change in slope from steep on the dune to gentle on the barrier flat; having an elevation of 2 m (6.6 ft) NAVD88 or greater; bounding dunes that provide at least minimal storm-surge protection; having an orientation that roughly parallels the shoreline; being adjacent to the shoreline and features classified as dunes; and connecting adjacent forms classified as dunes (Gibeaut and Caudle, 2009).

The landward dune boundary was digitized at scales of 1:1,000 to 1:5,000 using the 2019 lidar-derived DEMs, including height, slope, and hillshade representations, and aerial imagery. The foredune complex was defined as the seaward-most continuous feature with an elevation of at least 2 m (6.6 ft) NAVD88. If a single continuous feature was not present, dune clusters were considered to be part of the complex as long as they were arranged quasi-parallel to the shore and were close together or connected. In areas where dunes were absent (washover areas), the dune boundary was mapped at the 2 m (6.6 ft) NAVD88 contour, landward of any coppice dunes or mounds. Hillshade and slope were helpful for interpreting the extent of the dune boundary by visualizing the landward slope of dune features. Imagery was used to locate the extent of vegetation and to identify structures. Man-made structures are not considered to be part of the foredune complex; the landward dune boundary was placed seaward of buildings or retaining walls.

TEXAS GULF SHORELINE MOVEMENT THROUGH 2019

Rates of long-term Gulf shoreline change, calculated from shoreline positions between the 1930s and 2019 (fig. 14; table 4), averaged 1.27 m/yr (4.17 ft/yr) of retreat for net-rate and 1.29 m/yr (4.23 ft/yr) for linear regression-rate calculations. Rates were calculated at 11,722 sites along the entire Texas coast spaced at 50 m (164 ft). Net retreat occurred at 9,336 sites (80 percent) and advance occurred at 2,225 sites (19 percent). No significant net movement was determined at the remaining sites. Net retreat at rates greater than 0.6 m/yr (2.0 ft/yr) was measured at 7,043 sites (60 percent). The average movement rate is slightly higher than the average movement rate of 1.26 m/yr (4.13 ft/yr) determined for the most recent previous update through 2012 (Paine and others, 2014). Shorelines along the northeastern Texas coast (from Sabine Pass to the mouth of the Colorado River) generally retreated at greater rates than those on the middle and lower coast. Average change rates were retreat at 1.71 m/yr (5.6 ft/yr) for the northeastern part of the coast and retreat at 0.97 m/yr (3.2 ft/yr) for the middle and lower coast.

From the upper coast to the lower coast, notable extensive areas of relatively high long-term retreat rates include the Sabine chenier and Trinity headland area, an area on Galveston Island west of the seawall, Follets Island near San Luis Pass, the fluvial and deltaic headland of the Brazos and Colorado rivers, Matagorda Peninsula west of the Colorado River, Matagorda Peninsula and Matagorda Island near Pass Cavallo, northern San José Island, northern Padre Island, and most of the southern half of Padre Island (fig. 14). Limited areas of general net shoreline advance are found on the upper coast near the Sabine Pass and Bolivar Roads jetties, at the western tip of Galveston Island, adjacent to the mouth of the Brazos River, at the western end of Matagorda Peninsula, on the middle Texas coast along the northern part of Matagorda Island and near Aransas Pass, and on Padre Island near Baffin Bay and the southern end of the island (fig. 14).

Closely spaced measurement sites allow estimates of land loss to be made (fig. 14 and table 4). The annual rate of land loss along the Texas Gulf shoreline, updated from the 1930s through

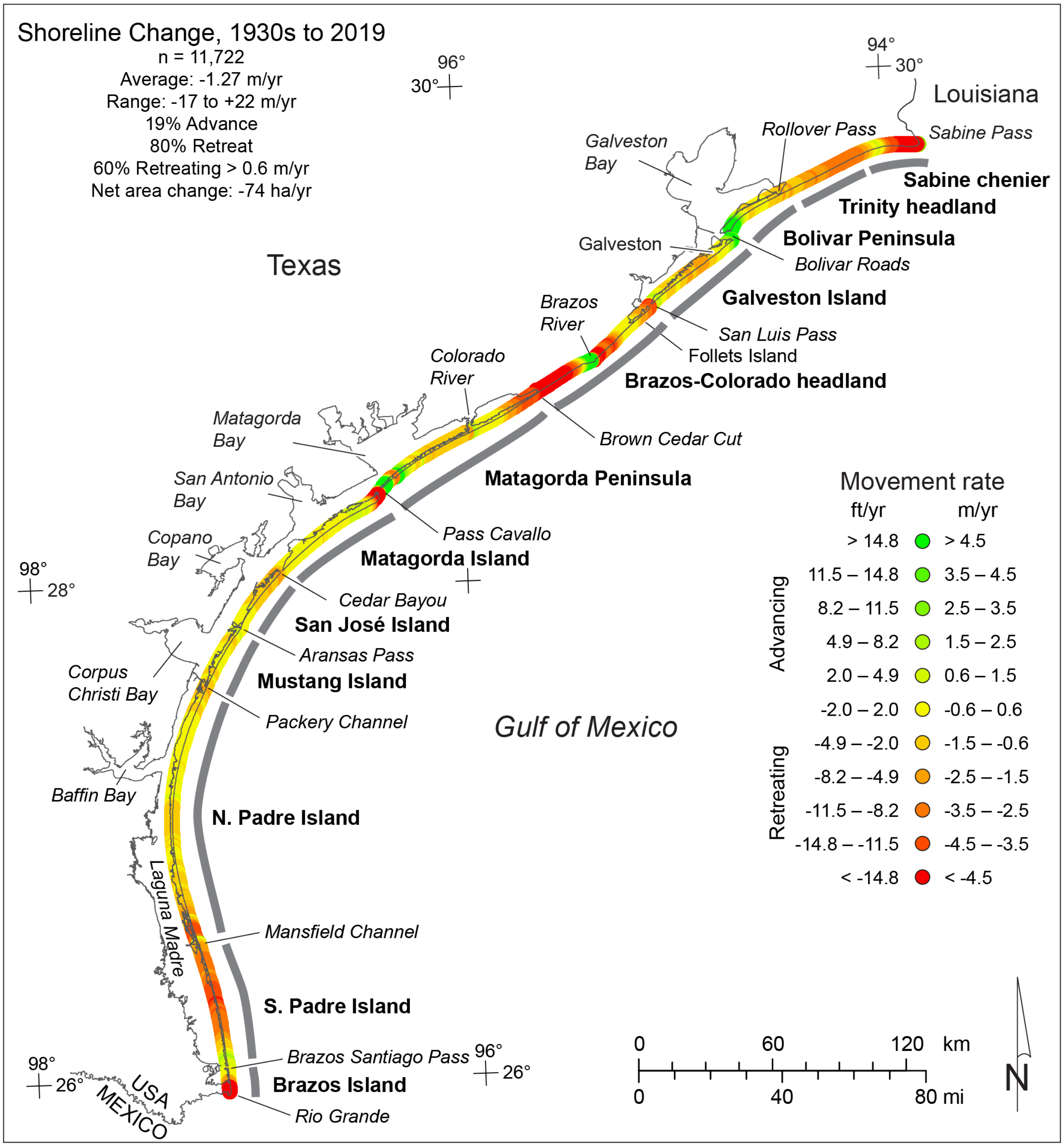

Figure 14. Net rates of long-term movement for the Texas Gulf shoreline between Sabine Pass and the Rio Grande calculated from shoreline positions from the 1930s to 2019.

Table 4. Net shoreline and land-area change between the 1930s and 2019 for the Texas Gulf shoreline and major geomorphic areas (fig. 14) with shoreline on the Gulf of Mexico.

Area	No.	Net rate (m/yr)	Std. dev. (m/yr)	Range (m/yr)	Area change rate (ha/yr)	Area change (ha)
All Texas sites	11,722	-1.27	2.77	-16.5 to +22.0	-74.5	-6,627
Geomorphic Areas						
Sabine Pass to Rollover Pass	1,345	-3.03	2.64	-11.6 to +10.6	-20.4	-1,814
Bolivar Peninsula	542	+0.28	2.60	-1.9 to +14.2	+0.75	+67
Galveston Island (all)	932	-0.21	1.76	-2.5 to +5.9	-0.98	-87
Galv. Is. (no seawall)	704	-0.22	1.99	-2.5 to +5.9	-0.78	-70
Galv. Is. (East Beach)	108	+3.66	1.38	+1.6 to +5.9	+2.0	+176
Galv. Is. (West Beach)	596	-0.93	1.06	-2.5 to +3.8	-2.8	-246
Brazos–Colorado headland	1,244	-2.16	4.79	-13.2 to +18.1	-13.4	-1,194
Matagorda Peninsula	1,589	-0.89	2.84	-12.2 to +22.0	-7.1	-631
Matagorda Island	1,116	-0.91	3.70	-16.5 to +14.4	-5.1	-452
San José Island	622	-0.84	0.67	-1.9 to +0.8	-2.6	-231
Mustang Island	574	-0.29	0.52	-1.4 to +1.7	-0.83	-74
N. Padre Island	2,403	-0.77	0.93	-4.4 to +1.0	-9.2	-820
S. Padre Island	1,120	-2.46	1.51	-4.7 to +2.8	-13.8	-1,227
Brazos Island	235	-1.57	2.60	-7.2 to +2.3	-1.8	-164

2019, is 74 ha/yr (184 ac/yr). Total Texas Gulf shoreline land loss from 1930 through 2019 is estimated to be 6,627 ha (16,375 ac).

Recent Gulf Shoreline Movement, 2000 to 2019

One approach to assess whether shoreline movement rates are increasing, decreasing, or remaining constant over time is to compare long-term rates with rates measured over shorter and more recent periods. Coast-wide data on shoreline position are available from aerial imagery acquired since the 1930s, GPS surveys in the 1990s, and from airborne lidar surveys conducted in 2000, 2012, and 2019. We have augmented the long-term rates (1930s to 2019, fig. 14; table 4) with additional analyses for 2000 to 2019, the most recent period for which we have comparable lidar data coverage (fig. 15; table 5).

Overall, change patterns are similar for the shorter monitoring period (figs. 14 and 15). Major areas of shoreline retreat and advance are similar, but average rates of change differ among the periods for the entire coast as well as for major geomorphic features (fig. 16), and there is a higher percentage of shoreline that advanced during the most recent monitoring period. Average retreat rate for the entire coast is slightly higher over the long-term (1930s to 2019) monitoring period (retreat at 1.27 m/yr [4.2 ft/yr]) than it is over the most recent, short-term (2000 to 2019) monitoring period (retreat at 1.25 m/yr [4.1 ft/yr]). Percentages of sites advancing or retreating show a similar pattern: the shoreline retreated at a greater proportion of sites between the 1930s and 2019 (80 percent) than it did during the most recent monitoring period between 2000 and 2019 (71 percent). Estimated land-loss rates for the most recent period are 73 ha/yr (181 ac/yr), nearly identical to long-term land-loss rates of 74 ha/yr (184 ac/yr).

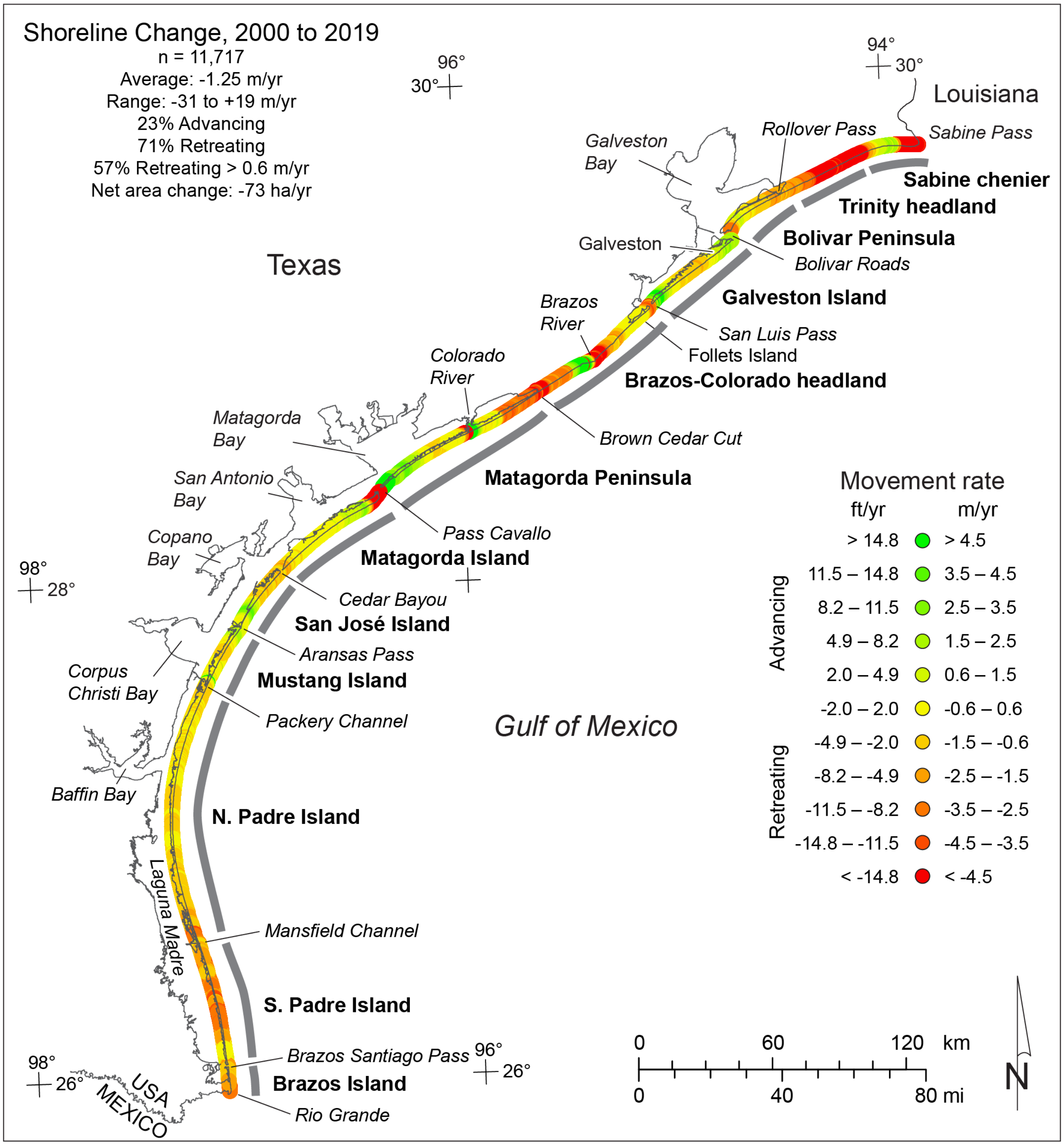

Figure 15. Net rates of recent, short-term movement for the Texas Gulf shoreline between Sabine Pass and the Rio Grande calculated from shoreline positions from 2000 to 2019.

Table 5. Net shoreline and land-area change between 2000 and 2019 for the Texas Gulf shoreline and major geomorphic areas (fig. 15) with shoreline on the Gulf of Mexico.

Area	**No.**	**Net rate (m/yr)**	**Std. dev. (m/yr)**	**Range (m/yr)**	**Area change rate (ha/yr)**	**Area change (ha)**
All Texas sites	11,717	-1.25	3.25	-30.6 to +18.5	-73.1	-1,389
Geomorphic Areas						
Sabine Pass to Rollover Pass	1,345	-4.49	3.63	-12.7 to +2.9	-30.2	-573
Bolivar Peninsula	542	-0.88	0.99	-2.8 to +1.5	-2.4	-45
Galveston Island (all)	930	+0.77	1.91	-2.0 to +11.0	+3.6	+68
Galv. Is. (no seawall)	704	+0.68	2.11	-2.0 to +11.0	+2.4	+46
Galv. Is. (East Beach)	108	+1.94	0.51	+0.2 to +3.3	+1.0	+20
Galv. Is. (West Beach)	596	+0.45	2.21	-2.0 to +11.0	+1.4	+26
Brazos–Colorado headland	1,244	-1.66	4.36	-30.6 to +9.2	-10.3	-196
Matagorda Peninsula	1,586	-0.20	3.87	-14.2 to +18.5	-1.6	-31
Matagorda Island	1,116	-1.65	4.83	-24.1 to +3.4	-9.2	-175
San José Island	622	-0.07	1.65	-2.4 to +4.8	-0.21	-4
Mustang Island	574	+0.15	0.97	-1.2 to +5.4	+0.42	+8
N. Padre Island	2,403	-0.82	0.76	-4.0 to +7.1	-9.8	-187
S. Padre Island	1,120	-1.99	1.26	-5.0 to +1.3	-11.2	-212
Brazos Island	235	-1.91	0.88	-4.1 to +0.7	-2.2	-43

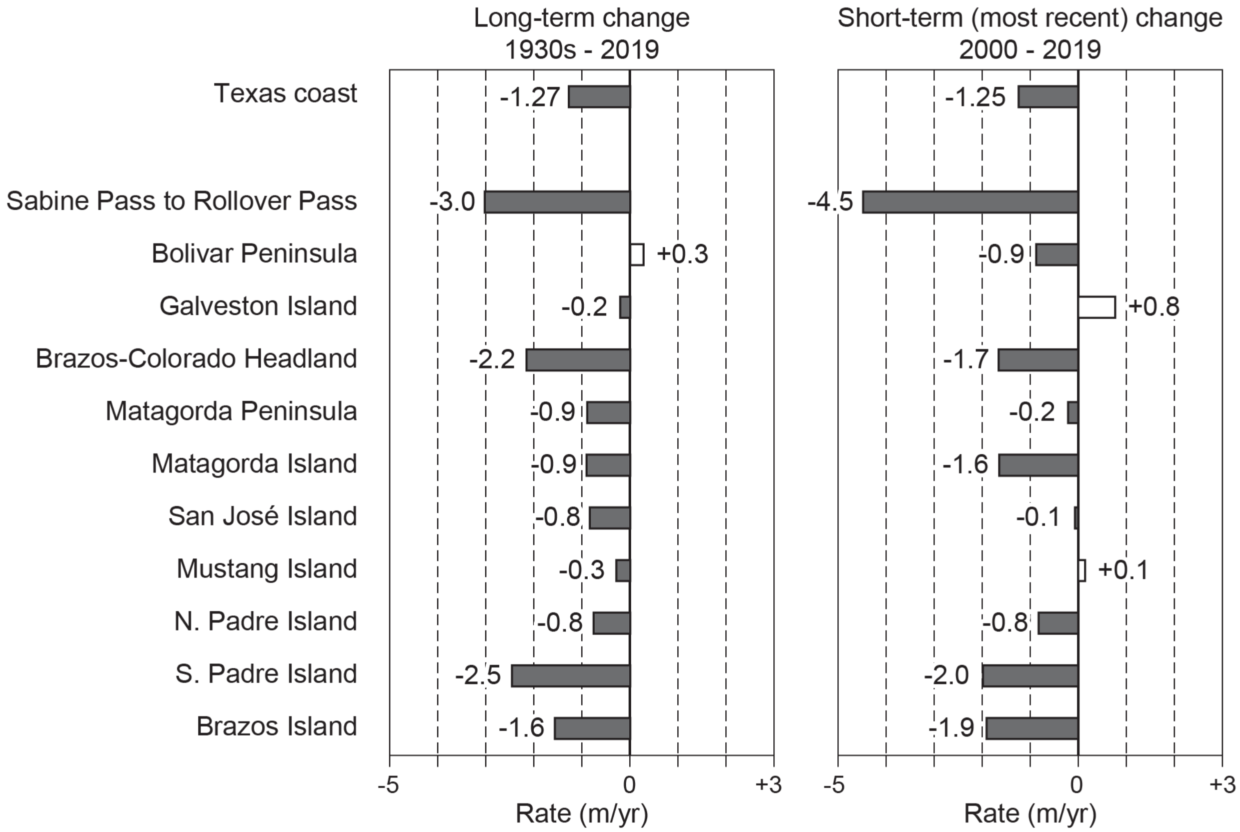

Figure 16. Comparison of long-term and most recent short-term net rates of shoreline movement for the Texas Gulf shoreline between Sabine Pass and the Rio Grande calculated from shoreline positions between the 1930s and 2019 and 2000 and 2019. Also shown are net rates for major geomorphic units along the coast.

Upper Texas Coast (Sabine Pass to San Luis Pass)

The upper Texas coast extends from Sabine Pass at the Texas–Louisiana border to San Luis Pass at the southwestern end of Galveston Island (figs. 14 and 17), a distance of about 141 km (88 mi). Major natural geomorphic features (fig. 14) and shoreline types are (1) the Sabine chenier, composed of generally shore-parallel beach ridges and intervening swales in the Sabine Pass area, (2) the Trinity headland, where thin, discontinuous sandy beaches and washover deposits rest on retreating low, muddy marsh deposits between Sea Rim State Park and High Island, (3) the broad, sandy beach and dune system on Bolivar Peninsula, and (4) the sandy barrier-island system at Galveston Island. Net longshore drift directions are eastward from the Trinity headland toward Sabine Pass, westward from the headland to Bolivar Roads, and

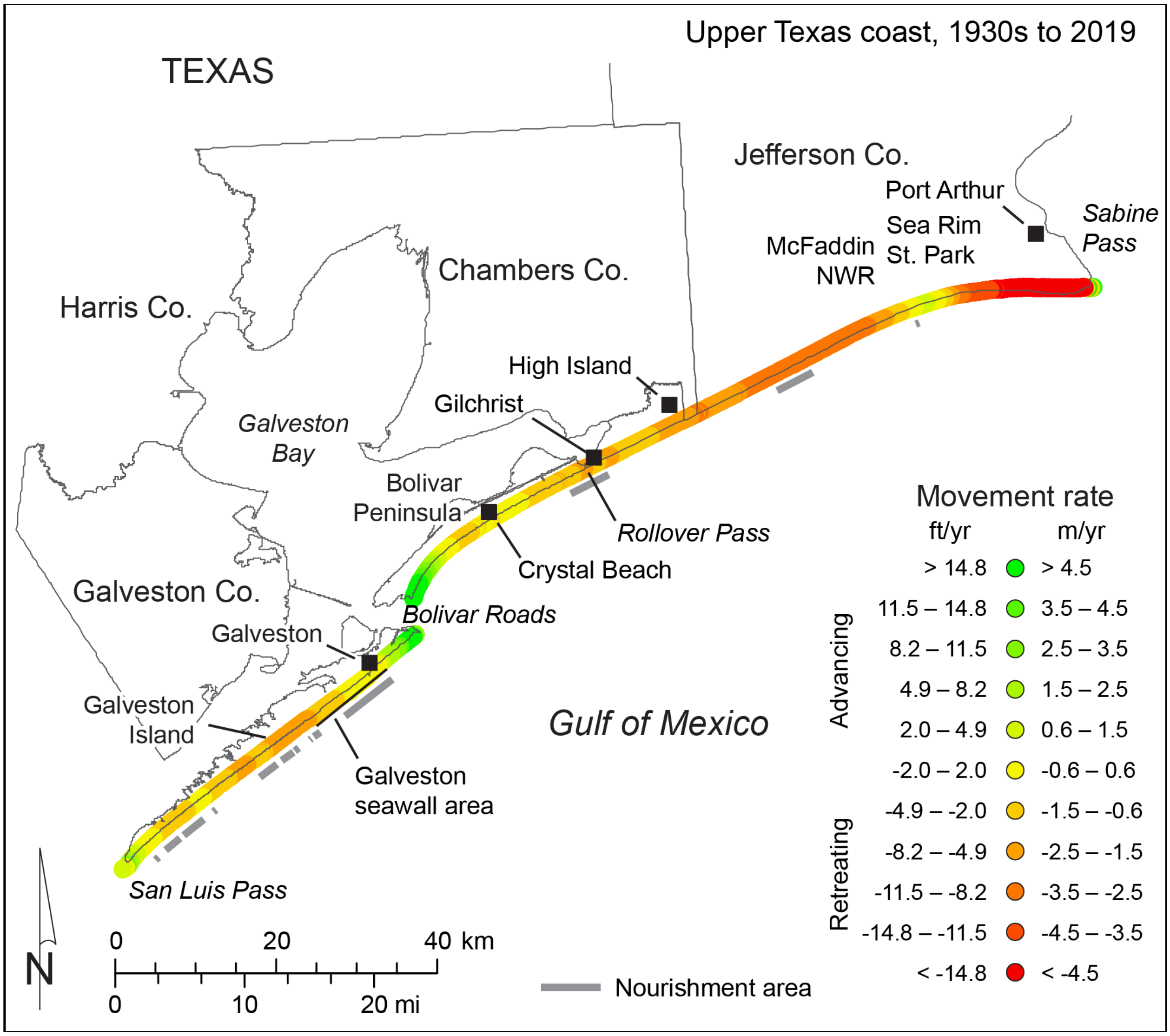

Figure 17. Net rates of long-term movement for the upper Texas Gulf shoreline between Sabine Pass and San Luis Pass (Sabine chenier, Trinity headland, and Galveston Island, fig. 14) calculated from shoreline positions between the 1930s and 2019 (table 3). Nourishment and restoration areas are listed in Appendix B.

eastward along Galveston Island, although longshore drift occurs in both directions depending on wave and wind conditions. Engineered structures that have affected the sediment budget and shoreline change rates include jetty and dredged channel systems at Sabine Pass and Bolivar Roads, a shallow (1.5 m [5 ft]) dredged channel across Bolivar Peninsula at Rollover Pass (scheduled for closure in 2020), and the seawall and groin system on the eastern part of Galveston Island. Sand has also been added to the system artificially through periodic and site-specific beach nourishment and dune restoration projects on the Trinity headland, Bolivar Peninsula, and Galveston Island (fig. 17; table B1 and fig. B1, Appendix B). At Sabine Pass, the south jetty extends about 4 km (2.5 mi) from the shoreline and protects a channel maintained at a depth of 12 m (40 ft). The Sabine Pass jetties and channel isolate the upper Texas coast from potential easterly sources of longshore sediment. The Bolivar Roads channel, maintained at a depth of 14 m (45 ft), is protected by jetties that extend 7.6 km (4.7 mi) (north jetty) and 3.9 km (2.4 mi) (south jetty) from the shoreline. The jetties and channel compartmentalize the upper Texas coast by blocking longshore transport of sand between Bolivar Peninsula and Galveston Island.

About 81 percent of the measurement sites on the upper Texas coast (2,273 of 2,819) showed net shoreline retreat from the 1930s through 2019. Net rates at individual measuring points on the upper Texas coast range from retreat at 11.6 m/yr (38 ft/yr) to advance at 14.2 m/yr (47 ft/yr). Net land loss since 1930 is estimated to be 1,814 ha (4,482 ac) between Sabine Pass and Rollover Pass and 87 ha (215 ac) on Galveston Island (table 4). There was a net land gain of 67 ha (166 ac) on Bolivar Peninsula west of Rollover Pass. Long segments of retreating shorelines extend from near Sabine Pass to High Island, along Bolivar Peninsula near Gilchrist and southwest of Crystal Beach, and on Galveston Island from the west end of the seawall to near San Luis Pass (fig. 17). Areas of net advance are limited, but include a 3-km (2-mi)-long segment at Sea Rim State Park and McFaddin National Wildlife Refuge, a short shoreline segment adjacent to the south jetty at Sabine Pass, shoreline segments extending 7.3 km (4.5 mi) north and 12 km (7.5 mi) south of the jetties at Bolivar Roads, and the southwestern end of Galveston Island extending about 4.3 km (2.7 mi) from San Luis Pass.

The shoreline between Sabine Pass and Rollover Pass has the highest rate of net shoreline retreat (3.03 m/yr [9.9 ft/yr]) observed on the Texas coast between the 1930s and 2019 (table 4). Conversely, Bolivar Peninsula and Galveston Island have among the lowest net rates of shoreline movement since the 1930s: there is net shoreline advance at 0.28 m/yr (0.9 ft/yr) on Bolivar

Peninsula, whereas Galveston Island shorelines retreated at a low net rate of 0.21 m/yr (0.7 ft/yr). In these areas, shoreline advance adjacent to the Bolivar Roads jetties offsets shoreline retreat farther from the jetties. On Galveston Island, for example, the East Beach area adjacent to the jetty advanced at a net rate of 3.66 m/yr (12.0 ft/yr) between the 1930s and 2019, whereas Galveston Island shorelines west of the seawall retreated at average net rates of 0.93 m/yr (3.0 ft/yr) during the same period.

Comparisons of long-term (1930s to 2019) rates on the upper Texas coast (fig. 17; table 4) with those calculated for the most recent period (2000 to 2019) (fig. 18; table 5) show similar patterns of shoreline movement. Since 2000, most of the shoreline northeast of Rollover Pass has retreated, with the exception of the Sea Rim State Park area, where the shoreline underwent net advance during the most recent monitoring period. Relatively high and accelerating rates of retreat on the upper coast between Sabine Pass and Rollover Pass (average rates of retreat at 4.49 m/yr [14.7 ft/yr] along this segment between 2000 and 2019) are the highest for the period on the entire coast (fig. 16). Bolivar Peninsula, the only major geomorphic feature showing long-term net advance, underwent net retreat at 0.88 m/yr (2.9 ft/yr) during the 2000 to 2019 period (fig. 16). For Galveston Island as a whole, minimal average net retreat rates between the 1930s and 2019 contrast with average short-term net rates of advance of 0.77 m/yr (2.5 ft/yr) between 2000 and 2019. The eastern and western ends of Galveston Island underwent net shoreline advance between 2000 and 2019, while the central part of the island west of the seawall was stable to erosional.

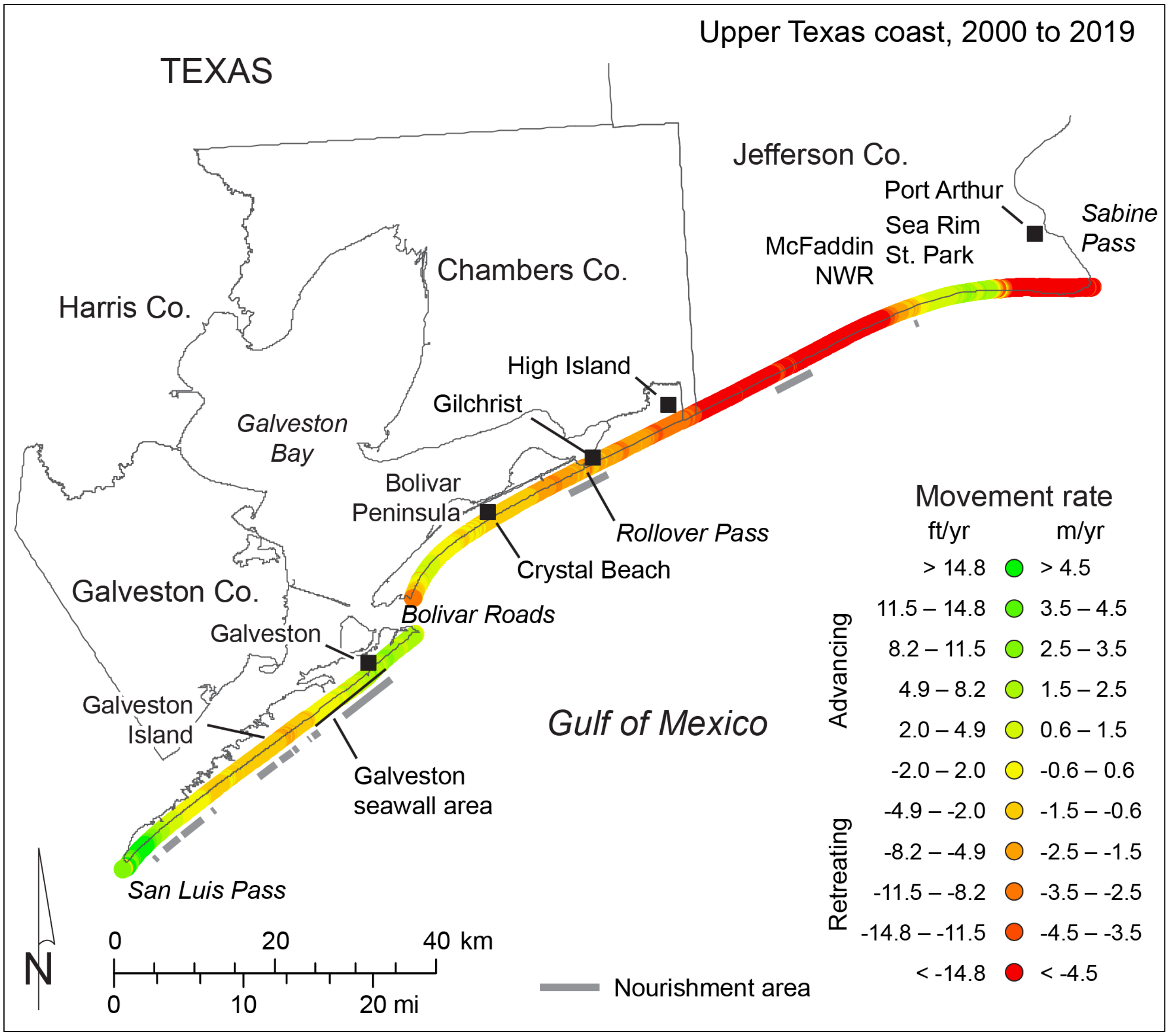

Figure 18. Net rates of recent, short-term movement for the upper Texas Gulf shoreline between Sabine Pass and San Luis Pass (Sabine chenier, Trinity headland, and Galveston Island, fig. 15) calculated from shoreline positions between 2000 and 2019 (table 3). Nourishment and restoration areas are listed in Appendix B.

Brazos–Colorado Headland and Adjacent Peninsulas (San Luis Pass to Pass Cavallo)

Between San Luis Pass and Pass Cavallo lie the headland of the Brazos and Colorado river deltas and adjacent barrier peninsulas: Follets Island and Matagorda Peninsula (figs. 14 and 19). This segment includes about 143 km (89 mi) of Gulf of Mexico shoreline. Major geologic features are (1) Follets Island, a narrow, sandy barrier peninsula extending northeastward from the Brazos headland toward San Luis Pass; (2) the Brazos–Colorado deltaic headland, consisting of

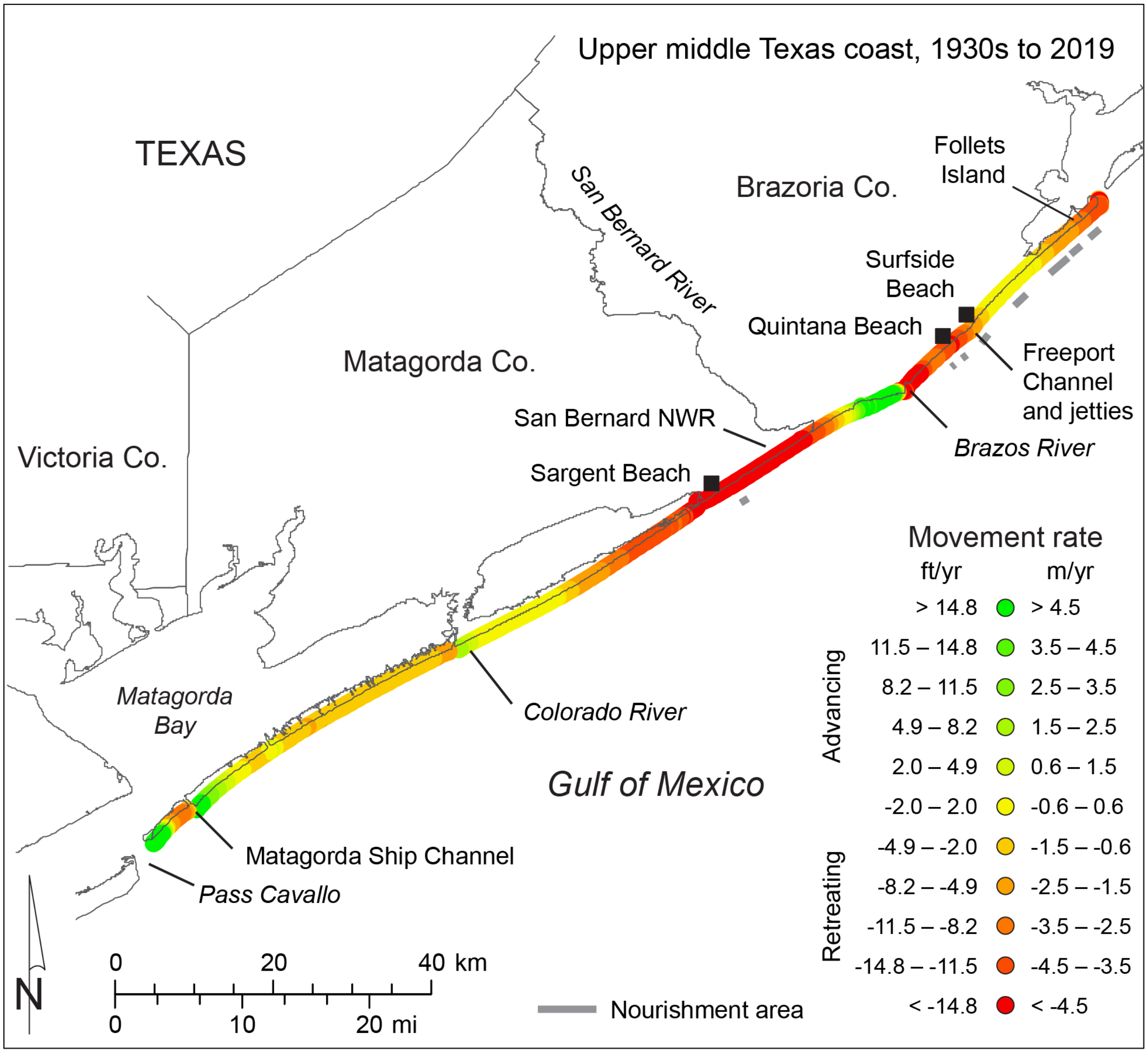

Figure 19. Net rates of long-term movement for the Texas Gulf shoreline between San Luis Pass and Pass Cavallo (Brazos and Colorado headland, Follets Island, and Matagorda Peninsula; fig. 14) calculated from shoreline positions between the 1930s and 2019 (table 3). Nourishment and restoration areas are listed in Appendix B.

semiconsolidated, muddy and sandy sediments deposited by the Brazos and Colorado rivers and overlain by a discontinuous, thin veneer of sandy beach deposits; and (3) Matagorda Peninsula, a narrow, sandy barrier peninsula extending southwestward from the Brazos–Colorado headland from Sargent Beach to Pass Cavallo. Sediments eroded by waves at the headland contribute sand to the flanking barrier peninsulas. In addition, the Brazos and Colorado rivers historically brought sediment to the coast from their large drainage basins. The drainage basin of the Brazos River covers more than 116,000 km^2 (45,300 mi^2) in Texas and eastern New Mexico, but its capacity for carrying sediment to the coast during major floods has been reduced by completion of several dams and reservoirs between 1941 and 1969 (Possum Kingdom, Whitney, Granbury, and DeCordova Bend). The drainage basin of the Colorado is nearly as large (103,000 km^2) [41,600 mi^2], but its sediment load has also been reduced by nine dams completed in the upper and central basins between 1937 and 1990 (Buchanan, Inks, Tom Miller, Mansfield, Wirtz, Starcke, Thomas, Lee, and Ivie), reductions in flood frequency and flow, and diversion into Matagorda Bay. This segment of Gulf shoreline has been compartmentalized by jetties and dredged channels. Between Quintana Beach and Surfside Beach, the Freeport jetties extend about 1,000 m (3,300 ft) from the shoreline to reduce dredging needs of the Freeport Ship Channel, which has been dredged to a depth of 14 m (45 ft). On Matagorda Peninsula, shorter jetties extend 140 to 240 m (460 to 790 ft) seaward from the mouth of the Colorado River. The Matagorda Ship Channel, maintained at a depth of 11 m (36 ft) near the southwestern end of Matagorda Peninsula, is flanked by jetties that extend 880 m (2,900 ft) (north jetty) and 1,600 m (5,250 ft) (south jetty) into the Gulf. Sand has been added to the system artificially during beach nourishment and dune restoration projects on Follets Island and in the Surfside Beach, Quintana Beach, and Sargent Beach areas (fig. 19; table B1 and fig. B2, Appendix B).

There was net shoreline retreat at 2,327 of 2,833 measurement sites (82 percent) between San Luis Pass and Pass Cavallo between the 1930s and 2019 (fig. 19). Net rates of change through 2019 ranged from retreat at 13.1 m/yr (43.2 ft/yr) to advance at 22.0 m/yr (72.0 ft/yr). Notable areas of long-term shoreline retreat include Follets Island, the Brazos–Colorado headland between Surfside Beach and the mouth of the Brazos River and from the mouth of the San Bernard River to Sargent Beach (including the frontage of the San Bernard Wildlife Refuge), Matagorda Peninsula southwest of Sargent Beach, and Matagorda Peninsula southwest of the Matagorda Ship Channel (fig. 19). Shorelines having net long-term advance include a 3.2-km (2.0 mi)-long segment on the Brazos–Colorado headland northeast of Surfside Beach, a 7.7-km (4.8-mi)-long segment southwest of the mouth of the Brazos River, and short segments on Matagorda Peninsula that include a 2.5-km (1.6-mi) long segment northeast of the mouth of the Colorado River, a 6.3-km (3.9-mi)-long segment adjacent to the north jetty at the Matagorda Ship Channel, and a 2.4-km (1.5-mi)-long segment at the southwestern tip of Matagorda Peninsula.

Average net movement on the Brazos–Colorado headland (including Follets Island) between the 1930s and 2019 was retreat at 2.16 m/yr (7.1 ft/yr) (fig. 16; table 4), translating to a net land-loss rate of 13.4 ha/yr (33.1 ac/yr). Total land loss on the headland since 1930 is estimated to be 1,194 ha (2,950 ac) (table 4). Average long-term retreat rates are 0.89 m/yr (2.9 ft/yr) on Matagorda Peninsula. Land-loss rates on Matagorda Peninsula are estimated at 7.1 ha/yr (17.5 ac/yr) between the 1930s and 2019. Total land loss on Matagorda Peninsula between 1930 and 2019 is estimated to be 631 ha (1,558 ac).

During the most recent short-term monitoring period between 2000 and 2019, shoreline movement patterns are similar to those of the long-term period, but rates are generally less recessional (figs. 19 and 20). Average net rates of retreat on the Brazos–Colorado headland decreased to 1.66 m/yr (5.5 ft/yr) (fig. 16; table 5). On Matagorda Peninsula, there was net shoreline retreat at 0.20 m/yr (0.7 ft/yr) between 2000 and 2019. Advancing shoreline segments were more extensive in the most recent period; significant shoreline advance was measured along much of Follets Island (except near San Luis Pass), between the Brazos River and the San Bernard River, on Matagorda Peninsula northeast of the mouth of the Colorado River, and on the southwestern part of Matagorda Peninsula (fig. 20).

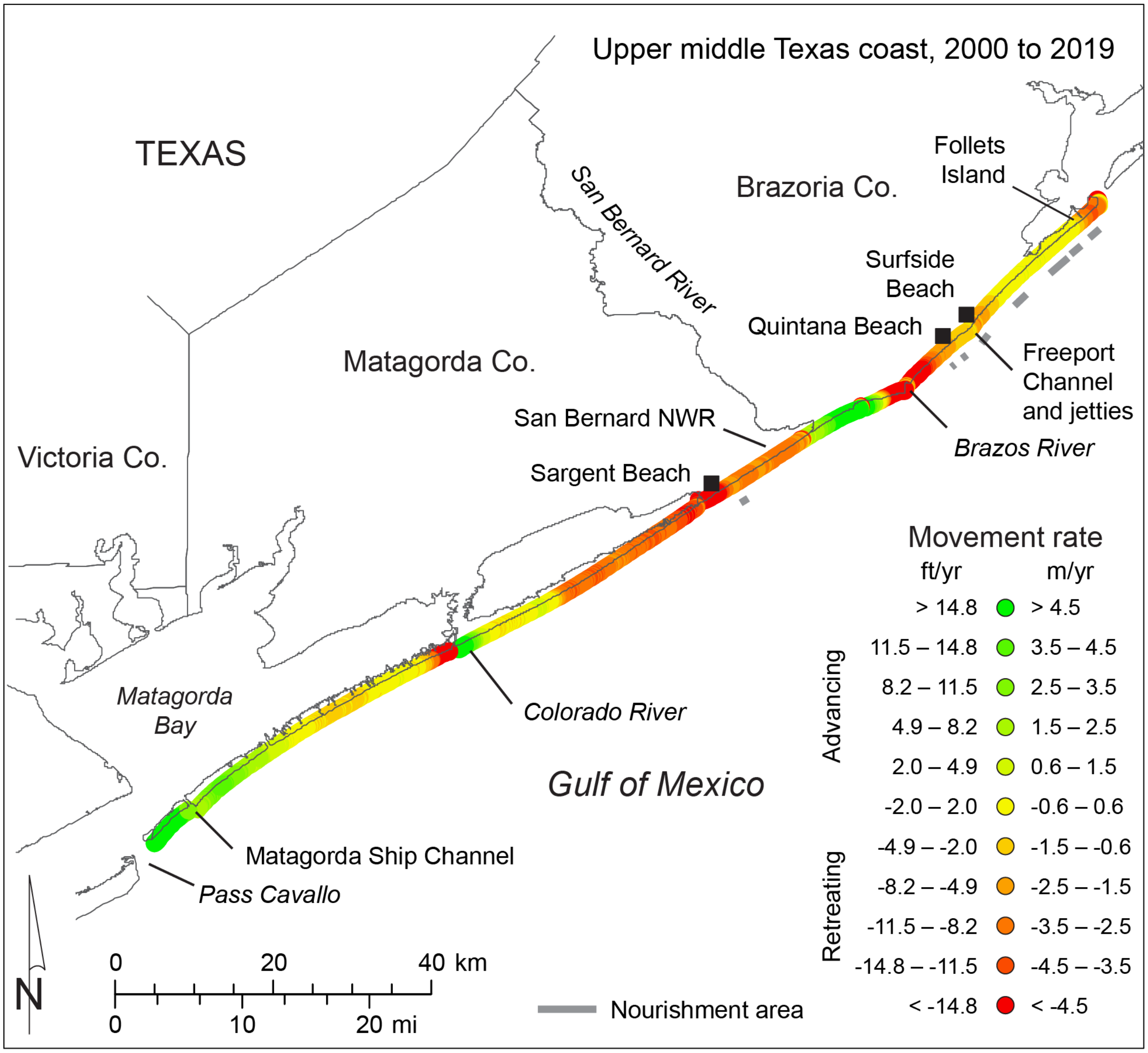

Figure 20. Net rates of recent, short-term movement for the Texas Gulf shoreline between San Luis Pass and Pass Cavallo (Brazos and Colorado headland, Follets Island, and Matagorda Peninsula; fig. 15) calculated from shoreline positions between 2000 and 2019 (table 3). Nourishment and restoration areas are listed in Appendix B.

Middle Texas Coast (Pass Cavallo to Packery Channel)

Gulf shorelines along the middle Texas coast between Pass Cavallo and Packery Channel include those on three sandy barrier islands: Matagorda Island, San José Island, and Mustang Island (figs. 15 and 21). These generally sand-rich islands are characterized by broad, sandy beaches and dune systems that reflect the position of the islands within a longshore current convergence zone between the Brazos–Colorado and Rio Grande fluvial and deltaic headlands. The natural

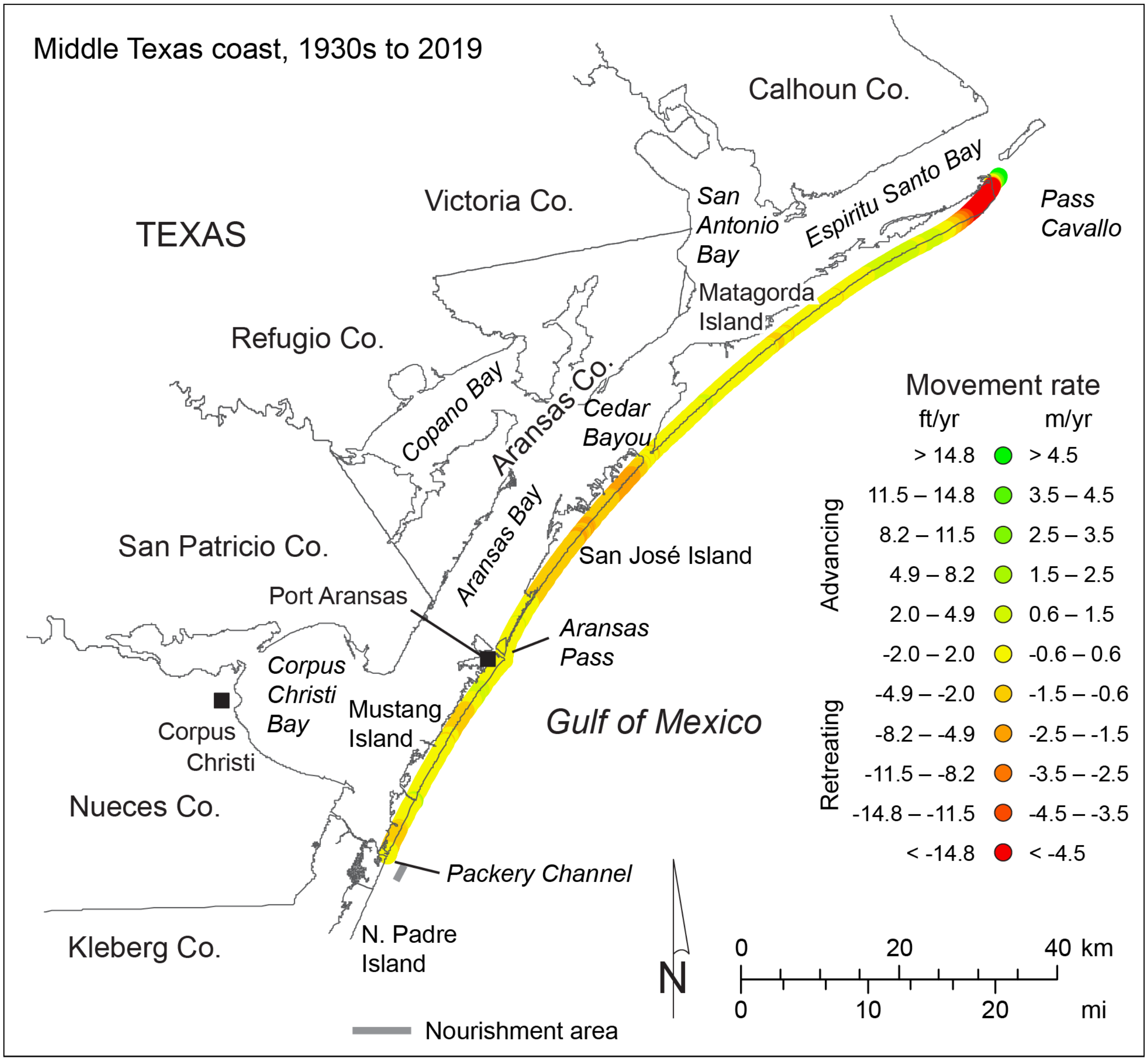

Figure 21. Net rates of long-term movement for the middle Texas Gulf shoreline between Pass Cavallo and the Packery Channel area (Matagorda Island, San José Island, and Mustang Island) calculated from shoreline positions between the 1930s and 2019 (table 3). Nourishment and restoration areas are listed in Appendix B.

boundaries between these three islands are Cedar Bayou, a tidal inlet between Matagorda and San José Islands, and Aransas Pass, a tidal inlet between San José and Mustang Islands. No rivers directly reach the Gulf within this segment.

Engineered structures that have compartmentalized the nearshore system are (1) the Matagorda Ship Channel and jetties that restrict sediment transport to Matagorda Island from the northeast, and (2) the jetties at Aransas Pass, which protect the dredged, 14-m (47-ft) deep Corpus Christi Ship Channel. Plans are underway to deepen the Corpus Christi channel to 16 m (52 ft). These jetties extend 1,100 to 1,200 m (3,600 to 3,950 ft) gulfward from the shoreline, interrupting bidirectional longshore sand exchange between Mustang Island and San José Island. Smaller structures with possible local effects include the closed Fish Pass on Mustang Island, where the former dredged channel is filled but short jetties that extend about 150 m (500 ft) from the shoreline remain; and Packery Channel, a shallow channel between Mustang Island and Padre Island that has been dredged to a nominal depth of 3 m (10 ft) and is protected by jetties that reach 300 m (1,000 ft) (north jetty) and 365 m (1,200 ft) (south jetty) seaward of the Gulf shoreline.

Long-term Gulf shoreline change rates within this segment of the Texas coast were calculated at 2,312 sites over a distance of 115 km (71 mi) between Pass Cavallo and the southern end of Mustang Island (table 4; fig. 21). Net shoreline change rates calculated from the 1930s to 2019 averaged retreat at 0.91 m/yr (3.0 ft/yr) for Matagorda Island, retreat at 0.84 m/yr (2.8 ft/yr) for San José Island, and retreat at 0.29 m/yr (1.0 ft/yr) for Mustang Island. Annual rates of land loss estimated from these rates are 5.1 ha/yr (12.5 ac/yr) on Matagorda Island, 2.6 ha/yr (6.4 ac/yr) on San José Island, and 0.83 ha/yr (2.1 ac/yr) on Mustang Island. Estimated total land loss along the Gulf shoreline since 1930 is 452 ha (1,116 ac) on Matagorda Island, 231 ha (572 ac) on San José Island, and 74 ha (183 ac) on Mustang Island.

Two-thirds of measuring sites underwent net shoreline retreat (1,562 of 2,312; 68 percent) from 1930 to 2019. Net rates at individual sites ranged from retreat at 16.5 m/yr (54.3 ft/yr) to advance at 14.4 m/yr (47.3 ft/yr). Almost 40 percent of the Gulf shoreline along Matagorda Island has advanced since the 1930s, albeit at low rates except along a short segment where the island has migrated toward Pass Cavallo at its northeastern end (fig. 21). Sites along short shoreline segments (6.3 to 7.2 km [3.9 to 4.5 mi] long) near the north and south jetties at Aransas Pass recorded minor net shoreline advance. Highest rates of net retreat (more than 3 m/yr [10 ft/yr]) were measured along a 6.2-km (3.8-mi)-long segment of Matagorda Island near Pass Cavallo. Net retreat rates greater than 1 m/yr (3.3 ft/yr) were measured along a 17-km (10.5 mi)-long segment of San José Island southwestward from Cedar Bayou and along a 2.7-km (1.7-mi)-long segment on the southern part of Mustang Island. Net retreat rates elsewhere were less than about 1 m/yr (3 ft/yr).

Net rates of retreat on Matagorda Island are higher for the more recent (2000 to 2019) monitoring period than they are for the longer-term period (figs. 16 and 22). The average long-term retreat rate of 0.91 m/yr (3.0 ft/yr) increased to 1.65 m/yr (5.4 ft/yr) from 2000 to 2019. Recent short-term trends on San José Island are less erosional; average net retreat rates of 0.84 m/yr (2.8 ft/yr) between the 1930s and 2019 changed to average net retreat rates of 0.07 m/yr (0.2 ft/yr) over the most recent period (2000 to 2019, fig. 22). On Mustang Island, low average rates of long-term net retreat at 0.29 m/yr (1.0 ft/yr) changed to slight net advance at 0.15 m/yr (0.5 ft/yr) during the most recent monitoring period (2000 to 2019). Mustang Island was one of only two geologic features on the Texas coast having net shoreline advance from 2000 to 2019 (fig. 16).

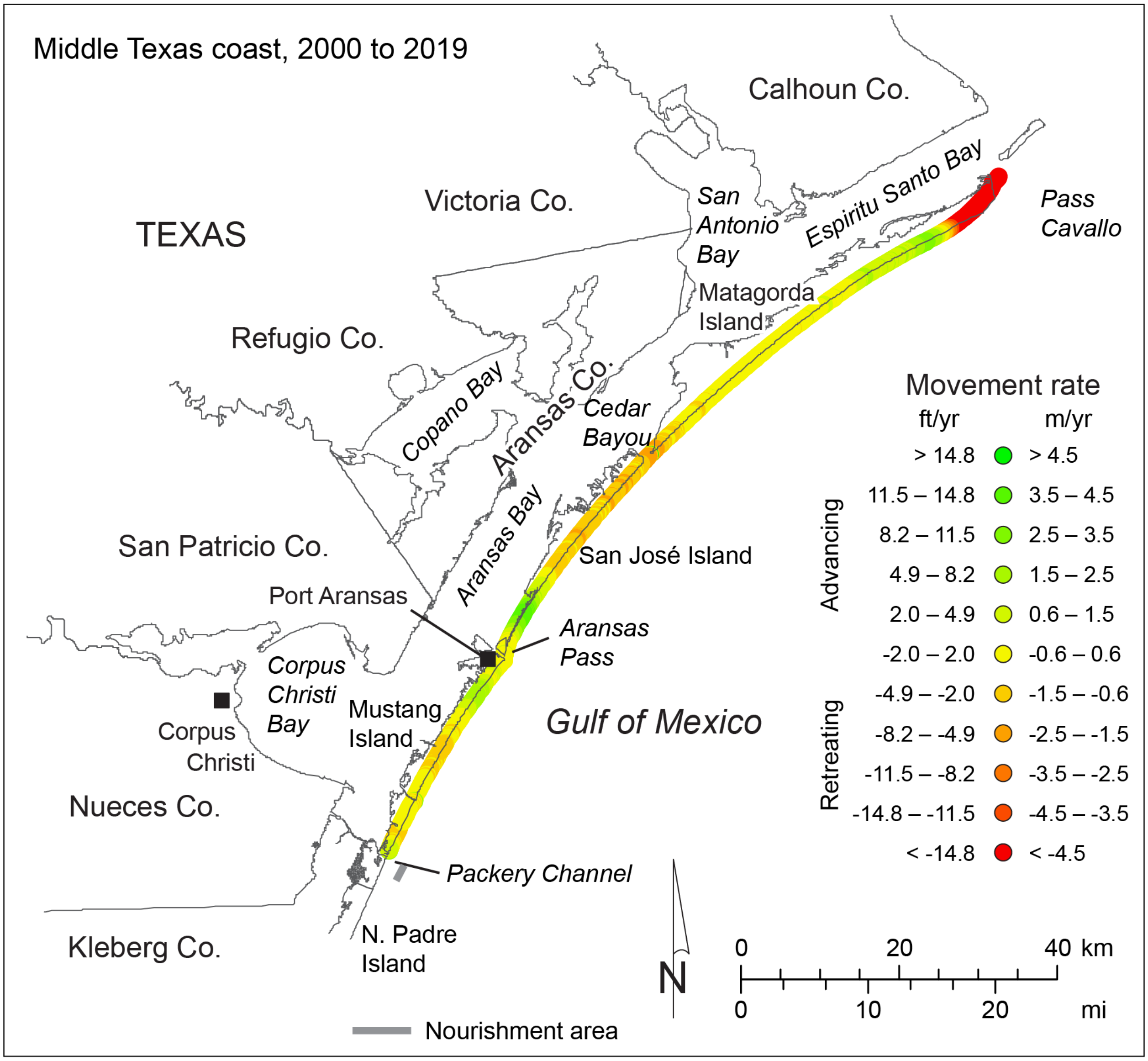

Figure 22. Net rates of recent, short-term movement for the middle Texas Gulf shoreline between Pass Cavallo and the Packery Channel area (Matagorda Island, San José Island, and Mustang Island) calculated from shoreline positions between the 2000 and 2019 (table 3). Nourishment and restoration areas are listed in Appendix B.

Lower Coast (Padre Island and Brazos Island)

The lower coast segment encompasses 188 km (117 mi) of Gulf shoreline between Packery Channel and the mouth of the Rio Grande (figs. 14 and 23). The principal natural geomorphic feature in this area is Padre Island, a long Holocene barrier island that broadens from a narrow peninsula at Brazos Santiago Pass to a broad, sandy barrier island having a well-developed dune system throughout most of its length. Brazos Island is a short barrier island that extends southward toward the Rio Grande from Brazos Santiago Pass. The Rio Grande enters the Gulf of Mexico at the southern end of this segment and has created a large fluvial and deltaic headland that forms the southern boundary of a regional longshore current cell that is bounded on the north by the Brazos–Colorado headland. Net longshore drift is northward on the southern part of Padre Island and southward on the northern part of the island. The Rio Grande has a large drainage basin (471,900 km^2 [182,200 mi^2]) that extends into Mexico, New Mexico, and Colorado, but dams constructed on the middle and lower parts of the basin in 1954 (Falcon) and 1969 (Amistad), combined with extensive irrigation use of Rio Grande water on the coastal plain, has reduced the sediment delivered to the coast.

Most of Padre Island is undeveloped, except for intensive development at its northern extremity and at the southern tip of the island (the city of South Padre Island). Engineering structures that have affected shoreline position include (1) the jetties and associated ship channel at Brazos Santiago Pass, where the 13-m (44-ft) deep channel is flanked by jetties that reach 870 m (2,850 ft) (north jetty) and 490 m (1,600 ft) (south jetty) into the Gulf; and (2) the shallower Port Mansfield Channel and its 620-m (2,030 ft) north jetty and 140-m (460 ft) south jetty that protect the 5-m (15-ft) deep channel. Plans are underway to deepen the ship channel to 16 m (54 ft). Sand has been artificially added to the beach and nearshore system during numerous projects on southern Padre Island and near Packery Channel at the northern end of the island (fig. 23; table B1 and fig. B4, Appendix B).

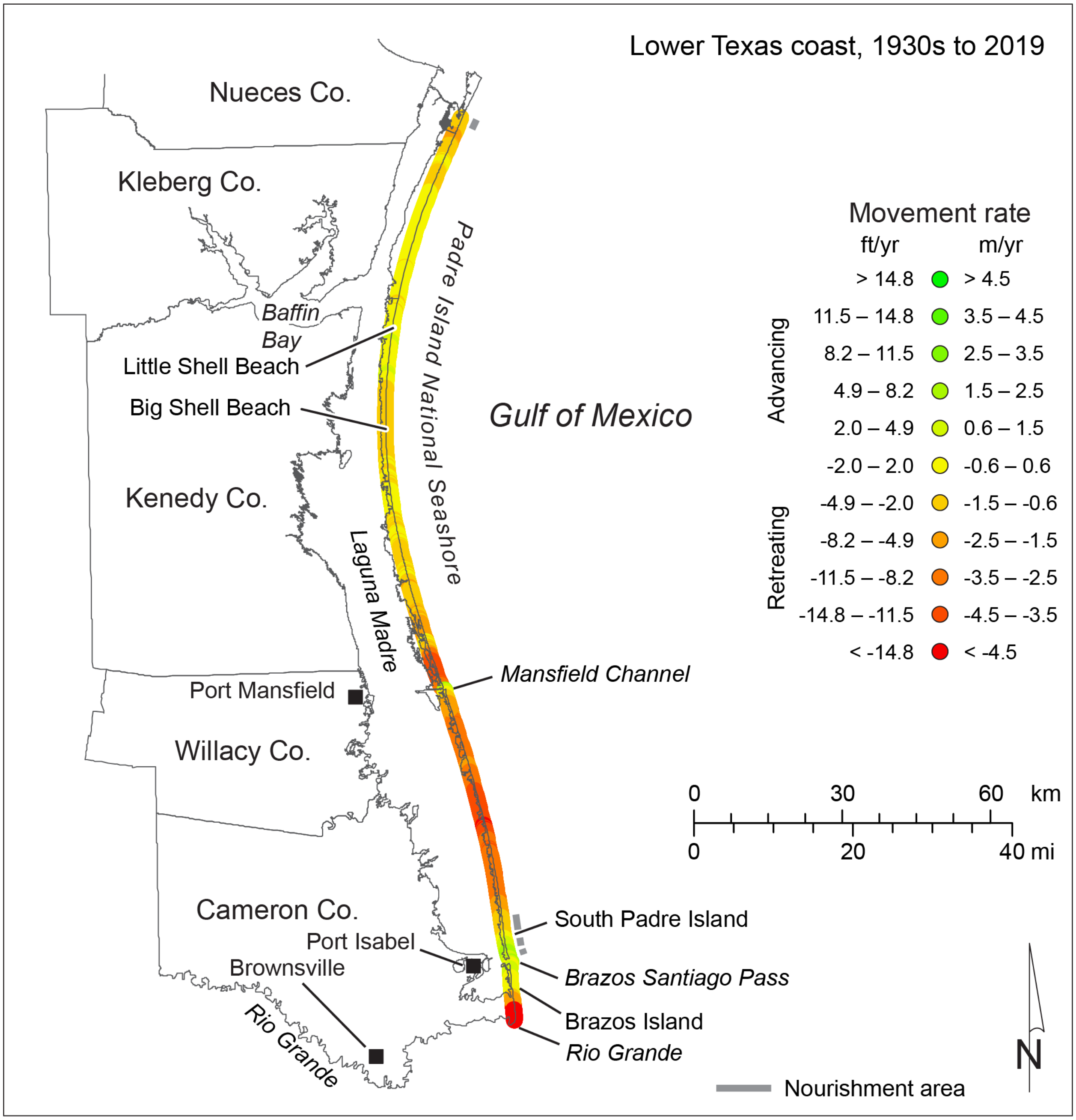

Figure 23. Net rates of long-term movement for the lower Texas Gulf shoreline between Packery Channel and the Rio Grande (Padre Island and Brazos Island) calculated from shoreline positions between the 1930s and 2019 (table 3). Nourishment and restoration areas are listed in Appendix B.

Despite the favorable location of much of Padre Island in a longshore drift convergence zone, the shoreline retreated at 3,174 of 3,758 measurement sites (85 percent) between the 1930s and 2019 (fig. 23). Net change rates ranged from retreat at 7.2 m/yr (23.6 ft/yr) to advance at 2.8 m/yr (9.1 ft/yr). Average long-term net shoreline movement rates are retreat at 0.77 m/yr (2.5 ft/yr) on northern Padre Island (Mansfield Channel to Packery Channel), 2.46 m/yr (8.1 ft/yr) on southern Padre Island (Mansfield Channel to Brazos Santiago Pass), and 1.57 m/yr (5.2 ft/yr) on Brazos Island (fig. 23, table 4). Estimated net land loss since 1930 is 820 ha (2,026 ac) along northern Padre Island, 1,227 ha (3,032 ac) along southern Padre Island, and 163 ha (405 ac) along Brazos Island.

Net advancing shorelines include a 13.3-km (8.3-mi)-long segment in the Little Shell Beach area on Padre Island National Seashore near Baffin Bay, a 1-km (0.6-mi)-long segment adjacent to the south jetty at Mansfield Channel, and two nearly 5-km (3-mi)-long segments adjacent to the north and south jetties at Brazos Santiago Pass (fig. 23). Highest rates of net retreat (greater than 3 m/yr [10 ft/yr]) were measured along a 7-km (4-mi)-long segment north of the Mansfield Channel jetties, a 22-km (13.7-mi)-long segment on southern Padre Island, and a 2.8-km (1.7-mi)-long segment near the Rio Grande (fig. 23).

During the most recent, short-term monitoring period (2000 to 2019), net shoreline movement on the lower Texas coast was similar to the long-term average (figs. 16, 23, and 24). Northern Padre Island, the segment on the lower coast with the lowest long-term average retreat rate at 0.77 m/yr (2.5 ft/yr), underwent slightly higher net retreat at 0.82 m/yr (2.7 ft/yr) between 2000 and 2019 (fig. 16; table 5). Net average retreat rates for the most recent period are 1.99 m/yr (6.5 ft/yr) for southern Padre Island, lower than the long-term average of 2.46 m/yr (8.1 ft/yr). On Brazos Island, retreat rates for the 2000 to 2019 period are 1.91 m/yr (6.3 ft/yr), higher than the long-term rate of 1.57 m/yr (5.2 ft/yr) for Brazos Island (fig. 16; table 5).

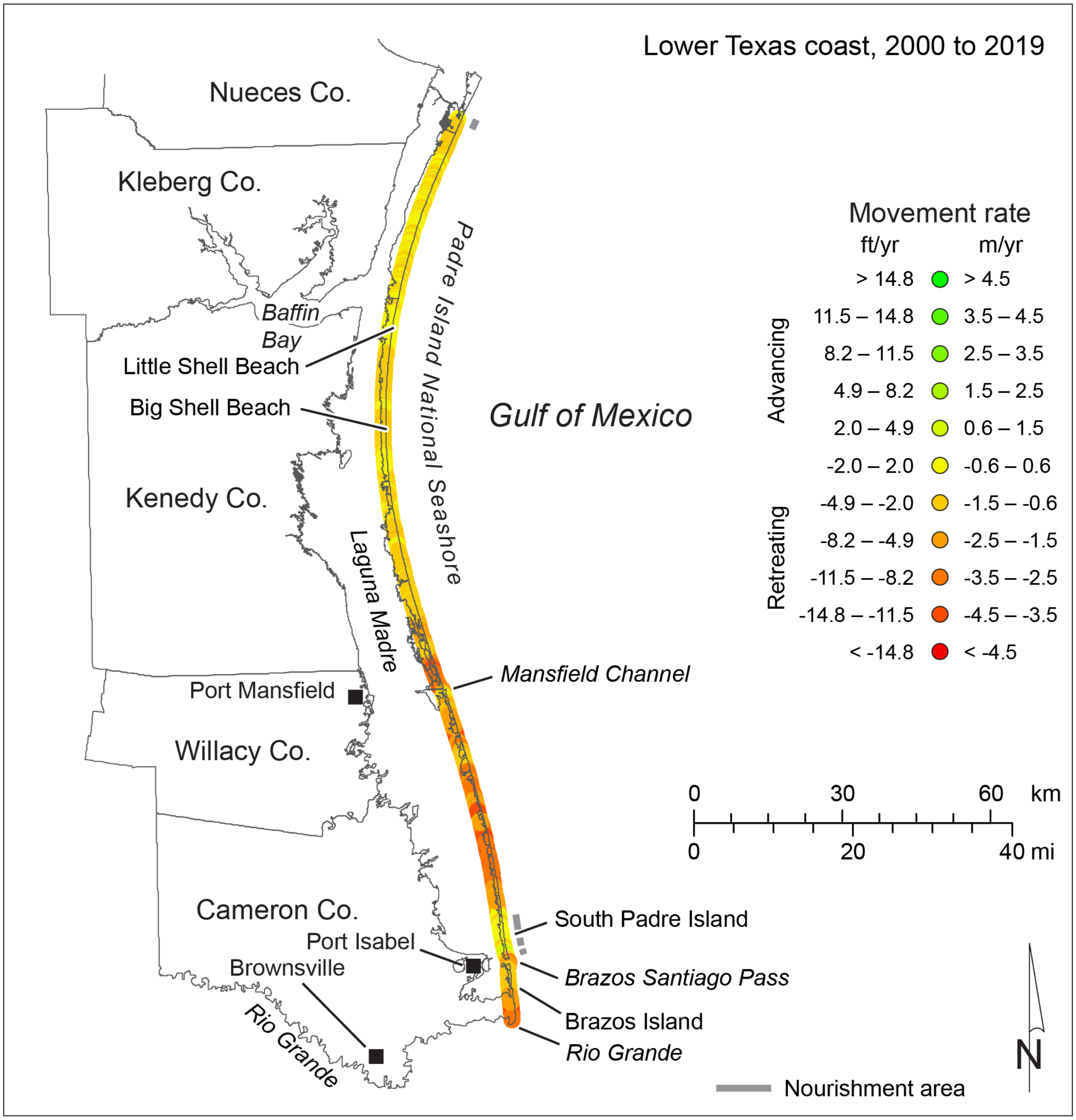

Figure 24. Net rates of recent, short-term movement for the lower Texas Gulf shoreline between Packery Channel and the Rio Grande (Padre Island and Brazos Island) calculated from shoreline positions between 2000 and 2019 (table 3). Nourishment and restoration areas are listed in Appendix B.

LATE PLEISTOCENE TO HOLOCENE CONTEXT

Estimates of shoreline-change rates over recent geologic intervals can provide a longer-term context for historical rates documented from maps, aerial photographs, beach surveys, and airborne surveys acquired over many decades. One simple approach to estimating net change rates since the end of the last glacial maximum about 20 thousand years ago (ka), when sea level was several hundred feet lower than it is today (fig. 25), is to use shelf bathymetric contours (fig. 26) as a proxy for shoreline position at past sea-level elevations. Rates of postglacial shoreline change can be estimated by measuring the shore-normal distance between selected bathymetric contours on the Texas shelf and the present shoreline position and dividing by the

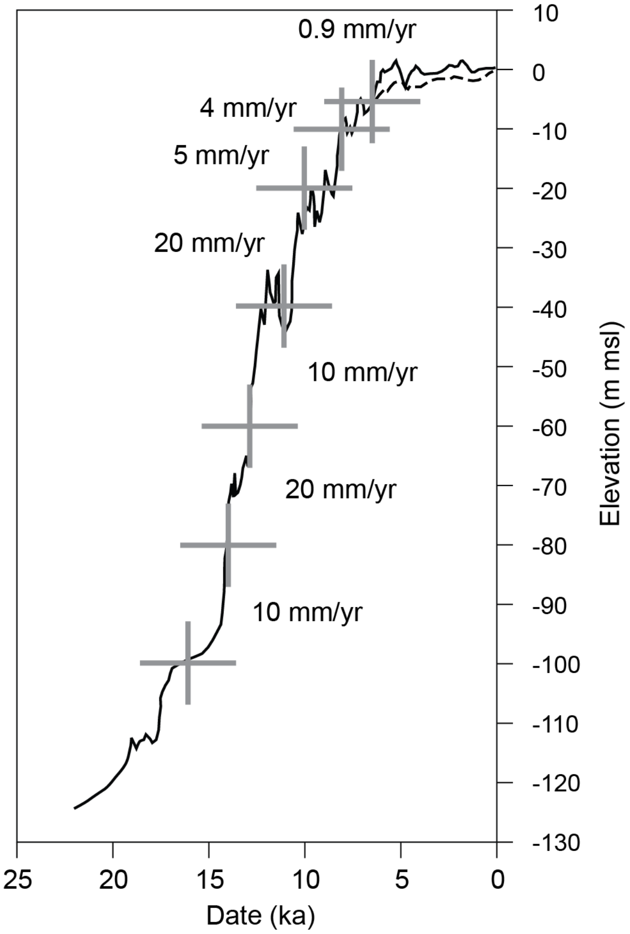

Figure 25. Postglacial Gulf of Mexico sea-level curves (Balsillie and Donoghue, 2004, 2009; Millilken and others, 2008) and approximate rates of relative sea-level rise between 16 and 14 ka, 14 and 13 ka; 13 and 11 ka; 11 and 10 ka; 10 and 8 ka, 8 and 7 ka, and 7 ka to present.

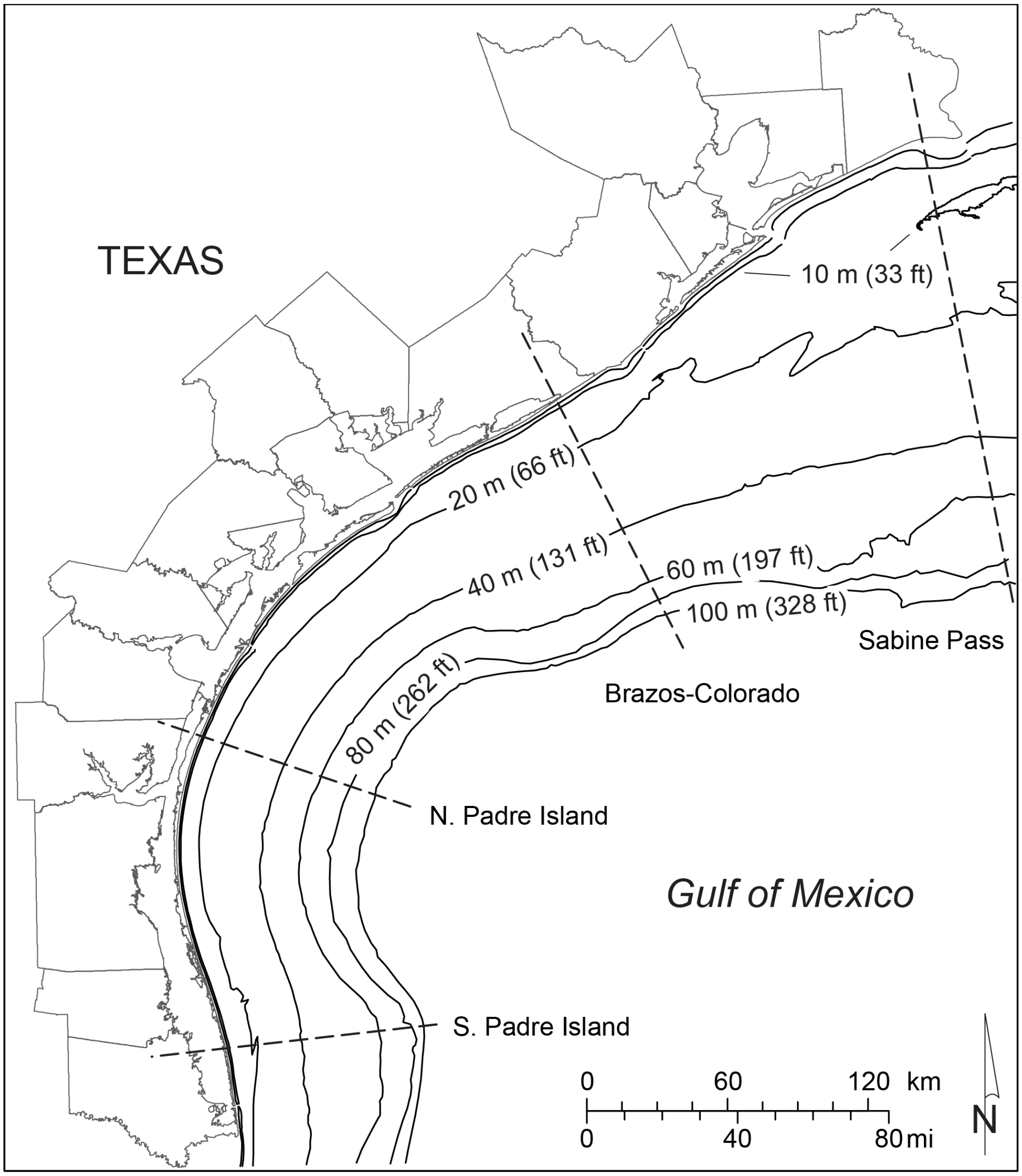

Figure 26. Major bathymetric contours on the Texas continental shelf and transect locations where postglacial net and interval shoreline migration rates are estimated using bathymetric contours as a shoreline proxy. Bathymetric data generalized from Holcombe and Arias (2009).

elapsed time since sea level was at those elevations (table 6). Subsidence, which is likely to vary spatially and temporally, is a substantial source of possible error for this approach. Nevertheless, the impact of subsidence on the rates is partly offset by the fact that the Gulf of Mexico sea-level curves (Balsillie and Donoghue, 2004, 2009; Milliken and others, 2008) have also been constructed without correcting for the effects of subsidence. Holocene shelf sedimentation is another source of error that can be significant (particularly within major incised valleys on the

Table 6. Late Pleistocene and Holocene net shoreline retreat rates for the Texas coast estimated by assuming water depth (fig. 26) approximates shoreline position at past sea-level positions (fig. 25). Effects of subsidence, sedimentation, and erosion are neglected and are significant sources of error. Sea-level ages and elevations are from northern Gulf of Mexico sea level curves published by Balsillie and Donoghue (2004, 2009) and Milliken and others (2008).

		Net rate to present (m/yr)				**Interval rate from previous position (m/yr)**			
Elev. (m msl)	**Age (ka)**	**Sabine Pass**	**Brazos-Colorado**	**N. Padre Island**	**S. Padre Island**	**Sabine Pass**	**Brazos-Colorado**	**N. Padre Island**	**S. Padre Island**
-7	7	-1.0	-0.2	-0.1	-0.1	-6.3	-2.0	-0.7	-0.8
-10	8	-1.7	-0.4	-0.2	-0.2	-33.1	-9.5	-4.4	-5.8
-20	10	-7.9	-2.3	-1.0	-1.3	-55.2	-40.3	-26.7	-18.3
-40	11	-12.2	-5.7	-3.4	-2.9	-13.6	-13.2	-8.2	-16.2
-60	13	-12.4	-6.9	-4.1	-4.9	-28.4	-8.6	-12.6	-13.9
-80	14	-13.6	-7.0	-4.7	-5.6	-4.9	-3.7	-5.6	-2.5
-100	16	-12.5	-6.6	-4.8	-5.2	-	-	-	-

inner continental shelf), but is presumed to be minimal in the context of generalized bathymetric contours extending along the entire continental shelf.

This order-of-magnitude approach yields estimated net retreat rates between 16 ka and the present that range from about 5 to 13 m/yr (16 to 41 ft/yr, table 6), reflecting rapid sea-level rise rates and rapid general shoreline retreat during the late Pleistocene and early Holocene. Higher long-term rates are calculated for the upper coast than for the lower coast. Beginning at about 10 ka, net rates generally decrease along the entire coast as the beginning shoreline position date becomes younger; but the trend of higher retreat rates on the upper coast and lower rates on the lower coast is consistent for each period. From 11 ka to present, for example, estimated retreat rates ranged from 3 m/yr (9 ft/yr) along the southern Padre Island transect to 12 m/yr (40 ft/yr) along the Sabine Pass transect. From 8 ka to present, net rates decreased to 0.2 m/yr (0.6 ft/yr) on Padre Island and 1.7 m/yr (5 ft/yr) at Sabine Pass. Published sea-level curves for the northern Gulf of Mexico (Balsillie and Donoghue, 2004, 2009; Milliken and others, 2008) show a reduction in rates of sea-level rise that began between about 8 and 10 ka that coincides with lower estimated rates of postglacial shoreline retreat.

Shoreline change rates can also be estimated for discrete intervals within the general postglacial sea-level rise by comparing past successive sea-level positions and generalized bathymetric contours as a shoreline proxy (table 6). These data show that estimated net retreat rates were very high before 8 ka, ranging from 3 to 55 m/yr (8 to 181 ft/yr) depending on the interval and location (upper coast rates are generally significantly higher than middle- and lower-coast rates). The highest rates of shoreline retreat occurred between 11 ka and 10 ka, when rates ranged between 18 m/yr (60 ft/yr) along the southern Padre Island transect and 55 m/yr (181 ft/yr) along the Sabine Pass transect. Rates between 8 and 7 ka lowered significantly to 0.7 to 6.3 m/yr (2 to 21 ft/yr), as did those since 7 ka (0.1 to 1 m/yr [0.4 to 3.3 ft/yr]). In this context, historical retreat rates averaging 1.7 m/yr (5.6 ft/yr) on the upper Texas coast and 1.0 m/yr (3.2 ft/yr) on the lower Texas coast (calculated from shoreline positions between the 1930s and 2019, table 4) are significantly lower than late Pleistocene to early Holocene retreat estimates during times of rapid postglacial sea-level rise and are similar to retreat rates estimated since the mid-Holocene when sea-level rise rates decreased.

USING POSTGLACIAL RATES TO PREDICT SHORELINE MOVEMENT

Over postglacial rates of relative sea-level rise that range from 1 to 20 mm/yr at millenial scales (fig. 25), there is a reasonably good empirical relationship (r^2 values of 0.48 to 0.78) between rates of relative sea-level rise and net retreat rates for the upper, upper-middle, lower-middle, and lower coast (fig. 27). The best-fit rate of retreat per millimeter per year of sea-level rise increases from south to north along the Texas coast, ranging from 0.8 m/yr (2.8 ft/yr) on the lower coast to 1.8 m/yr (5.9 ft/yr) on the upper coast (fig. 27). These relationships can perhaps be used to predict approximate rates of shoreline retreat that would be expected under various relative sea-level rise scenarios. At historical rates of relative sea-level rise, for example (2 to 4 mm/yr on the lower and lower-middle coast, 3 to 5 mm/yr on the upper-middle coast, and 5 to 7 mm/yr on

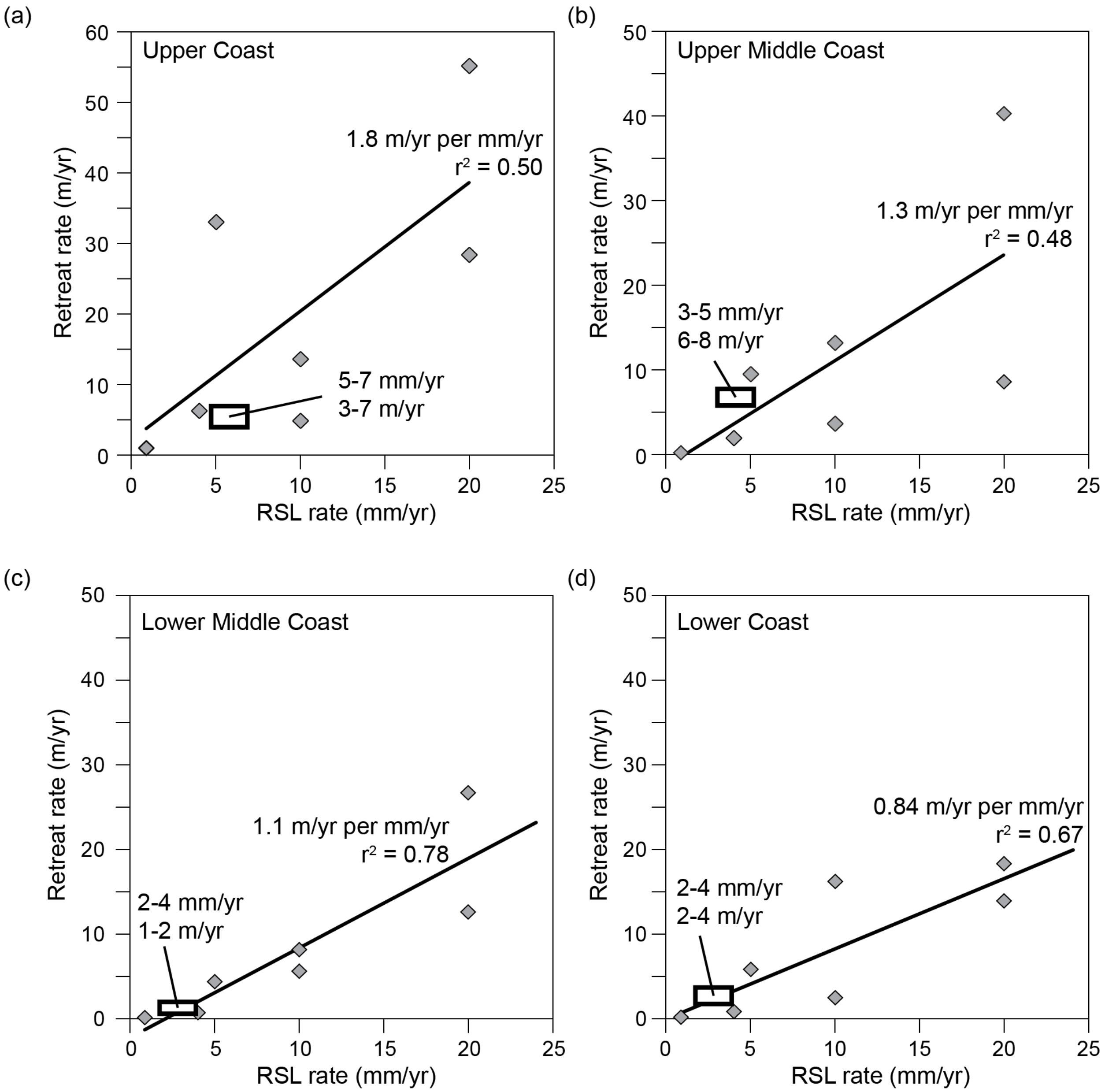

Figure 27. Relationship between postglacial rates of relative sea-level rise (fig. 25) and approximate long-term shoreline retreat rates for (a) the upper-coast, (b) upper-middle coast, (c) lower-middle coast, and (d) lower-coast transects (fig. 26). Boxed areas represent historical retreat rates and historical relative sea-level rise rates.

the upper coast), observed retreat rates of 2 to 4 m/yr (7 to 13 ft/yr) for the lower coast and 1 to 2 m/yr (3 to 7 ft/yr) for the lower-middle coast match predicted rates well (fig. 27c, d). Observed historical retreat rates of 6 to 8 m/yr (20 to 26 ft/yr) for the upper-middle coast are higher than the postglacial relationship would predict, but fall between the postglacial retreat rates calculated for the 8 to 7 ka period (4 mm/yr) and the 10 to 8 ka period (5 mm/yr) (fig. 27b). For the upper coast, historical rates of retreat at 3 to 7 m/yr (10 to 23 ft/yr) are lower than those predicted by the postglacial relationship (fig. 27a), but are nearly identical to the calculated postglacial retreat rate observed for the 8 to 7 ka period when sea-level rose at a similar rate (4 mm/yr).

BEACH AND FOREDUNE VOLUMETRICS

In addition to extracting shoreline position from lidar-derived DEMs to determine shoreline movement rates, DEMs can also be used to determine sediment volumes in the beach and foredune system. Volumes and their relationship to elevation help identify areas where sediment has accumulated, as well as areas where little sediment is stored near the shoreline. Further, peak elevations determined for shoreline segments help identify areas susceptible to breaching and overwash during tropical cyclone passage. Volumetrics data are presented both as peak elevations within each segment of the Texas Gulf shoreline and as volumes above threshold elevations ranging from 1 to 9 m (3 to 30 ft) relative to the NAVD88 elevation datum (all elevations in this discussion use this datum). These volumes can be cast as total volume above a threshold elevation for a given shoreline segment, or as “normalized” alongshore volumes above a threshold elevation, calculated by dividing the volume within the shoreline segment by the alongshore length of the segment.

Coastwide peak-elevation patterns (fig. 28) are similar to coastwise long- and short-term shoreline movement trends (figs. 14 and 15). Peak elevations are generally higher from Matagorda Island southward; peak elevations above 5 m (16 ft) are common on San José Island, Mustang Island, and Padre Island (fig. 28). Northeast of Matagorda Island, peak elevations are generally below 5 m (16 ft). Peak elevations are below 4.5 m (14.8 ft) for about 50 percent of the shoreline and are below 3.5 m (11.5 ft) along about 25 percent of the shoreline (fig. 29).

Normalized alongshore volumes above 1 m (3.3 ft) elevation show similar trends to peak elevations (fig. 30). Greatest volumes above 1 m (3.3 ft) elevation extend south of Matagorda Island to include San José Island, Mustang Island, and the northern half of Padre Island.

Relationships between volume and elevation also vary along the Texas Gulf shoreline (fig. 31). The average volume of sediment above 1 m (3.3 ft) elevation per meter alongshore is about 230 m^3/m (92 yd^3/ft). The average volume decreases at higher threshold elevations to about

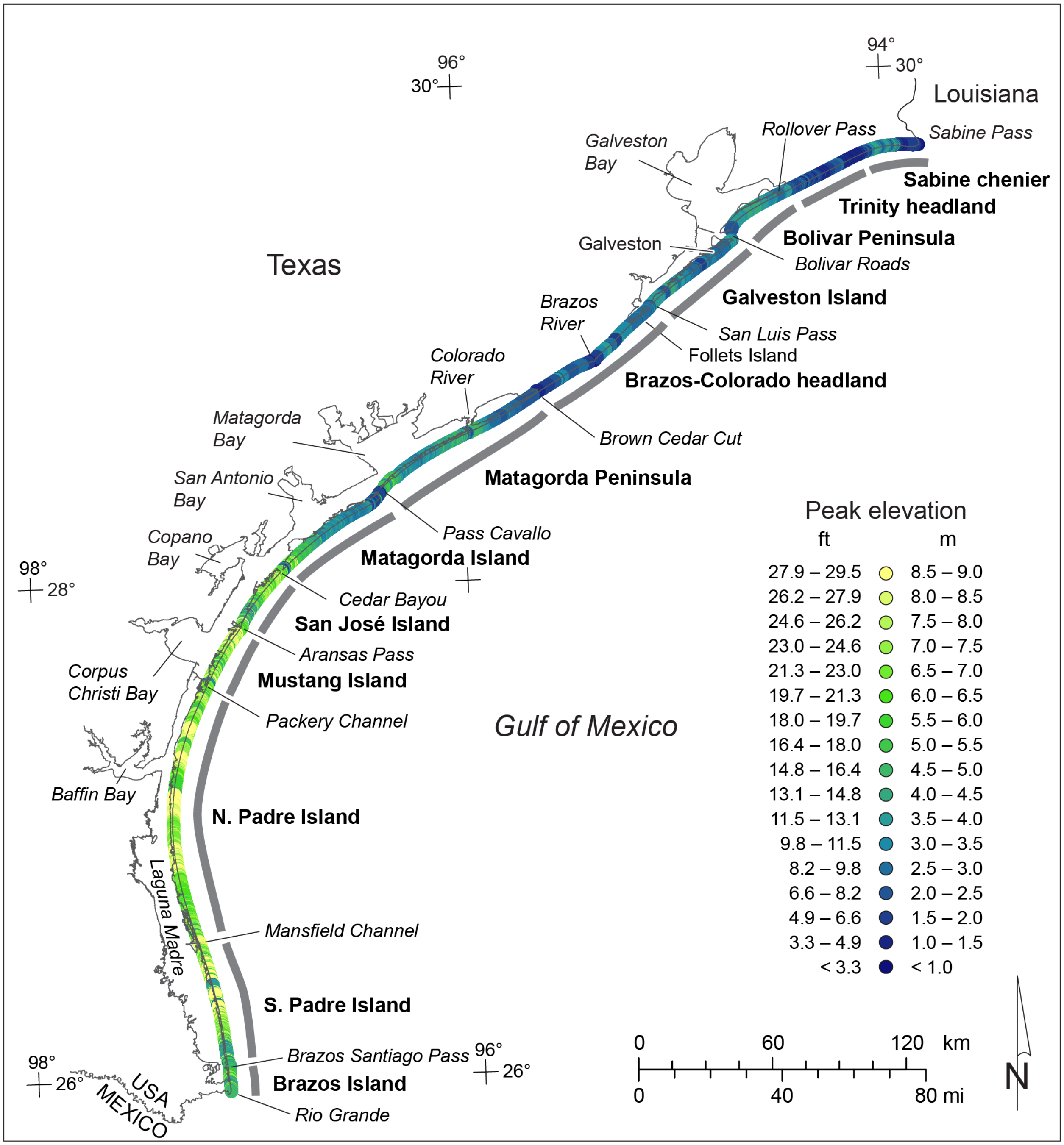

Figure 28. Peak beach and foredune elevation along the Texas Gulf shoreline determined at 50-m intervals from the 2019 airborne lidar survey.

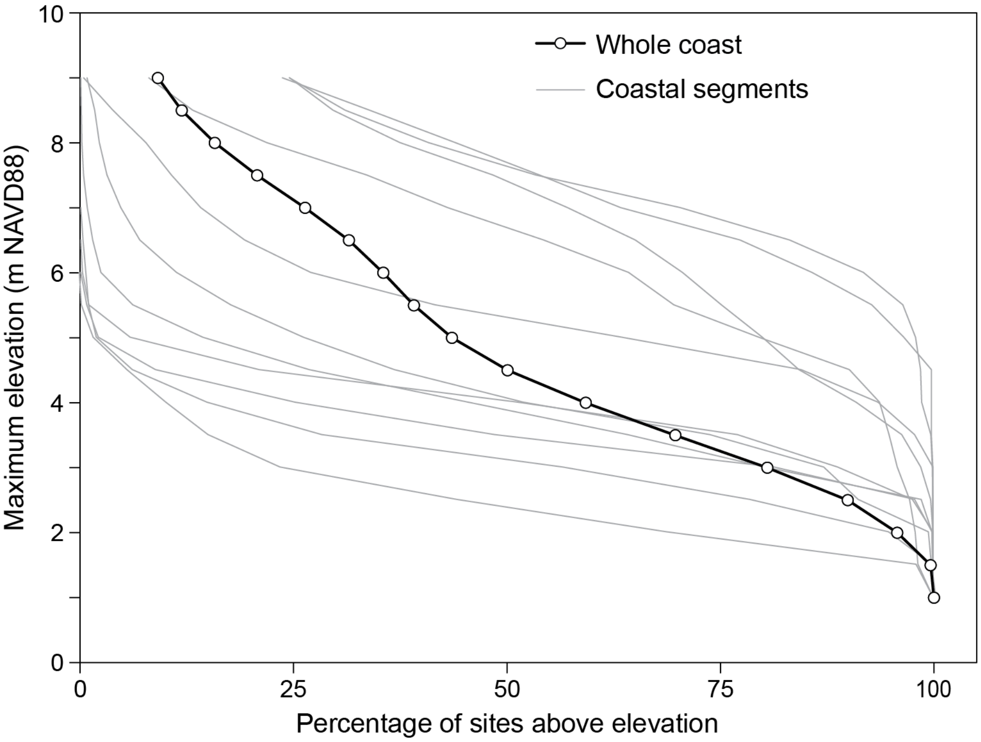

Figure 29. Percentage of the Texas Gulf shoreline having peak beach and foredune elevations above threshold elevations ranging from 1 to 9 m.

104 m^3/m (41 yd^3/ft) above 2.5 m (8.2 ft) elevation and to 50 m^3/m (20 yd^3/ft) above 4.5 m (14.8 ft) elevation.

Data from the 2019 lidar survey were also used to estimate total sediment volume above elevations ranging from 1 to 9 m (3 to 30 ft) for the Texas Gulf beach and foredune system as a whole (table 7). Total estimated volumes decrease from nearly 133,000,000 m^3 (174,000,000 yd^3) above 1 m (3 ft) to about 426,000 m^3 (557,000 yd^3) above 9 m (30 ft).

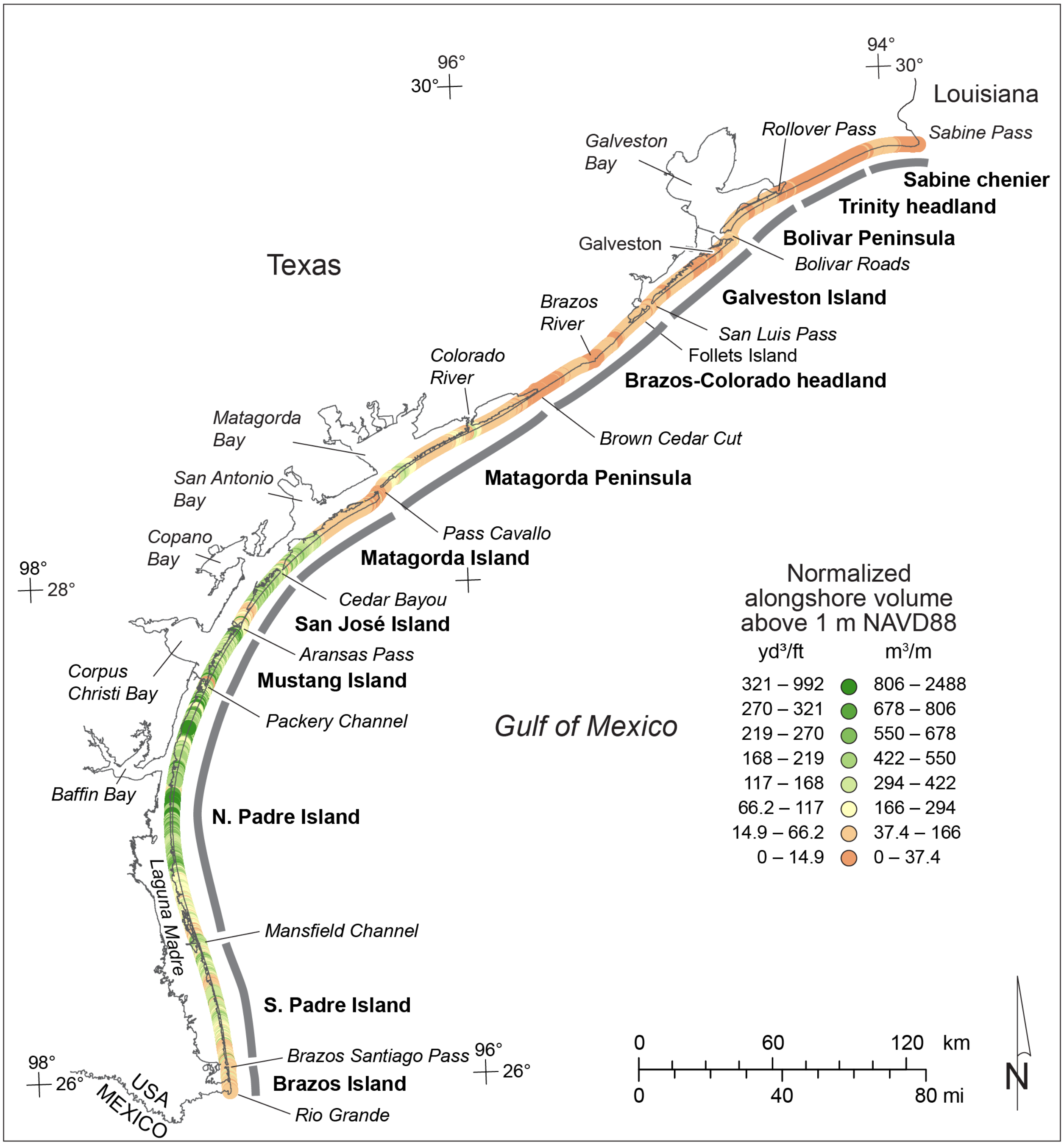

Figure 30. Normalized beach and foredune volume above 1 m elevation for the Texas Gulf shoreline.

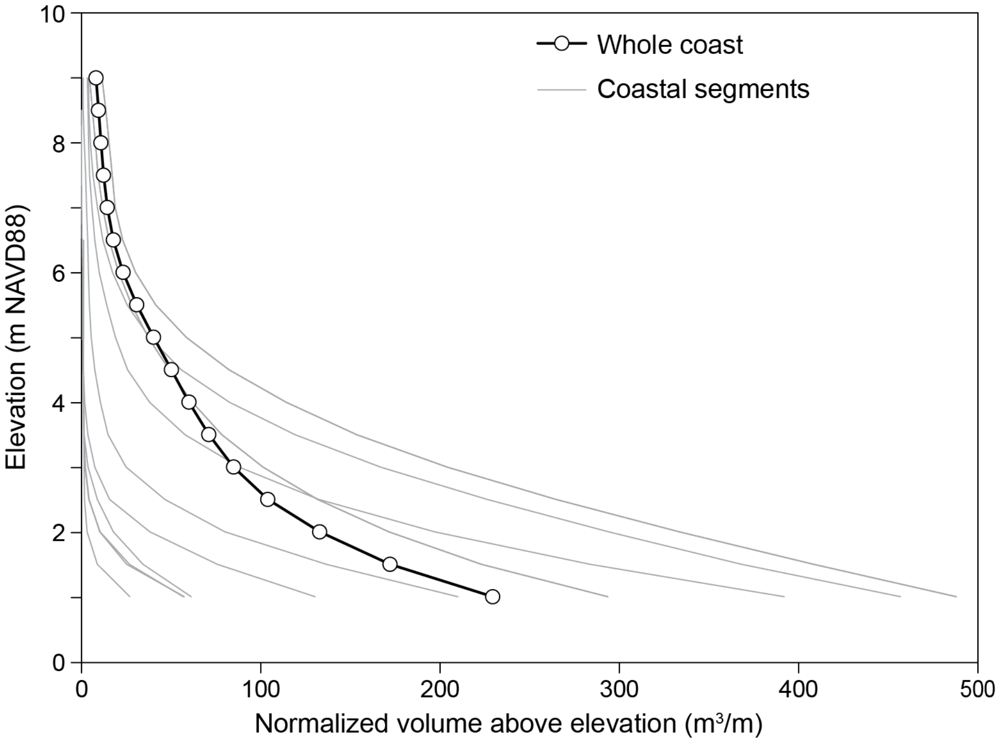

Figure 31. Normalized beach and foredune volume above 1 to 9 m elevation for the Texas Gulf shoreline and for major coastal segments.

Table 7. Estimated total volume (m^3) in the beach and foredune system above threshold elevations between 1 and 9 m NAVD88. Volumes are estimated from the DEM of the beach and dune system created from 2019 airborne lidar survey data (excluding structures and the area landward of the 2019 landward beach or dune boundary). Total volumes are calculated by adding volumes calculated for 50-m-wide corridors centered on transects (sites) across the beach and foredune system that coincide with those used to calculate shoreline movement rates.

	Sites	**>1 m**	**>2 m**	**>3 m**	**>4 m**	**>5 m**	**>6 m**	**>7 m**	**>8 m**	**>9 m**
All Texas sites	11,571	132,864,949	73,647,777	39,536,831	20,561,625	10,136,528	4,767,698	2,192,104	989,773	426,415
Geomorphic Areas										
Sabine Pass to Rollover Pass	1,314	1,712,781	96,071	6,325	613	16				
Bolivar Peninsula	536	1,617,792	450,493	62,809	1,679	55				
Galveston Island (all)	879	2,483,534	402,617	41,886	1,682	17				
Galv. Is. (East Beach)	113	563,641	89,223	13,371	693	5				
Galv. Is. (seawall)	183	211,770	23,440	506	21					
Galv. Is. (West Beach)	583	1,708,123	289,954	28,009	968	12				
Brazos–Colorado headland	1,213	3,407,747	554,174	40,464	2,115	346	121			
Matagorda Peninsula	1,579	10,309,173	3,020,302	475,384	70,075	8,993	1,319	159	10	
Matagorda Island	1,116	11,731,296	4,454,048	1,222,387	310,762	83,313	25,593	8,058	2,310	530
San José Island	622	12,201,877	5,995,310	2,610,611	1,092,120	454,749	185,124	69,903	22,956	6,654
Mustang Island	557	12,736,616	8,191,779	4,640,893	2,280,488	1,004,439	399,325	146,001	52,247	21,613
N. Padre Island	2,402	58,666,868	40,095,520	24,512,495	13,540,256	6,884,156	3,326,833	1,588,055	750,613	335,895
S. Padre Island	1,120	16,459,533	9,611,208	5,595,688	3,148,242	1,666,381	820,002	378,079	161,509	61,722
Brazos Island	233	1,537,733	776,256	327,889	113,593	34,062	9,381	1,850	129	

Volumetrics on the Upper Texas Coast (Sabine Pass to San Luis Pass)

Beach and foredune elevations along most of the upper Texas coast between Sabine Pass and San Luis Pass are among the lowest on the Texas Gulf shoreline (fig. 28). Low peak elevations occur along the Sabine chenier west of Sabine Pass, the Trinity headland marshes southwest of Sea Rim State Park, and the low marshes northeast of Rollover Pass. Areas of slightly higher peak elevations include segments near Sea Rim State Park, along Bolivar Peninsula, and Galveston Island east and west of the seawall (fig. 32).

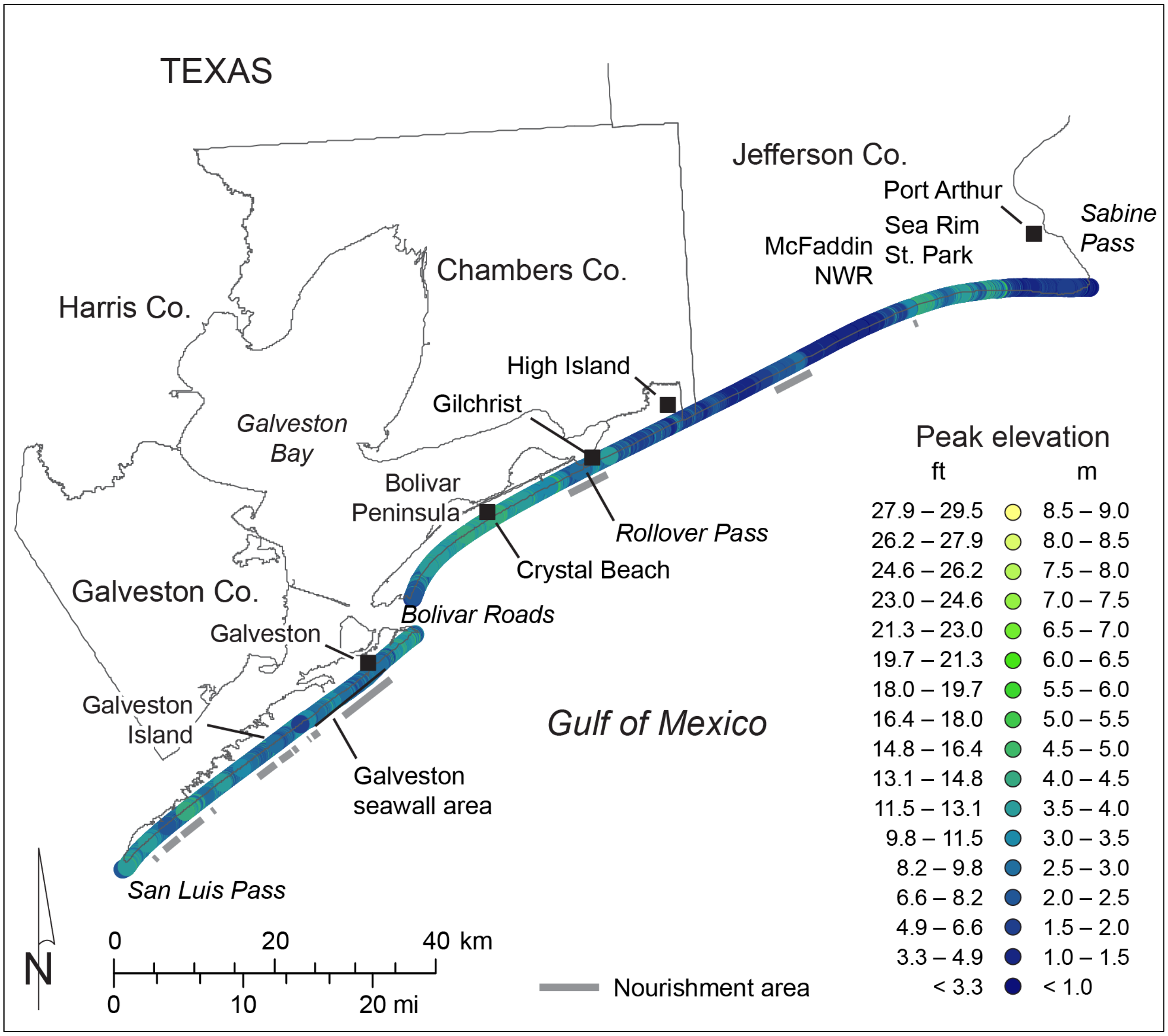

Figure 32. Peak beach and foredune elevation along the upper Texas coast determined at 50-m intervals from the 2019 airborne lidar survey. Nourishment and restoration areas are listed in Appendix B.

Percentages of shoreline above most threshold elevations along this part of the coast are among the lowest of all Texas coastal segments and are well below the average at all higher elevations (fig. 33). Peak elevations are above 3 m (10 ft) along less than 25 percent of the shoreline between Sabine Pass and Rollover Pass (fig. 33a). Peak elevations are above 4 m (13 ft) along more than 50 percent of the shoreline on Bolivar Peninsula (fig. 33b) and are above 3.5 m (11.5 ft) along more than 50 percent of Galveston Island (fig. 33c).

Normalized alongshore volumes above 1 m (3 ft) elevation are also very low on the upper Texas coast (fig. 34). Lowest values are along the Sabine chenier, the segment on the Trinity headland from Rollover Pass to Sea Rim State Park, and on Galveston Island in front of the seawall and adjacent to the western end of the seawall. Slightly higher values occur along Sea Rim State Park, most of Bolivar Peninsula, at the eastern end of Galveston Island, and along the western half of Galveston Island.

Total and normalized volumes are well below the whole-coast averages for all threshold elevations (table 7 and fig. 35). Normalized volumes decrease to near 0 m^3/m above 2 m (7 ft) elevation between Sabine Pass and Rollover Pass (fig. 35a), above 3.5 m (11.5 ft) elevation on Bolivar Peninsula (fig. 35b), and above 3 m (10 ft) elevation on Galveston Island.

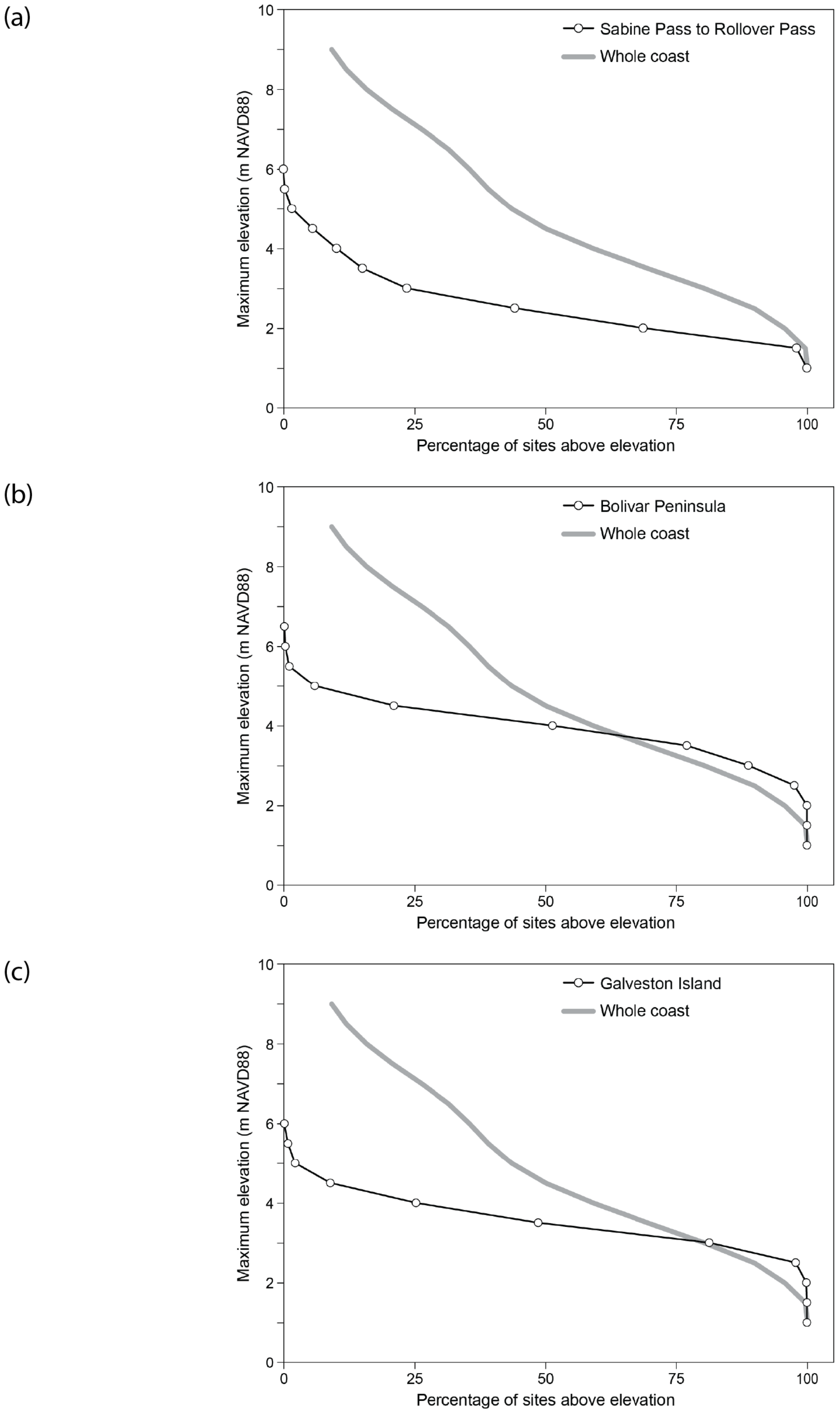

Figure 33. Percentage of the upper Texas coast shoreline having peak beach and foredune elevations above threshold elevations ranging from 1 to 9 m along (a) between Sabine Pass and Rollover Pass and along (b) Bolivar Peninsula and (c) Galveston Island.

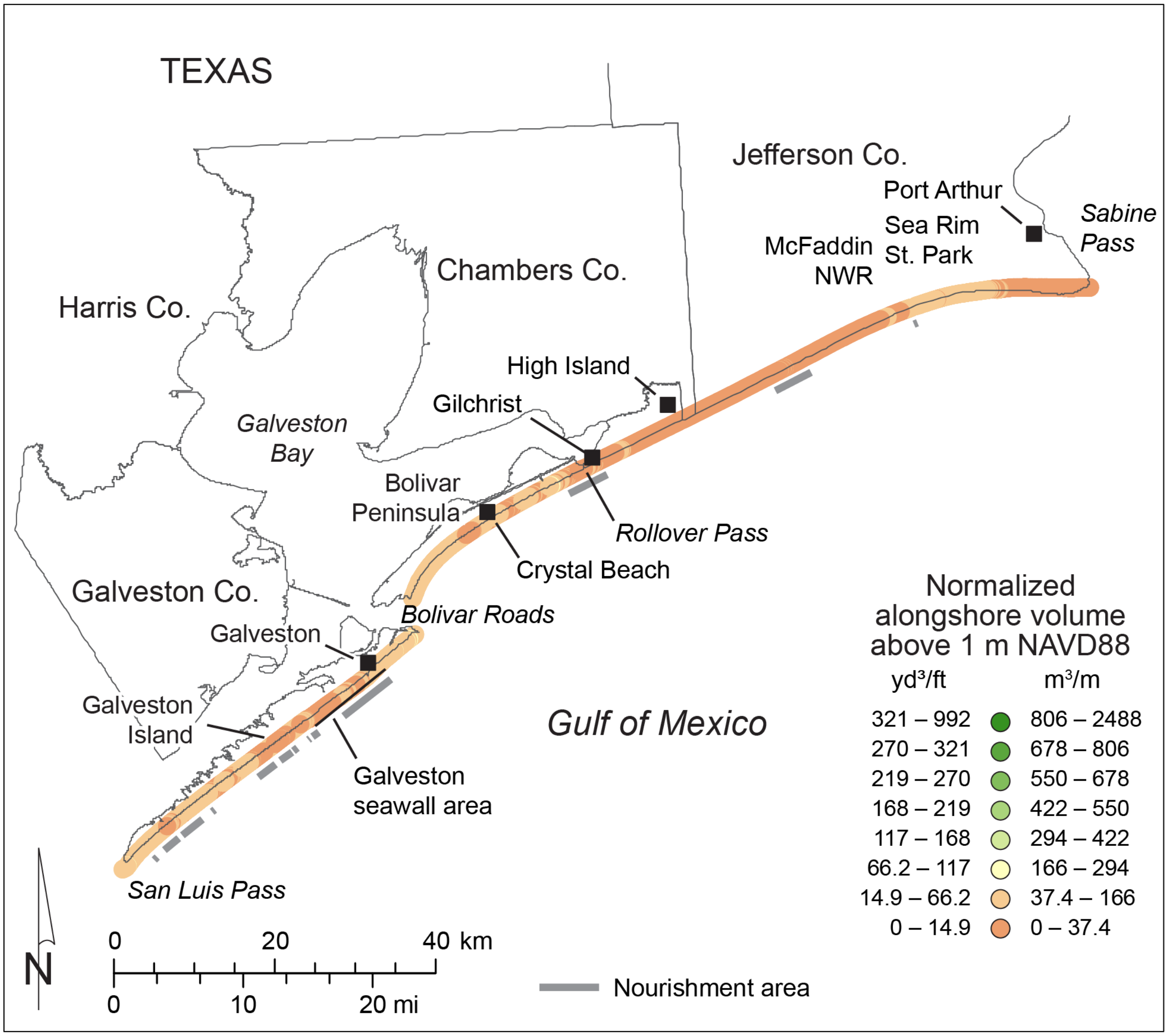

Figure 34. Normalized beach and foredune volume above 1 m elevation along the upper Texas coast. Nourishment and restoration areas are listed in Appendix B.

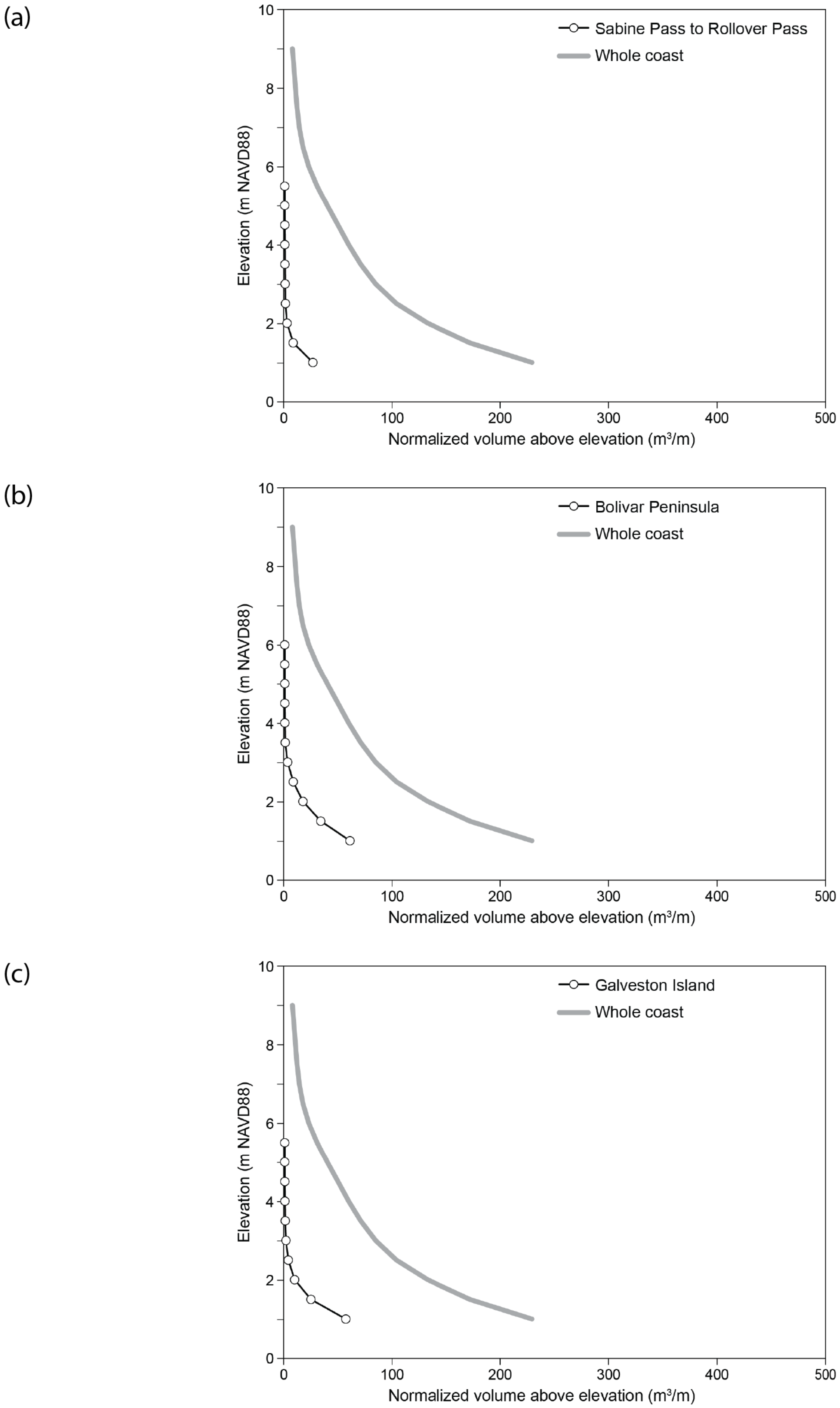

Figure 35. Normalized beach and foredune volume above 1 to 9 m elevation on the upper Texas coast (a) between Sabine Pass and Rollover Pass and along (b) Bolivar Peninsula and (c) Galveston Island.

Volumetrics along the Brazos–Colorado Headland and Adjacent Peninsulas

Beach and foredune peak elevations and volumes are relatively low along the Texas Gulf shoreline between San Luis Pass and Pass Cavallo, an upper-middle coastal segment that includes the Brazos–Colorado headland and the flanking barrier peninsulas Follets Island and Matagorda Peninsula (figs. 28 and 30). Peak beach and foredune elevations are lowest near the mouth of the Brazos River and on the western part of the headland near Sargent Beach (fig. 36). The highest peak elevations occur on Matagorda Peninsula to the northeast and southwest of

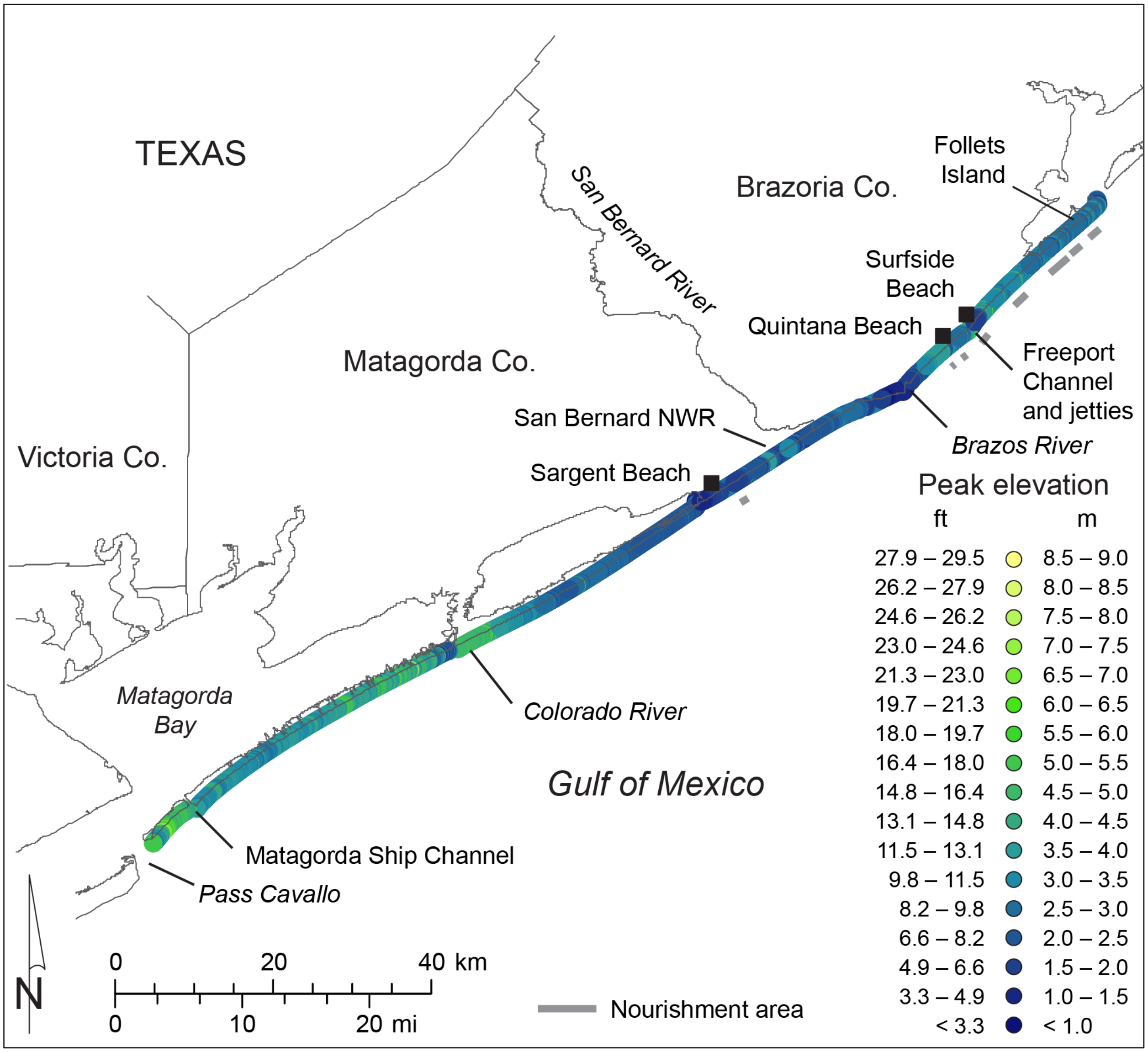

Figure 36. Peak beach and foredune elevation between San Luis Pass and Pass Cavallo determined at 50-m intervals from the 2019 airborne lidar survey. Nourishment and restoration areas are listed in Appendix B.

the mouth of the Colorado River and between the Matagorda Ship Channel and Pass Cavallo. Just more than half of the beach and foredune system along the Brazos–Colorado headland has peak elevations above 3 m (10 ft) (fig. 37a). Peak elevations are generally higher on Matagorda Peninsula, where just less than 50 percent of the shoreline has beach and foredune elevations above 4 m (13 ft) (fig. 37b).

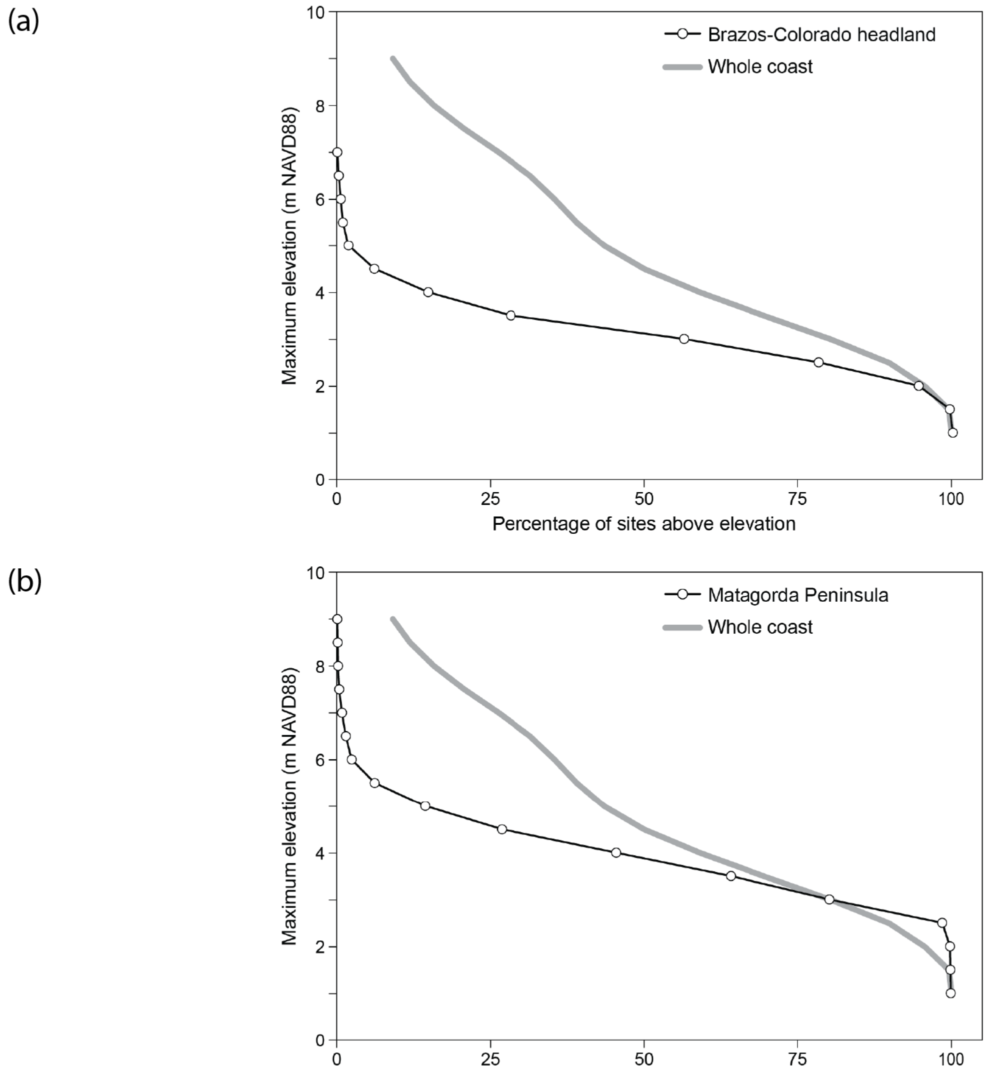

Figure 37. Percentage of the shoreline between San Luis Pass and Pass Cavallo having peak beach and foredune elevations above threshold elevations ranging from 1 to 9 m along (a) the Brazos–Colorado headland and Follets Island and (b) Matagorda Peninsula.

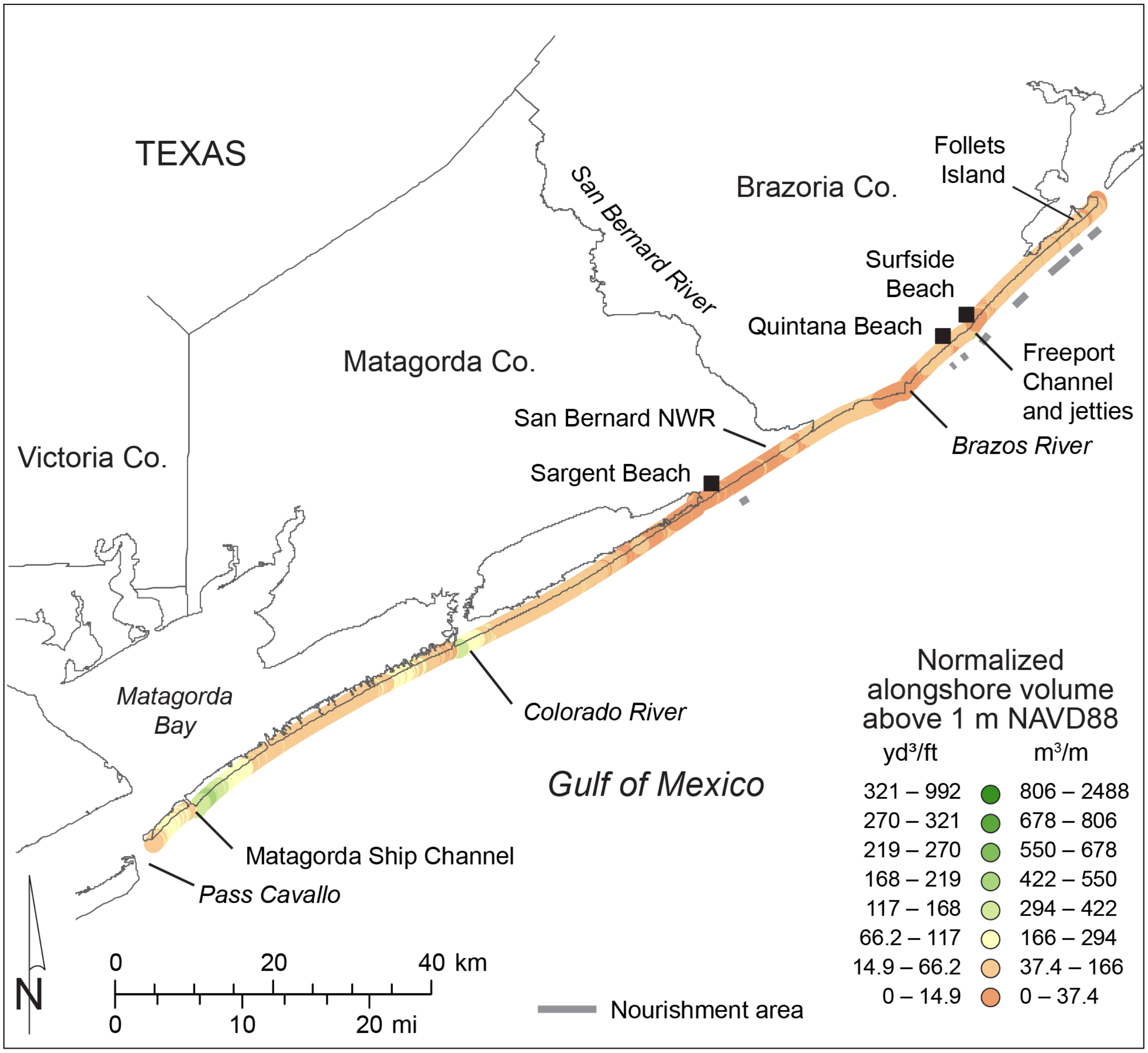

Figure 38. Normalized beach and foredune volume above 1 m elevation between San Luis Pass and Pass Cavallo. Nourishment and restoration areas are listed in Appendix B.

Normalized alongshore volumes above 1 m (3 ft) elevation are also low along most of this coastal segment (fig. 38). Areas of low normalized volumes above 1 m (3 ft) elevation include Surfside Beach near the Freeport Channel and jetties, the mouth of the Brazos River, and the western flank of the Brazos–Colorado headland near Sargent Beach. Segments on Matagorda Peninsula near the mouth of the Colorado River and northeast of the Matagorda Ship Channel have the highest normalized volumes greater than 1 m (3 ft) elevation (fig. 38).

Normalized sediment volumes are lower than whole-coast averages at all threshold elevations (table 7 and fig. 39). Normalized volumes are near 0 m³/m above threshold elevations of 3 m (10 ft) on the Brazos–Colorado headland (fig. 39a) and 4 m (13 ft) on Matagorda Peninsula.

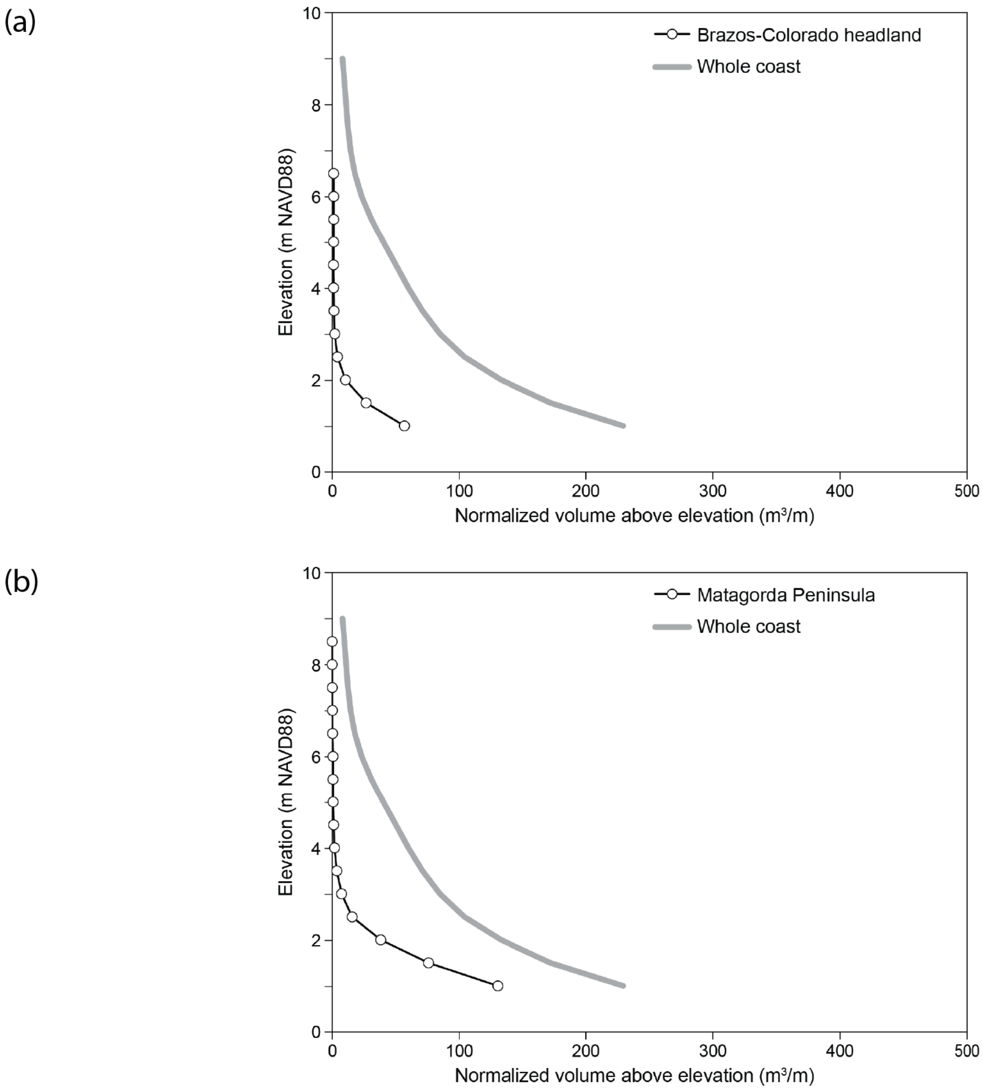

Figure 39. Normalized beach and foredune volume above 1 to 9 m elevation along (a) the Brazos–Colorado headland and Follets Island and (b) Matagorda Peninsula.

Volumetrics on the Middle Texas Coast (Pass Cavallo to Packery Channel)

Peak elevations and beach and foredune volumes generally increase southward along the middle Texas coast, where relatively stable shorelines front three sand-rich barrier islands (Matagorda Island, San José Island, and Mustang Island, figs. 28 and 30). Low to moderate peak beach and foredune elevations at the eastern end of Matagorda Island gradually increase southwestward toward Cedar Bayou, remaining relatively high along most of San José Island and nearly all of Mustang Island (fig. 40). Peak elevations are above 4 m (13 ft) along about 50 percent of

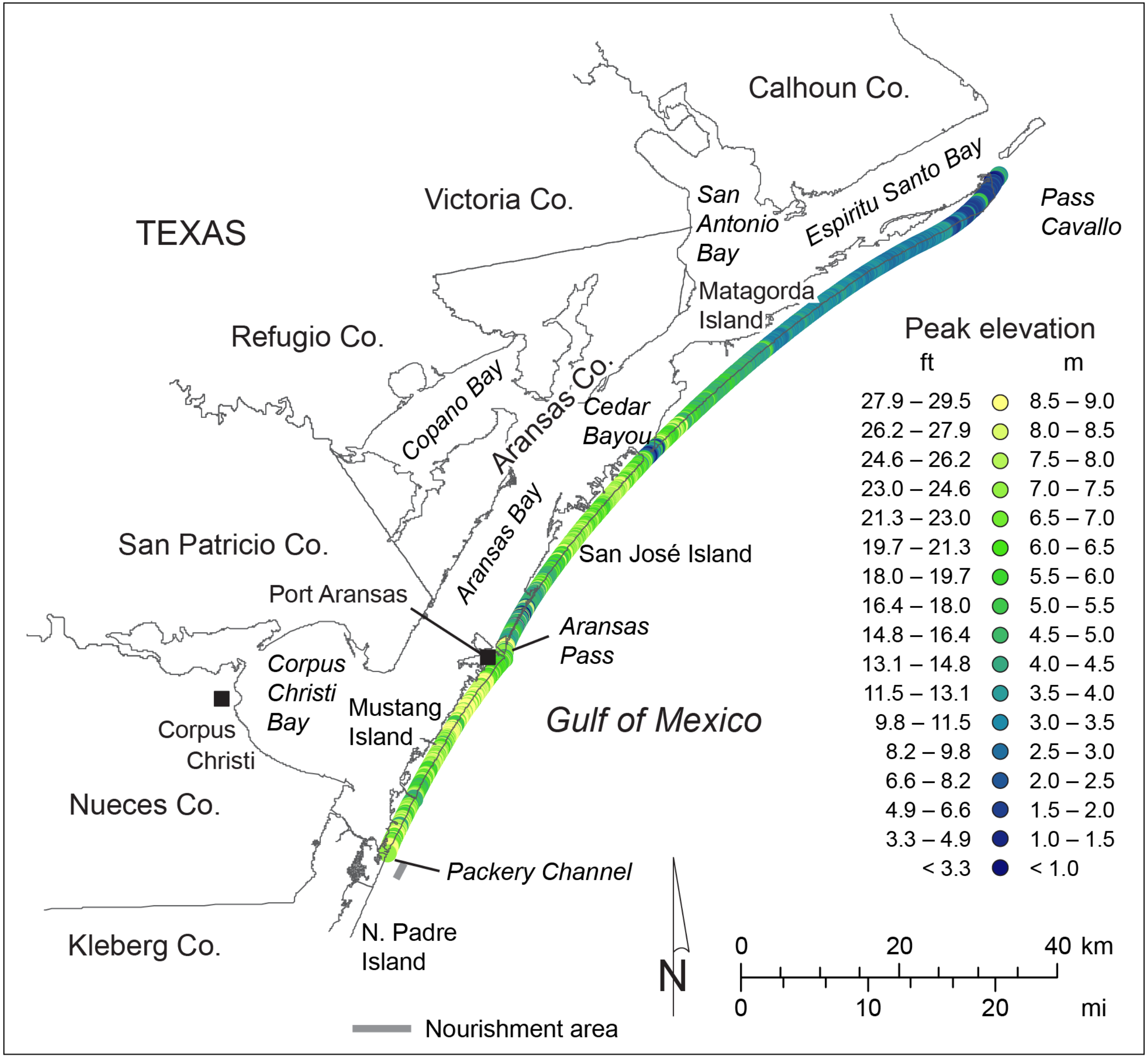

Figure 40. Peak beach and foredune elevation along the middle Texas coast determined at 50-m intervals from the 2019 airborne lidar survey. Nourishment and restoration areas are listed in Appendix B.

Matagorda Island (fig. 41a). Peak elevations exceed 7 m (23 ft) along 50 percent of the San José Island shoreline (fig. 41b) and 7.5 m (24.6 ft) along 50 percent of the Mustang Island shoreline (fig. 41c), much higher than the whole-coast average.

Normalized volumes above 1 m (3 ft) elevation follow a similar trend: relatively low beach and foredune volumes at the eastern end of Matagorda Island increase to much higher values from the western part of Matagorda Island to the southern end of Mustang Island (fig. 42). Relatively low normalized volumes occur near Cedar Bayou and along the southern end of San José Island.

As threshold elevations increase, normalized volumes above those elevations transition from below whole-coast averages at all elevations along Matagorda Island (fig. 43a), to higher than whole-coast averages at elevations below 3 m (10 ft) and lower than whole-coast averages above 3 m (10 ft) along San José Island (fig. 43b), to mostly higher than or equal to whole-coast averages at all elevations along Mustang Island (fig. 43c). Total and normalized volumes remain above 0 at 9 m (30 ft) elevation (table 7 and fig. 43) for all three barrier islands on the middle Texas coast, although volumes above 6 m (20 ft) are relatively insignificant on Matagorda Island.

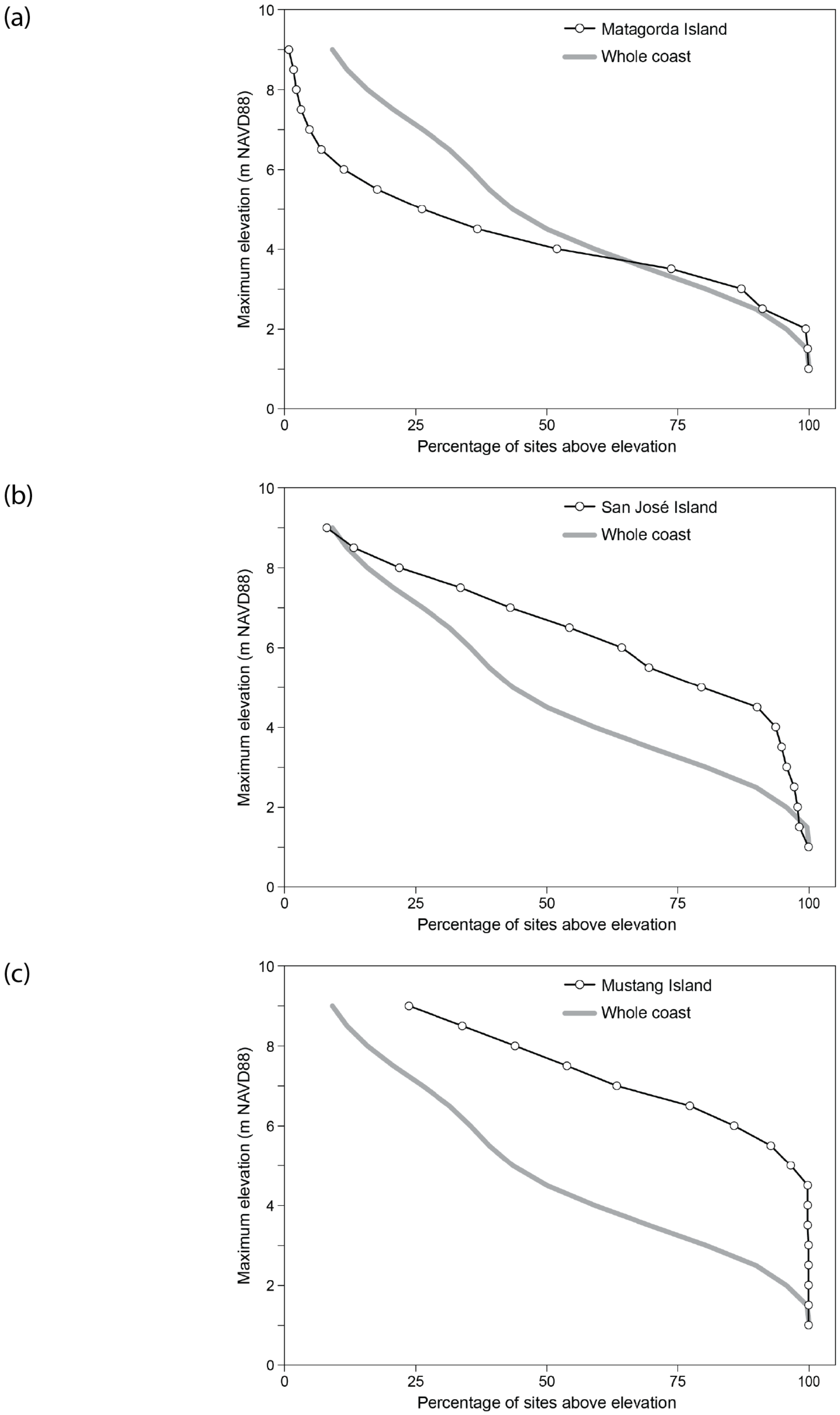

Figure 41. Percentage of the middle Texas coast shoreline having peak beach and foredune elevations above threshold elevations ranging from 1 to 9 m along (a) Matagorda Island, (b) San José Island, and (c) Mustang Island.

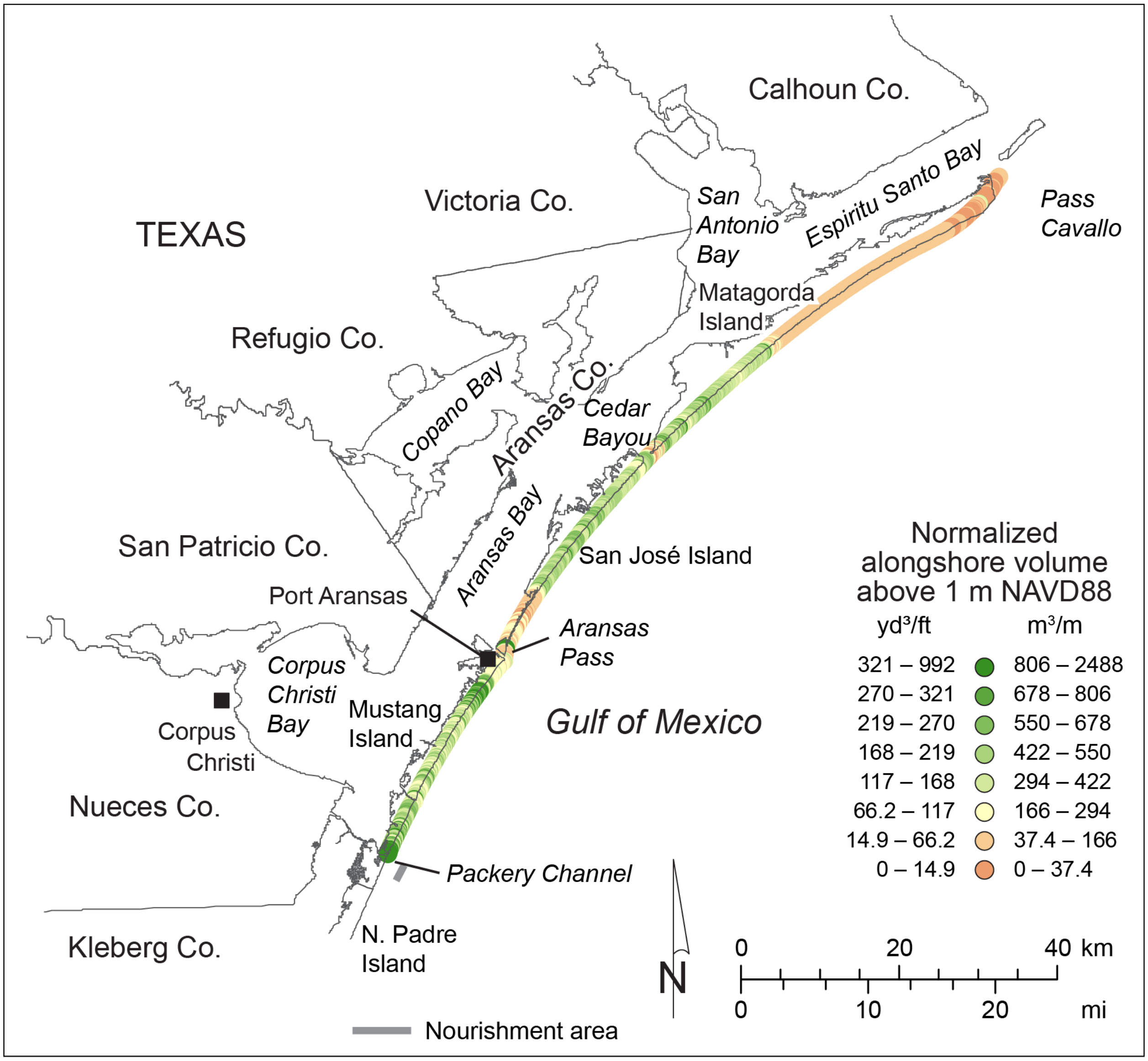

Figure 42. Normalized beach and foredune volume above 1 m elevation along the middle Texas coast. Nourishment and restoration areas are listed in Appendix B.

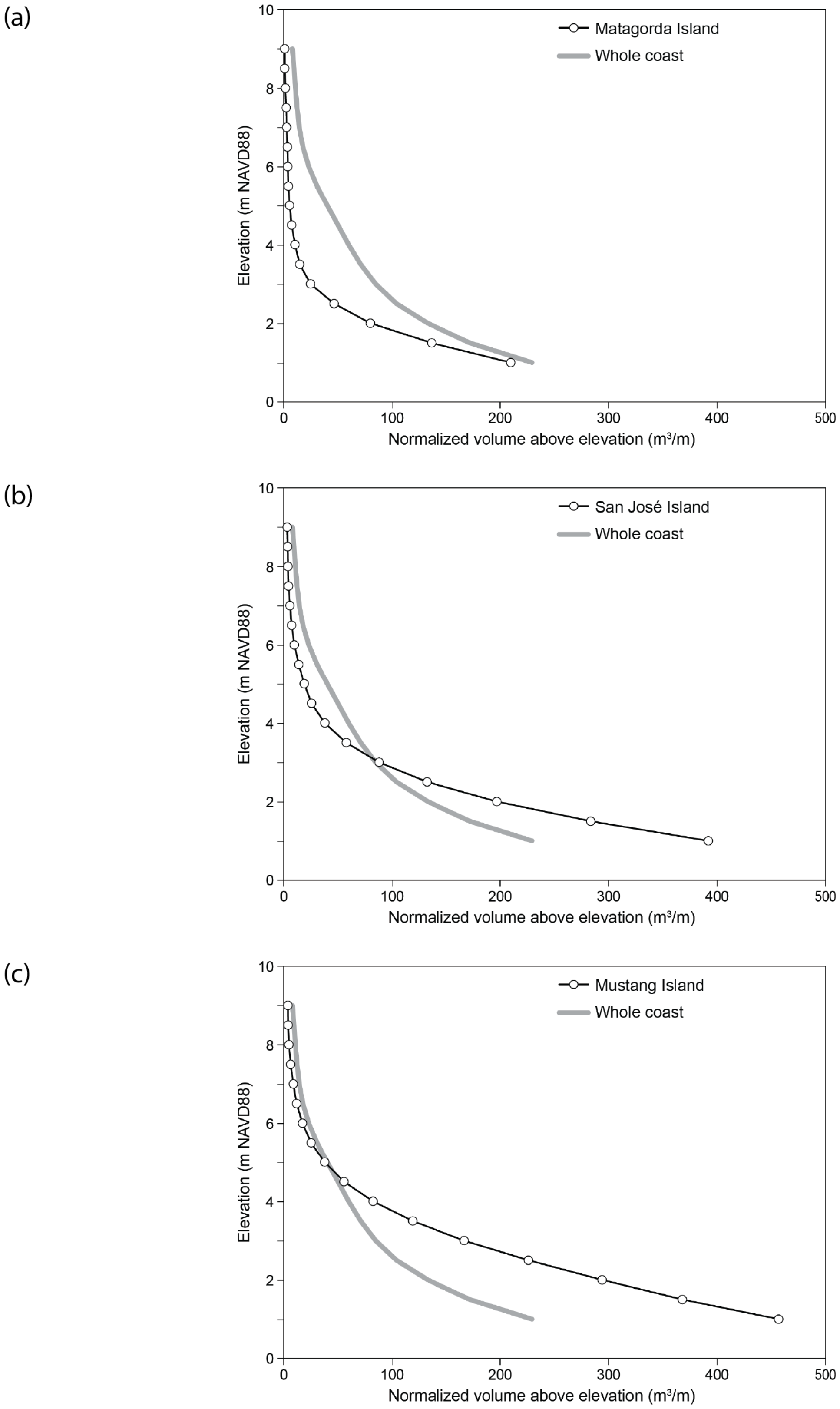

Figure 43. Normalized beach and foredune volume above 1 to 9 m elevation on the middle Texas coast along (a) Matagorda Island, (b) San José Island, and (c) Mustang Island.

Volumetrics on the Lower Coast (Padre Island and Brazos Island)

The lower coast includes all of Padre Island (Packery Channel to Brazos Santiago Pass) and Brazos Island, a barrier peninsula on the northern flank of the Rio Grande headland. Mansfield Channel separates northern and southern Padre Island. Beach and foredune elevations and volumes are very high along most of northern Padre Island, but generally decrease southward to southern Padre Island and Brazos Island (figs. 28 and 30). Beaches and foredunes at the northern tip of Padre Island and near the southern end of the island have the lowest peak elevations (fig. 44). Peak elevations above 9 m (30 ft) are common along nearly the entire length of Padre Island, particularly along the northern half. Shoreline percentages are above whole-coast average percentages at every threshold elevation along northern Padre Island (fig. 45a) and are equal to, or higher than, whole-coast averages at every threshold elevation on southern Padre Island (fig. 45b). On Brazos Island, shoreline percentages with beach and foredune threshold elevations of 5.5 m (18 ft) or lower are above whole-coast averages.

Normalized alongshore volumes above 1 m (3 ft) elevation are very high for shorelines along the northern half of Padre Island, but decrease near Mansfield Channel, near the southern end of Padre Island, and on Brazos Island (fig. 46).

Total sediment volume above 1 m (3 ft) elevation is about 59,000,000 m^3 (77,000,000 yd^3) on northern Padre Island, which is just less than half the total volume above 1 m (3 ft) elevation for the entire Texas beach and foredune system (table 7). When combined with the southern Padre Island volumes, the total is more than half that for the entire coast. Normalized volumes for northern and southern Padre Island are generally higher than the whole-coast averages at all threshold elevations (fig. 47a,b). Normalized volumes on Brazos Island are lower than the whole-coast average at threshold elevations below 4 m (13 ft) (fig. 47c).

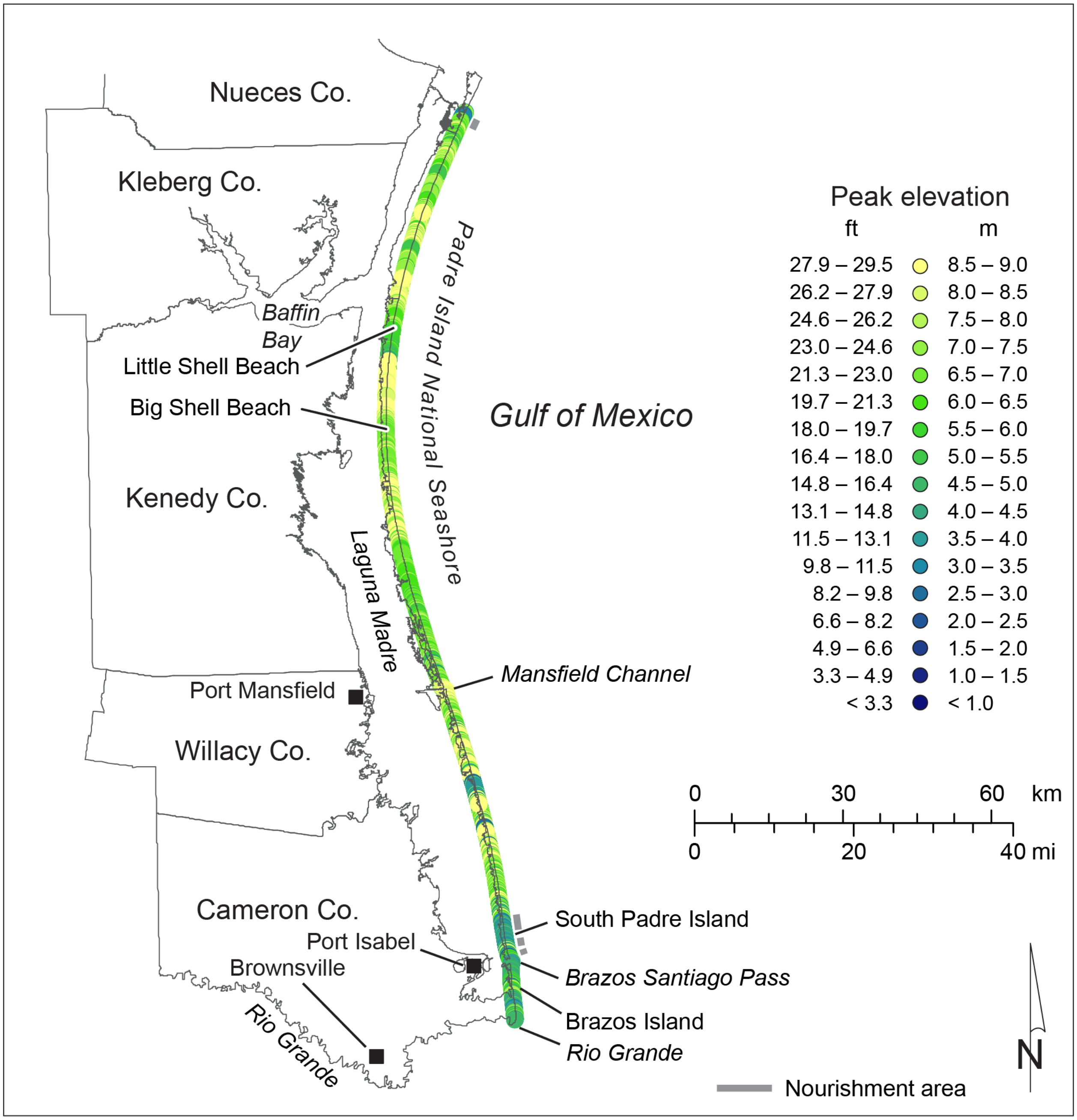

Figure 44. Peak beach and foredune elevation along the lower Texas coast determined at 50-m intervals from the 2019 airborne lidar survey. Nourishment and restoration areas are listed in Appendix B.

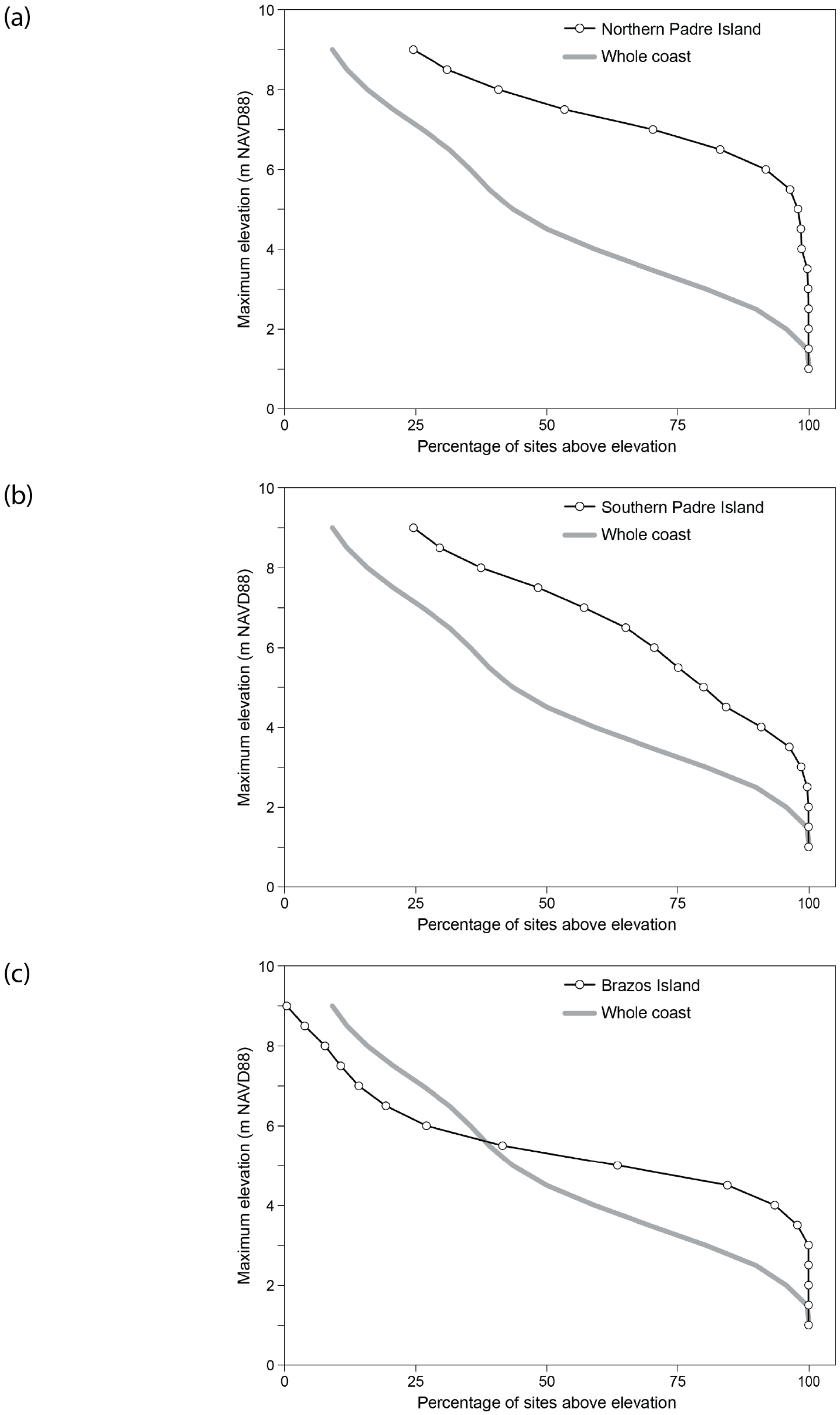

Figure 45. Percentage of the lower Texas coast shoreline having peak beach and foredune elevations above threshold elevations ranging from 1 to 9 m along (a) northern Padre Island, (b) southern Padre Island, and (c) Brazos Island.

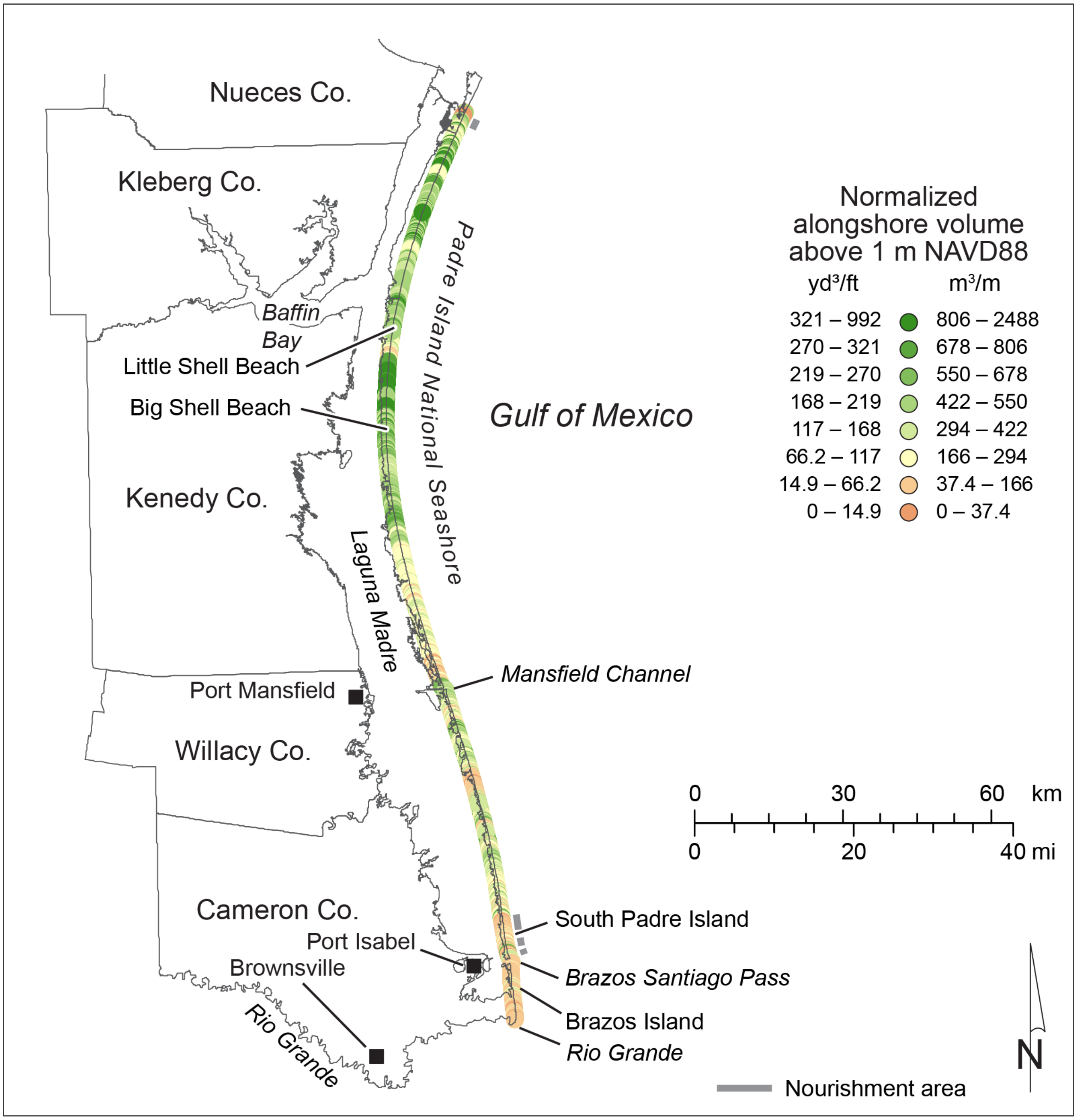

Figure 46. Normalized beach and foredune volume above 1 m elevation on the lower Texas coast. Nourishment and restoration areas are listed in Appendix B.

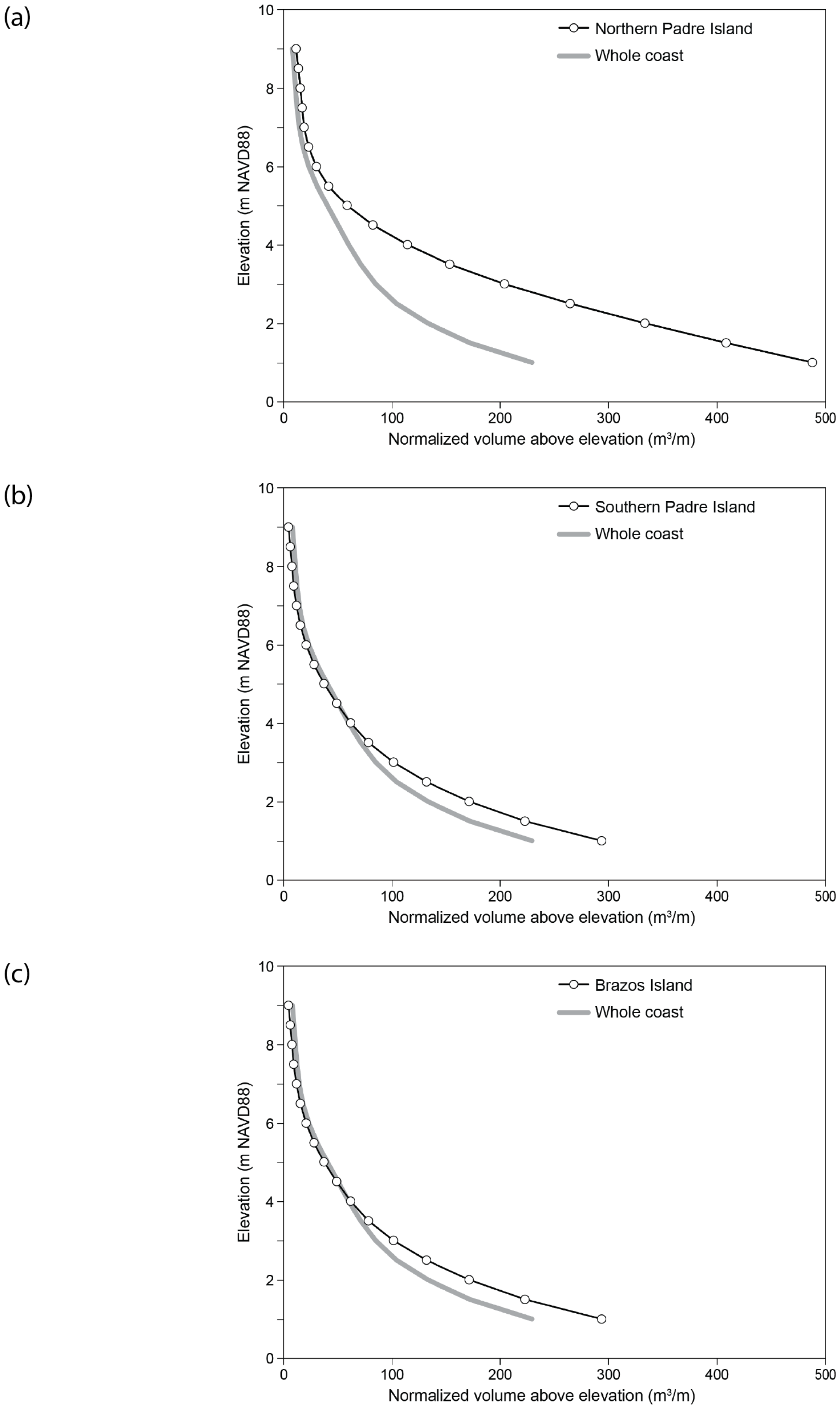

Figure 47. Normalized beach and foredune volume above 1 to 9 m elevation on the lower Texas coast along (a) northern Padre Island, (b) southern Padre Island, and (c) Brazos Island.

CONCLUSIONS

Long-term rates of Texas Gulf shoreline change have been updated through 2019 from a series of shoreline positions that includes those from aerial photography from the 1930s through 2007, ground GPS surveys from the mid-1990s, and airborne lidar surveys conducted in 2000, 2012, and 2019.

Over the 19 storm seasons (2000 to 2018) coinciding with the most recent short-term shoreline monitoring period considered in this report, there were ten tropical storms and six hurricanes that made landfall on the Texas coast, including seven on the upper coast, four on the middle coast, and five on the lower coast. Tropical cyclone frequency was 0.8 per year, which nearly equals the historical frequency. Relative sea-level rise rates at Galveston Pier 21 since 2000, coinciding with the most recent monitoring period, are at the high end of historically observed rates (about 12 mm/yr).

Change rates calculated at 11,722 sites spaced at 50-m intervals averaged net retreat at 1.27 m/yr (4.2 ft/yr) through 2019. Average change rates were more recessional on the upper Texas coast (retreat at 1.71 m/yr [5.6 ft/yr]) than they were on the middle and lower coast (retreat at 0.97 m/yr [3.2 ft/yr]). Annual rates of land loss along the Texas Gulf shoreline average 74 ha/yr (184 ac/yr). Total land loss since 1930, when aerial photography-based shoreline monitoring became possible, is estimated to be 6,627 ha (16,375 ac). For the most recent short-term monitoring period (2000 to 2019), the average net shoreline movement rate is retreat at 1.25 m/yr (4.1 ft/yr), which is similar to the average historical net rate.

Historical shoreline retreat rates calculated from shoreline positions determined from aerial photographs and ground and airborne surveys, when compared to prehistoric rates estimated from bathymetric contour shoreline proxies and past sea-level positions, are significantly lower than late Pleistocene to early-Holocene retreat rates of 2.5 to 55.2 m/yr (8 to 181 ft/yr) but are similar to retreat rates of 0.1 to 1.7 m/yr (0.4 to 5.4 ft/yr) estimated since the mid-Holocene.

Postglacial rates of retreat per millimeter per year of relative sea-level rise range from 0.8 m/yr for the lower coast to 1.8 m/yr for the upper coast. This relationship can be used to estimate future rates of Gulf shoreline retreat under various relative sea-level rise scenarios.

Elevation and volumetric trends in the beach and foredune corridor determined from the 2019 airborne lidar survey generally follow shoreline movement trends. Rapidly retreating shoreline segments have lower peak beach and foredune elevations than do segments where shorelines are more stable or advancing. Peak beach and foredune elevations are below 4.5 m (15 ft) elevation along nearly 50 percent of the Texas Gulf shoreline. Areas of low peak beach and foredune elevations and low sediment volumes above 1 m (3.3 ft) elevation include the Sabine chenier and Trinity headland on the upper Texas coast, the Brazos–Colorado headland, and parts of Matagorda Peninsula and Matagorda Island. Total sediment volume above 1 m (3.3 ft) elevation in the beach and foredune system is estimated to be nearly 133,000,000 m^3 (174,000,000 yd^3), of which more than half is stored in the beach and foredune system on Padre Island.

ACKNOWLEDGMENTS

This project was supported by Contract No.16-201-000, Work Order No. B428 from the General Land Office of Texas (GLO) to the Bureau of Economic Geology, The University of Texas at Austin. Jeffrey G. Paine served as the principal investigator. The project was funded through the Coastal Erosion Planning and Response Act (CEPRA) program (Project No. 1662) administered by the GLO. Kelly Brooks (GLO) served as project manager. Bureau researchers John Andrews and Aaron Averett acquired the 2019 airborne lidar survey data. TxDOT pilots Travis Zachary, Carol Foy, Jim Reid, Alan Fenter, and Brian Schoen flew the aircraft. Bureau researchers Tiffany Caudle, John Andrews, and Kutalmis Saylam processed the lidar data and imagery. Kelly Brooks (GLO) provided information on beach nourishment and dune restoration projects.

REFERENCES

Anders, F. J., and Byrnes, M. R., 1991, Accuracy of shoreline change rates as determined from maps and aerial photographs: Shore and Beach, v. 59, p. 17–26.

Aronow, S., Fisher, W. L., McGowen, J. H., and Barnes, V. E., 1982, Geologic Atlas of Texas, Houston Sheet: The University of Texas at Austin, Bureau of Economic Geology, scale 1:250,000, 1 sheet.

Balsillie, J. H., and Donoghue, J. F., 2009, Chapter 4: Northern Gulf of Mexico sea-level history for the past 20,000 years: in Holmes, C.W., ed., The Gulf of Mexico, Its Origin, Waters, Biota and Human Impacts: Vol. 1, Geology: Corpus Christi, TX, Harte Research Institute for Gulf of Mexico Studies, p. 53–69.

Balsillie, J. H., and Donoghue, J. F., 2004, High resolution sea-level history for the Gulf of Mexico since the last glacial maximum: Florida Geological Survey, Report of Investigations No. 103, 65 p.

Barnett, T. P., 1983, Global sea level: estimating and explaining apparent changes: in Magoon, O. T., and Converse, H., eds., Coastal Zone ‘83, Proceedings of the Third Symposium on Coastal and Ocean Management, v. 3, p. 2777–2783.

Blake, E. S., and Zelinsky, D. A., 2018, Hurricane Harvey (AL092017): National Hurricane Center Tropical Cyclone Report, 77 p.

Brown, L. F., Jr., Brewton, J. L., and McGowen, J. H., 1975, Geologic Atlas of Texas, Corpus Christi Sheet: The University of Texas at Austin, Bureau of Economic Geology, scale 1:250,000, 1 sheet.

Brown, L. F., Jr., Brewton, J. L., McGowen, J. H., Proctor, C. V., Aronow, S., and Barnes, V.E., 1975, Geologic Atlas of Texas, Beeville-Bay City Sheet: The University of Texas at Austin, Bureau of Economic Geology, scale 1:250,000, 1 sheet.

Brown, L. F., Jr., Brewton, J. L., White, W. A., and Owens, F., 1976, Geologic Atlas of Texas, McAllen-Brownsville Sheet: The University of Texas at Austin, Bureau of Economic Geology, scale 1:250,000, 1 sheet.

Bruun, P., 1954, Coastal erosion and development of beach profiles: Technical Memorandum, v. 44, Beach Erosion Board, U. S. Army Corps of Engineers, 82 p.

Bruun, P., 1962, Sea-level rise as a cause of shore erosion: Proceedings, American Society of Civil Engineers, Journal of the Waterways and Harbors Division, v. 88, p. 117–130.

Bruun, P., 1988, The Bruun rule of erosion by sea-level rise: a discussion of large-scale two- and three-dimensional usages: Journal of Coastal Research, v. 4, p. 627–648.

Caudle, T., and Paine, J. G., 2012, Pre-college student involvement in Texas coastal research: Gulf Coast Association of Geological Societies Transactions, v. 62, p. 27–38.

Caudle, T., and Paine, J. G., 2017, Applications of coastal data collected in the Texas High School Coastal Monitoring Program (THSCMP): Journal of Coastal Research, v. 33, no. 3, p. 738–746. DOI: 10.2112/JCOASTRES-D-16-00033.1.

Cazenave, A., and Nerem, R. S., 2004, Present-day sea level change: observations and causes: Reviews of Geophysics, v. 42, RG3001. doi: 1029/2003RG000139, 20 p.

Cazenave, A., Dieng, H.-B., Meyssignac, B., von Schuckmann, K., Decharme, B., and Berthier, E., 2014, The rate of sea-level rise: Nature Climate Change, v. 4, p. 358-361.

Church, J. A., Clark, P. U., Cazenave, A., Gregory, J. M., Jevrejeva, S., Levermann, A., Merrifield, M. A., Milne, G. A., Nerem, R. S., Nunn, P. D., Payne, A. J., Pfeffer, W. T., Stammer, D., and Unnikrishnan, A. S., 2013, Sea Level Change: in Stocker, T. F., Qin, D., Plattner, G.-K., Tignor, M., Allen, S. K., Boschung, J., Nauels, A., Xia, Y., Bex, V., and Midgley, P.M., eds., Climate Change 2013: The Physical Science Basis: Contribution of Working Group I to the Fifth Assessment Report of the Intergovernmental Panel on Climate Change. Cambridge, United Kingdom and New York, NY, USA: Cambridge University Press, 1137–1216.

Church, J. A., and White, N. J., 2006, A 20th century acceleration in global sea-level rise: Geophysical Research Letters, v. 33: L01602. doi: 10.1029/2005GL024826.

Church, J. A., and White, N. J., 2011, Sea-level rise from the late 19th to the early 21st century: Surveys in Geophysics, v. 32, p. 585-602. doi: 10.1007/s10712-011-9119-1.

Cooper, J. A. G., and Pilkey, O. H., 2004, Sea-level rise and shoreline retreat: time to abandon the Bruun Rule: Global and Planetary Change, v. 43, p. 157–171.

Crowell, M., Leatherman, S. P., and Buckley, M. K., 1991, Historical shoreline change: error analysis and mapping accuracy: Journal of Coastal Research, v. 7, no. 3, p. 839–852.

Emery, K. O., 1980, Relative sea levels from tide-gauge records: Proceedings, National Academy of Sciences, USA, v. 77: p. 6968–6972.

FitzGerald, D. M., Fenster, M. S., Argow, B. A., and Buynevich, I. V., 2008, Coastal impacts due to sea-level rise: Annual Review of Earth and Planetary Sciences, v. 36, p. 601–647.

Gibeaut, J. C., and Caudle, T., 2009, Defining and mapping foredunes, the line of vegetation, and shorelines along the Texas Gulf Coast: Texas A&M University Corpus Christi, Harte Research Institute and The University of Texas at Austin, Bureau of Economic Geology, final report prepared for the Texas General Land Office contract no. 07-005-22 and National Oceanic and Atmospheric Administration award no. NA06NOS4190219, 14 p.

Gibeaut, J. C., Gutierrez, R., and Hepner, T., 2002, Threshold conditions for episodic beach erosion along the southeast Texas coast: Gulf Coast Association of Geological Societies Transactions, v. 52, p. 323–335.

Gibeaut, J. C., Hepner, T., Waldinger, R., Andrews, J., Gutierrez, R., Tremblay, T. A., and Smyth, R., 2001, Changes in Gulf shoreline position, Mustang and North Padre Islands, Texas: The University of Texas at Austin, Bureau of Economic Geology, Report to the Texas Coastal Coordination Council and the General Land Office, contract no. 00-002r, 29 p.

Gibeaut, J. C., White, W. A., Hepner, T., Gutierrez, R., Tremblay, T. A., Smyth, R. A., and Andrews, J., 2000, Texas Shoreline Change Project: Gulf of Mexico shoreline change from the Brazos River to Pass Cavallo: The University of Texas at Austin, Bureau of Economic

Geology, Report to the Texas Coastal Coordination Council and the General Land Office, contract no. NA870Z0251, 32 p.

Gornitz, V., Lebedeff, S., and Hansen, J., 1982, Global sea level trend in the past century: Science, v. 215, p. 1611–1614.

Gornitz, V., and Lebedeff, S., 1987, Global sea-level changes during the past century: in Nummedal, D., Pilkey, O. H., and Howard, J. D., eds., Sea level fluctuation and coastal evolution: Society of Economic Paleontologists and Mineralogists Special Publication 41, p. 3–16.

Gutenberg, B., 1941, Changes in sea level, postglacial uplift, and mobility of the Earth's interior: Geological Society of America Bulletin, v. 52, p. 721–772.

Hayes, M. O., 1967, Hurricanes as geological agents: case studies of hurricanes Carla, 1961, and Cindy, 1963: The University of Texas at Austin, Bureau of Economic Geology, Report of Investigations No. 61, 54 p.

Himmelstoss, E. A., Farris, A. S., Henderson, R. E., Kratzmann, M. G., Ergul, Ayhan, Zhang, Ouya, Zichichi, J. L., Thieler, E. R., 2018, Digital Shoreline Analysis System (version 5.0): U.S. Geological Survey software release, https://code.usgs.gov/cch/dsas.

Holcombe, T. L., and Arias, C., 2009, Bathymetry of Texas-Louisiana continental shelf and coastal regions compatible with geographic information systems – bathymetry (version 2): Texas A&M University, Department of Oceanography.

LeBlanc, R. J. and Hodgson, W. D., 1959, Origin and development of the Texas shoreline: Gulf Coast Association of Geological Societies Transactions, v. 9, p. 197–220.

Leuliette, E. W., and Miller, L., 2009, Closing the sea level rise budget with altimetry, Argo, and GRACE: Geophysical Research Letters, v. 36, L04608. doi:10.1029/2008GL036010.

Leuliette, E. W. and Willis, J. K., 2011, Balancing the sea level budget: Oceanography, v. 24, no. 2, p. 122–129. doi:10.5670/oceanog.2011.32.

Lyles, S. D., Hickman, L. E., Jr., and Debaugh, H. A., Jr., 1988, Sea level variations for the United States, 1855-1986: National Ocean Service, Rockville, Maryland, 182 p.

Milliken, K. T., Anderson, J. B., and Rodriguez, A. B., 2008, A new composite Holocene sea-level curve for the northern Gulf of Mexico: in Anderson, J.B., and Rodriguez, A. B., eds., Response of Upper Gulf Coast Estuaries to Holocene Climate Change and Sea-Level Rise: Geological Society of America Special Paper 443, p. 1–11. doi: 10.1130/2008.2443(01).

Moore, L. J., 2000, Shoreline mapping techniques: Journal of Coastal Research, v. 16, no. 1, p. 111–124.

Morton, R. A., 1974, Shoreline changes on Galveston Island (Bolivar Roads to San Luis Pass), an analysis of historical changes of the Texas Gulf shoreline: The University of Texas at Austin, Bureau of Economic Geology, Geological Circular 74-2, 34 p.

Morton, R. A., 1975, Shoreline changes between Sabine Pass and Bolivar Roads: The University of Texas at Austin, Bureau of Economic Geology, Geological Circular 75-6, 43 p.

Morton, R. A., 1977, Historical shoreline changes and their causes, Texas Gulf Coast: Gulf Coast Association of Geological Societies Transactions, v. 27, p. 352–364. Reprinted as Bureau of Economic Geology Geological Circular 77-6, 13 p.

Morton, R. A., 1997, Gulf shoreline movement between Sabine Pass and the Brazos River, Texas: 1974 to 1996: The University of Texas at Austin, Bureau of Economic Geology, Geological Circular 97-3, 46 p.

Morton, R. A., Leach, M. P., and Cardoza, M. A., 1993, Monitoring beach changes using GPS surveying techniques: Journal of Coastal Research, v. 9, p. 702-720.

Morton, R. A., Miller, T. L., and Moore, L. J., 2004, National assessment of shoreline change, part 1: historical shoreline changes and associated coastal land loss along the U.S. Gulf of Mexico: U.S. Geological Survey Open-File Report 2004-1043, 42 p.

Morton, R. A., and Paine, J. G., 1985, Beach and vegetation-line changes at Galveston Island, Texas: erosion, deposition, and recovery from Hurricane Alicia: The University of Texas at Austin, Bureau of Economic Geology Geological Circular 85-5, 39 p.

Morton, R. A., and Paine, J. G., 1990, Coastal land loss in Texas: an overview: Transactions, Gulf Coast Association of Geological Societies, v. 40, p. 625-634.

Morton, R. A., Paine, J. G., and Gibeaut, J. C., 1994, Stages and durations of post-storm beach recovery, southeastern Texas coast, U.S.A.: Journal of Coastal Research, v. 10, p. 884–908.

Morton, R. A., and Pieper, M. J., 1975a, Shoreline changes on Brazos Island and South Padre Island (Mansfield Channel to mouth of the Rio Grande), an analysis of historical changes of the Texas Gulf shoreline: The University of Texas at Austin, Bureau of Economic Geology, Geological Circular 75-2, 39 p.

Morton, R. A., and Pieper, M. J., 1975b, Shoreline changes in the vicinity of the Brazos River delta (San Luis Pass to Brown Cedar Cut): The University of Texas at Austin, Bureau of Economic Geology, Geological Circular 75-4, 47 p.

Morton, R. A., and Pieper, M. J., 1976, Shoreline changes on Matagorda Island and San Jose Island (Pass Cavallo to Aransas Pass): The University of Texas at Austin, Bureau of Economic Geology, Geological Circular 76-4, 42 p.

Morton, R. A., and Pieper, M. J., 1977a, Shoreline changes on Mustang Island and North Padre Island (Aransas Pass to Yarborough Pass): The University of Texas at Austin, Bureau of Economic Geology, Geological Circular 77-1, 45 p.

Morton, R. A., and Pieper, M. J., 1977b, Shoreline changes on central Padre Island (Yarborough Pass to Mansfield Channel): The University of Texas at Austin, Bureau of Economic Geology, Geological Circular 77-2, 35 p.

Morton, R. A., Pieper, M. J., and McGowen, J. H., 1976, Shoreline changes on Matagorda Peninsula (Brown Cedar Cut to Pass Cavallo): The University of Texas at Austin, Bureau of Economic Geology, Geological Circular 76-6, 37 p.

Nerem, R. S., Beckley, B. D., Fasullo, J. T., Hamlington, B. D., Masters, D., and Mitchum, G. T., 2018, Climate-change-driven accelerated sea-level rise detected in the altimeter era:

Proceedings of the National Academy of Sciences of the United States of America, v. 115, no. 9, p. 2022-2025. doi: 10.1073/pnas.1717312115.

Paine, J. G., 1991, Late Quaternary depositional units, sea level, and vertical movement along the central Texas coast: Ph. D. dissertation, University of Texas at Austin, Austin, Texas, 256 p.

Paine, J. G., 1993, Subsidence of the Texas coast: inferences from historical and late Pleistocene sea levels: Tectonophysics, v. 222, p. 445–458.

Paine, J. G., Caudle, T., and Andrews, J., 2013, Shoreline, beach, and dune morphodynamics, Texas Gulf coast: The University of Texas at Austin, Bureau of Economic Geology, Final Report prepared for General Land Office under contract no. 09-242-000-3789, 64 p.

Paine, J. G., Caudle, T., and Andrews, J., 2014, Shoreline movement along the Texas Gulf coast, 1930’s to 2012: The University of Texas at Austin, Bureau of Economic Geology, Final Report prepared for General Land Office under contract no. 09-074-000, 52 p. + CD-ROM.

Paine, J. G., Caudle, T., and Andrews, J. R., 2016, Shoreline movement in the Copano, San Antonio, and Matagorda Bay systems, central Texas coast, 1930s to 2010s: The University of Texas at Austin, Bureau of Economic Geology, Final Report prepared for General Land Office under contract no. 13-258-000-7485, 72 p.

Paine, J. G., Caudle, T., and Andrews, J. R., 2017, Shoreline and sand storage dynamics from annual airborne lidar surveys, Texas Gulf Coast: Journal of Coastal Research, v. 33, no. 3, p. 487–506. DOI: #10.2112/JCOASTRES-D-15-00241.1.

Paine, J. G., Mathew, S., and Caudle, T., 2011, Texas Gulf shoreline change rates through 2007: The University of Texas at Austin, Bureau of Economic Geology, Report prepared under General Land Office contract no. 10-041-000-3737 and National Oceanic and Atmospheric Administration award no. NA09NOS4190165, 38 p. + CD-ROM.

Paine, J. G., Mathew, S., and Caudle, T., 2012, Historical shoreline change through 2007, Texas Gulf coast: rates, contributing causes, and Holocene context: GCAGS Journal, v. 1, p. 13-26.

Paine, J. G., and Morton, R. A., 1989, Shoreline and vegetation-line movement, Texas Gulf Coast, 1974 to 1982: The University of Texas at Austin, Bureau of Economic Geology Geological Circular 89-1, 50 p.

Peltier, W. R., and Tushingham, A. M., 1989, Global sea level rise and the greenhouse effect: might they be connected?: Science, v. 44, p. 806-810.

Penland, S., and Ramsey, K., 1990, Sea-level rise in Louisiana and the Gulf of Mexico: 1908-1988: Journal of Coastal Research, v. 6, no. 2, p. 323–342.

Price, W. A., 1956, Hurricanes affecting the coast of Texas from Galveston to the Rio Grande: U.S. Army Corps of Engineers, Beach Erosion Board, Technical Memorandum No. 78, 35 p.

Roth, D., 2010, Texas hurricane history: National Weather Service, Camp Springs, Maryland, 83 p. http://origin.hpc.ncep.noaa.gov/research/txhur.pdf

Shalowitz, A. L., 1964, Shore and beach boundaries: U.S. Department of Commerce, Publication 10-1, 749 p.

Shepard, F. P., 1960, Rise of sea level along northwest Gulf of Mexico: in Shepard, F. P., Phleger, F. B., and van Andel, T.H., eds., Recent Sediments, Northwest Gulf of Mexico: Tulsa, Oklahoma, American Association of Petroleum Geologists, pp. 338–344.

Simpson, R. H., and Riehl, H., 1981, The hurricane and its impact: Baton Rouge, Louisiana State University Press, 398 p.

Snay, R., Cline, M., Dillinger, W., Foote, R., Hilla, S., Kass, W., Ray, J., Rohde, J., Sella, G., and Soler, T., 2007, Using global positioning system-derived crustal velocities to estimate rates of absolute sea level change from North American tide gauge records: Journal of Geophysical Research, v. 112, B04409, 11 p. doi: 10.1029/2006JB004606.

Swanson, R. L., and Thurlow, C. I, 1973, Recent subsidence rates along the Texas and Louisiana coast as determined from tide measurements: Journal of Geophysical Research, v. 78, p. 2665–2671.

U.S. Army Corps of Engineers, 2017, 2016 USACE NCMP topobathy lidar DEM: Gulf Coast (TX), Joint Airborne Lidar Bathymetry Technical Center of Expertise (JALBTCX), Charleston, SC.

APPENDIX A: 2019 AIRBORNE LIDAR AND IMAGERY SURVEY

Researchers from the Bureau of Economic Geology (Bureau) acquired high-resolution airborne lidar data of the Texas Gulf coast on 11 days between April 2, 2019 and June 2, 2019. Data were collected using the Bureau's airborne lidar and imagery system (Chiroptera, fig. A1), which can collect topographic lidar data, shallow bathymetric lidar data, and high-resolution imagery simultaneously. The topographic lidar scanner operates at a wavelength of 1 µm, a pulse rate as high as 400 kHz, and an incident angle (from vertical) of 28 to 40 degrees. It can operate to a maximum height of about 1,500 m (5,000 ft), allowing the system to be used to rapidly scan large areas with a range accuracy of about 2 cm over a flat target. The bathymetric lidar scanner operates at a shorter wavelength (0.515 µm) and a lower pulse rate (35 kHz). The shorter wavelength allows the laser to penetrate water of reasonable clarity. After the laser reflects off the bottom surface and back to the source, the transit-time difference between water-surface and water bottom reflections can be used to determine water depths to a flat-bottom accuracy of about 15 cm (6 in). Also mounted in the Chiroptera chassis is a Hasselblad DigiCAM 50 megapixel natural color (RGB) camera that acquires frame images at a resolution of 8,176 by 6,132 pixels.

Figure A1. The Bureau's Chiroptera airborne lidar and imagery system. The system was built for the Bureau by Airborne Hydrography AB and delivered in 2012.

Acquisition of topographic lidar data over a swath along the Texas Gulf of Mexico beach and dune system, bathymetric lidar data over a swath along the Gulf of Mexico shoreline and two nearshore areas, and topographic and bathymetric lidar data at five beaches in Corpus Christi, Aransas, and Matagorda Bays (fig. 4) were the principal objectives of this project. Aerial imagery was acquired for reference and interpretational purposes.

We acquired two higher-altitude topographic laser swaths along the 590 km (367 mi) of Texas Gulf shoreline from the beach landward across the dunes, and two lower-altitude bathymetric laser swaths from the beach seaward a few hundred meters into shallow water. The bathymetric survey areas extended farther seaward along GLO's two 10-km-long segments of special interest at southern Padre Island (to about 1,500 m [5,000 ft] offshore) and at Surfside (to about 3,500 m [11,500 ft] offshore). Two lower-altitude passes were conducted at five bay beaches: University Beach, North Beach, and McGee Beach in Corpus Christi Bay; Rockport Beach in Aransas Bay; and Indianola Beach in Matagorda Bay (fig. 4).

Airborne lidar data and supplemental RGB imagery were acquired during several deployments between April 2 and June 2, 2019 (table A1) using a single-engine Cessna Stationaire 206 aircraft (tail number N147TX) owned and operated by the Texas Department of Transportation (TxDOT). The aircraft was flown from the following coastal Texas airports: Corpus Christi, Rockport, Bay City, Angleton, Galveston, Harlingen, Laguna Vista, and Port Arthur. Middle Texas coast survey areas (mouth of the Colorado River to the northern boundary of Padre Island National Seashore) were flown on April 2-4 and April 8 (MTC, table A1). Upper Texas coast survey areas (Sabine Pass to the mouth of the Colorado River) were flown on April 8-9, May 16, and June 2 (UTC, table A1). South Texas coastal areas (northern boundary of Padre Island National Seashore to the Rio Grande) were flown on April 16, 18, and 19 (STC, table A1).

Extended bathymetric surveys were conducted at Surfside beach on April 11, 2019 (fig. 4 and table A1) and southern Padre Island April 19, 2019 (fig. 4 and table A1). Rockport Beach was

Table A1. Flight dates, survey areas flown, and GPS base stations used for the 2019 airborne lidar survey of the Texas coast.

Date	Flight #	Airport	Location	GPS Base Stations
4/2/2019	1	Corpus/Rockport	MTC	txcc, txpo, txpv, txrt
	2	Corpus/Rockport	MTC	txcc, txpo, txpv, txrt
4/3/2019	1	Corpus	MTC	txcc, txpo, txrt
4/4/2019	1	Corpus/Rockport	MTC/bay beach	txcc, txpo, txpv, txrt
	2	Rockport/Austin	MTC	txcc, txpo, txpv, txrt
4/8/2019	1	Bay City	MTC	txbc, txpv, mata
	2	Bay City	MTC/bay beach/ UTC	txbc, txpv, mata
	3	Bay City	UTC	txag, txbc, mata
4/9/2019	1	Bay City/Angelton	UTC	txag, txbc, mata
	2	Angelton/Galveston	UTC	txag, txlm, txga
4/11/2019	1	Galveston/Angelton	Surfside offshore	txag, txlm, txga
	2	Angelton/Galveston	Surfside offshore	txag, txlm, txga
4/16/2019	1	Harlingen	STC	ptmn, txrv, txln, txbv
4/18/2019	1	Harlingen/Laguna Vista	STC	ptmn, txrv, txln, txbv
	2	Laguna Vista/Harlingen	STC	ptmn, txrv, txln, txbv
4/19/2019	1	Harlingen	STC	ptmn, txrv, txln, txbv
	2	Harlingen	SPI offshore	ptmn, txrv, txln, txbv
5/16/2019	1	Austin/Port Arthur	UTC	txlm, txga, txac, txpt
	2	Port Arthur/Galveston	UTC	txlm, txga, txac, txpt
6/2/2019	1	Austin/Galveston	bay beach/UTC	txcc, txpo, txag, txlm, txga
	2	Galveston/Austin	UTC	txag, txlm, txga

surveyed during the April 4th flight, Indianola Beach on April 8th, and the Corpus Christi Bay beaches (University, North, and McGee) on June 2, 2019 (table A1).

Flight elevations averaging 750 m (2,460 ft) above ground level and a topographic laser pulse rate of 150 kHz were used for topographic lidar data collection along the 590 km (367 mi) of Texas Gulf shoreline. Bathymetric lidar data collection flights along the Gulf of Mexico nearshore, southern Padre Island and Surfside special interest areas, and bay beaches were flown at 400 m (1,300 ft) above ground level using a topographic laser pulse rate of 250 kHz and a bathymetric laser pulse rate of 35 kHz.

Thirteen Continuously Operating Reference Stations (CORS) were used during the lidar surveys (fig. 4) for differential corrections. TxDOT set the following stations to record data at a 1-second interval during the survey: Anahuac (txac), Angleton (txag), Bay City (txbc), Brownsville (txbv), Corpus Christi (txcc), Galveston (txga), La Marque (txlm), Laguna Vista (txln), Port Aransas (txpo), Port Arthur (txpt), Port Lavaca (txpv), Rockport (txrt), and Raymondville (txrv). These stations typically record data at a 15- or 30-second intervals. GPS base stations (Trimble Net R9 receivers and antennas) recording at a 1-second interval were deployed at Matagorda Bay Nature Park (mata) and Port Mansfield (ptmn) for additional GPS ground control in areas too distant from CORS receivers. At least three base stations were used to process data during each flight (Table A1).

APPENDIX B: SELECTED NOURISHMENT AND RESTORATION PROJECTS

Coastal staff at the General Land Office provided a partial list (table B1) of beach nourishment, dune restoration, and nearshore dredge material placement (NS) projects. Approximate locations of these projects are shown on maps of the upper coast between Sabine Pass and Rollover Pass (fig. B1), the upper middle coast between San Luis Pass and Pass Cavallo (fig. B2), the lower middle coast between Pass Cavallo and Packery Channel (fig. B3), and the lower coast between Packery Channel and the Rio Grande (fig. B4).

Table B1. Partial list of beach nourishment, dune restoration, and nearshore dredge material placement projects along the Texas Gulf of Mexico shoreline. Locations are shown by ID (figs. B1 to B4). Data from the General Land Office.

Map ID	Project	Name	County	Type	Year	Length (ft)	Volume (yd^3)
1	CEPRA 1175	Quintana BN (Bryan Beach)	Brazoria	BN	2005	1,846	168,500
2	CEPRA 1571	Bryan Beach BMMP BN	Brazoria	BN	2016	1,700	36,000
3	CEPRA 1529	CR257 Dune Restoration	Brazoria	DR	2017	6,817	13,950
4	CEPRA 1529	CR257 Dune Restoration	Brazoria	DR	2017	9,875	
5	CEPRA 1529	CR257 Dune Restoration	Brazoria	DR	2017	5,456	
6	CEPRA 1529	CR257 Dune Restoration	Brazoria	DR	2017	5,559	
7	CEPRA 1175	Quintana BN (Cortez Beach)	Brazoria	BN	2005	2,000	101,700
8	CEPRA 1154	Quintana Dune Restoration (Cortez Beach)	Brazoria	DR	2003	2,467	
9	CEPRA 1154	Quintana Dune Restoration (Bryan Beach)	Brazoria	DR	2003	1,792	
9	CEPRA 1154	Quintana Dune Restoration (Bryan Beach)	Brazoria	DR	2003	1,792	
10	CEPRA 1015	Surfside BN	Brazoria	BN	2001	4,780	80,000
11	CEPRA 1109	Surfside BN (Claudette)	Brazoria	BN	2003	4,780	37,181
12	CEPRA 1229	Surfside BN	Brazoria	BN	2006	4,780	950
13	CEPRA 1471	Surfside Shoreline Stabilization	Brazoria	BN	2009	4,780	27,000
14	CEPRA 1511	Surfside Emergency BN	Brazoria	BN	2011	4,500	210,000
15	CEPRA 1570	Surfside BMMP BN	Brazoria	BN	2015	1,964	98,270
16	CEPRA 1010	South Padre Island BN	Cameron	BN	2000	3,200	370,000
17	CEPRA 1053	South Padre Island BN-Park Road 100	Cameron	BN	2002	2,800	13,665
18	CEPRA 1107	South Padre Island BN-Park Road 100	Cameron	BN	2003	2,000	120,000
19	CEPRA 1115	South Padre Island BN	Cameron	BN	2002	3,400	331,031
20	CEPRA 1165A	South Padre Island BN	Cameron	BN	2005	2,100	49,037
21	CEPRA 1165B	South Padre Island BN	Cameron	BN	2005	3,100	228,960
22	CEPRA 1209A	South Padre Island BN	Cameron	BN	2006	1,400	65,400

Map ID	Project	Name	County	Type	Year	Length (ft)	Volume (yd^3)
23	CEPRA 1209B	South Padre Island BN	Cameron	BN	2006	3,750	261,600
24	CEPRA 1233	South Padre Island BN	Cameron	BN	2007	8,000	71,045
25	CEPRA 1355	South Padre Island BN-Park Road 100	Cameron	BN	2008	2,500	100,216
26	CEPRA 1356	South Padre Island BN	Cameron	BN	2009	4,700	406,825
27	CEPRA 1453	South Padre Island BN	Cameron	BN	2010	2,800	92,000
28	CEPRA 1456	South Padre Island BN	Cameron	BN	2010	3,000	130,000
29	CEPRA 1524?	South Padre Island BN	Cameron	BN	2012	2,500	210,000
30	CEPRA 1525?	Isla Blanca Park BN	Cameron	BN	2012	1,500	140,000
31	USACE 1997	SPI USACE 1997	Cameron	BN	1997	6,000	490,000
32	USACE 1999	SPI USACE 1999	Cameron	BN	1999	4,000	494,766
33	USACE 2011	SPI USACE 2011	Cameron	BN	2011	2,700	368,000
34	USACE 2011	SPI USACE Isla Blanca	Cameron	BN	2011	1,500	199,000
35	USACE 2015	SPI USACE 2015	Cameron	BN	2015	1,800	324,344
36	USACE 2016	SPI USACE 2016	Cameron	BN	2016	2,400	361,027
37	CEPRA 1037	Gilchrist BN	Galveston	BN	2000	5,280	300,000
38	CEPRA 1039A	GIWW Rollover Bay Reach BN FY00	Galveston	BN	2000	3,000	138,400
39	CEPRA 1039B	GIWW Rollover Bay Reach BN FY01	Galveston	BN	2001	3,000	126,000
40	CEPRA 1086	Caplen Beach Dune Restoration	Galveston	DR	2004	750	5,000
41	CEPRA 1112A	Rollover Pass BUDM 2002	Galveston	BN	2002	3,000	119,000
42	CEPRA 1112B	Rollover Pass BUDM 2003	Galveston	BN	2003	1,400	104,000
43	CEPRA 1276	Rollover Pass BUDM	Galveston	BN	2006	3,000	185,646
44	CEPRA 1400	Rollover Pass BUDM	Galveston	BN	2008	3,000	134,716
45	CEPRA 1494	Rollover Pass BUDM	Galveston	BN	2010	300	176,755
46	CEPRA 1519	GIWW Rollover Bay Reach BN	Galveston	BN	2012	1,200	105,000
47	CEPRA 1584	GIWW Rollover Bay Reach BN	Galveston	BN	2014	3,000	173,000
48	CEPRA 1584	GIWW Rollover Bay Reach BN	Galveston	BN	2015	3,000	171,000
49	CEPRA 1608	GIWW Rollover Bay Reach BN	Galveston	BN	2016	3,000	194,000
50	CEPRA 1608?	GIWW Rollover Bay Reach BN	Galveston	BN	2018	3,000	143,217
51	CEPRA 1619	GIWW Rollover Bay Reach BN	Galveston	BN	2019	3,000	70,000
52	pre CEPRA?	1000 ft west of Rollover	Galveston	BN	1999	3,000	175,000
53	CEPRA 1087	Caplen Gilchrist Beach BN	Galveston	BN	2004	16,000	
54	CEPRA 1087	Caplen Gilchrist Beach BN	Galveston	BN	2004	16,000	110,140
55	CEPRA 1095	West Galveston Island Association 5500 BN	Galveston	BN	2004	4,400	30,984
56	CEPRA 1643	Babes Beach BN	Galveston	BN	2020	5,350	423,027
57	CEPRA 1016	Bermuda Beach BN	Galveston	BN	2001	3,050	12,140
58	CEPRA 1100	Bermuda Beach BN	Galveston	BN	2004	3,100	35,767
59	CEPRA 1521	End of Seawall BN (Dellanera)	Galveston	BN	2015	2,000	11,370
60	CEPRA 1100	Hershey Beach BN	Galveston	BN	2004	920	5,131
61	CEPRA 1313	West Galveston Rita Repair Hershey Beach	Galveston	BN	2008	920	5,171
62	CEPRA 1095	Kahala Beach	Galveston	BN	2004	1,150	8,551
63	CEPRA 1088	West Galveston Island Pirates Beach BN	Galveston	BN	2004	7,815	57,012

Map ID	Project	Name	County	Type	Year	Length (ft)	Volume (yd^3)
64	CEPRA 1016	San Luis Pointe	Galveston	BN	2001	1,311	11,077
65	CEPRA 1100	Sands of Kahala	Galveston	BN	2004	1,375	9,791
66	CEPRA 1313	Sands of Kahala	Galveston	BN	2008	1,879	13,875
67	CEPRA 1016	Sea Isle I BN	Galveston	BN	2001	2,650	6,378
68	CEPRA 1095	Sea Isle BN	Galveston	BN	2004	8,570	23,793
69	CEPRA 1016	Sea Isle II BN	Galveston	BN	2001	750	3,095
70	CEPRA 1016	Sea Isle III BN	Galveston	BN	2001	1,675	3,519
71	CEPRA 1447	Emergency BN for Galveston Seawall	Galveston	BN	2009	12,650	470,000
72	CEPRA 1566	Galveston Seawall Beach Nourishment	Galveston	BN	2017	19,400	1,200,000
73	CEPRA 1016	Spanish Grant BN	Galveston	BN	2001	1,775	5,509
74	CEPRA 1100	Spanish Grant BN	Galveston	BN	2004	1,775	29,884
75	CEPRA 1313	West Galveston Rita Repair Spanish Grant	Galveston	BN	2008	1,775	21,000
76	CEPRA 1100	Sunny Beach BN	Galveston	BN	2004	660	10,618
77	CEPRA 1313	West Galveston Rita Repair Sunny Beach	Galveston	BN	2008	660	4,500
78	CEPRA 1016	Terramar BN	Galveston	BN	2001	2,841	11,652
79	CEPRA 1095	Terramar BN	Galveston	BN	2004	2,760	8,881
80	CEPRA 1100	West Grand Riviera I&II BN	Galveston	BN	2004	460	17,531
81	CEPRA 1530	McFaddin Beach Nourishment Phase I	Jefferson	BN	2016	15,312	640,000
82	CEPRA 1003	McFaddin Dune Restoration	Jefferson	DR	2002	1,775	14,000
83	CEPRA 1532	Sargent Beach Nourishment	Matagorda	BN	2013	3,600	82,000
84	CEPRA 1113	Packery Channel BN	Nueces	BN	2005	7,000	688,000
1001	USACE	SPI DMPA Number 1	Cameron	NS	1988	5,216	220,000
1002	USACE	SPI DMPA Number 1	Cameron	NS	1991	5,216	580,000
1003	USACE	SPI DMPA Number 1	Cameron	NS	1995	5,216	750,000
1004	USACE	SPI DMPA Number 1	Cameron	NS	1997	5,216	396,000
1005	USACE	SPI DMPA Number 1	Cameron	NS	1999	5,216	195,000
1006	USACE	SPI DMPA Number 1	Cameron	NS	2002	5,216	329,000
1007	USACE	SPI DMPA Number 1	Cameron	NS	2003	5,216	356,000
1008	USACE	SPI DMPA Number 1	Cameron	NS	2006	5,216	340,000
1009	USACE	SPI DMPA Number 1	Cameron	NS	2007	5,216	443,000
1010	USACE	SPI DMPA Number 1	Cameron	NS	2008	5,216	500,000
1011	USACE	SPI DMPA Number 1	Cameron	NS	2014	5,216	305,000
1012	USACE	SPI DMPA Number 2	Cameron	NS	2018	4,984	380,460

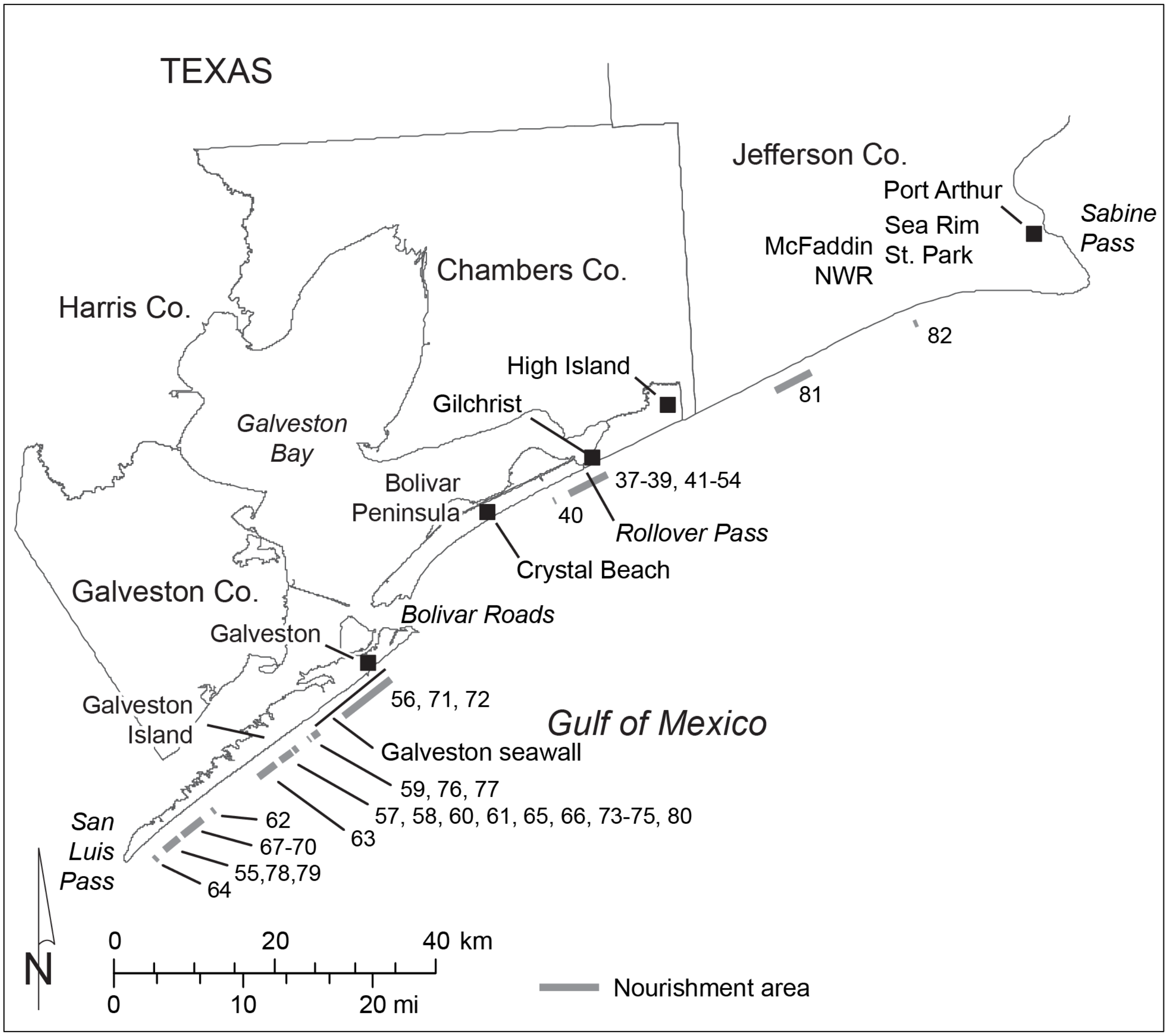

Figure B1. Locations of beach nourishment and dune restoration projects on the upper Texas coast.

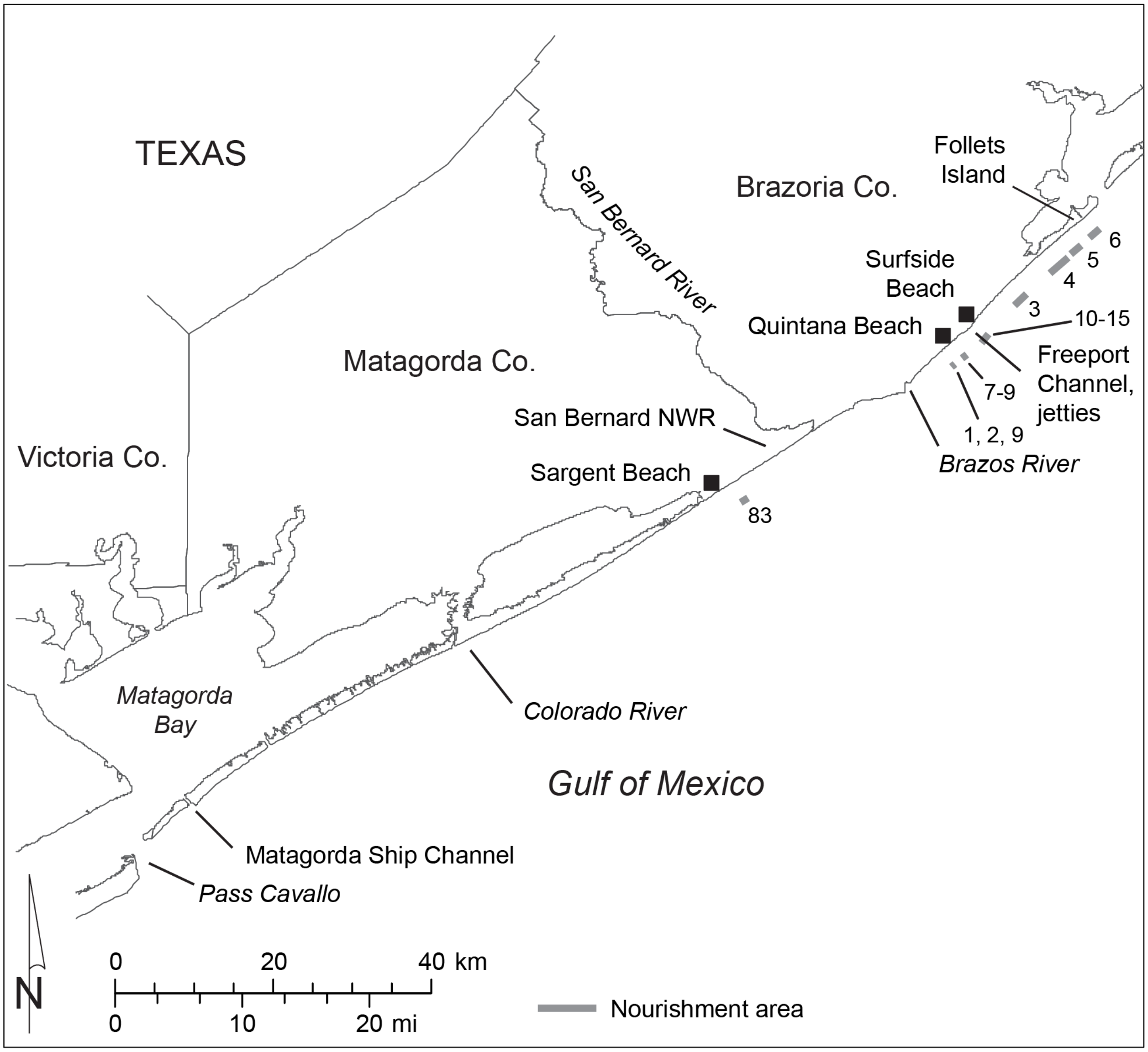

Figure B2. Locations of beach nourishment and dune restoration projects between San Luis Pass and Pass Cavallo.

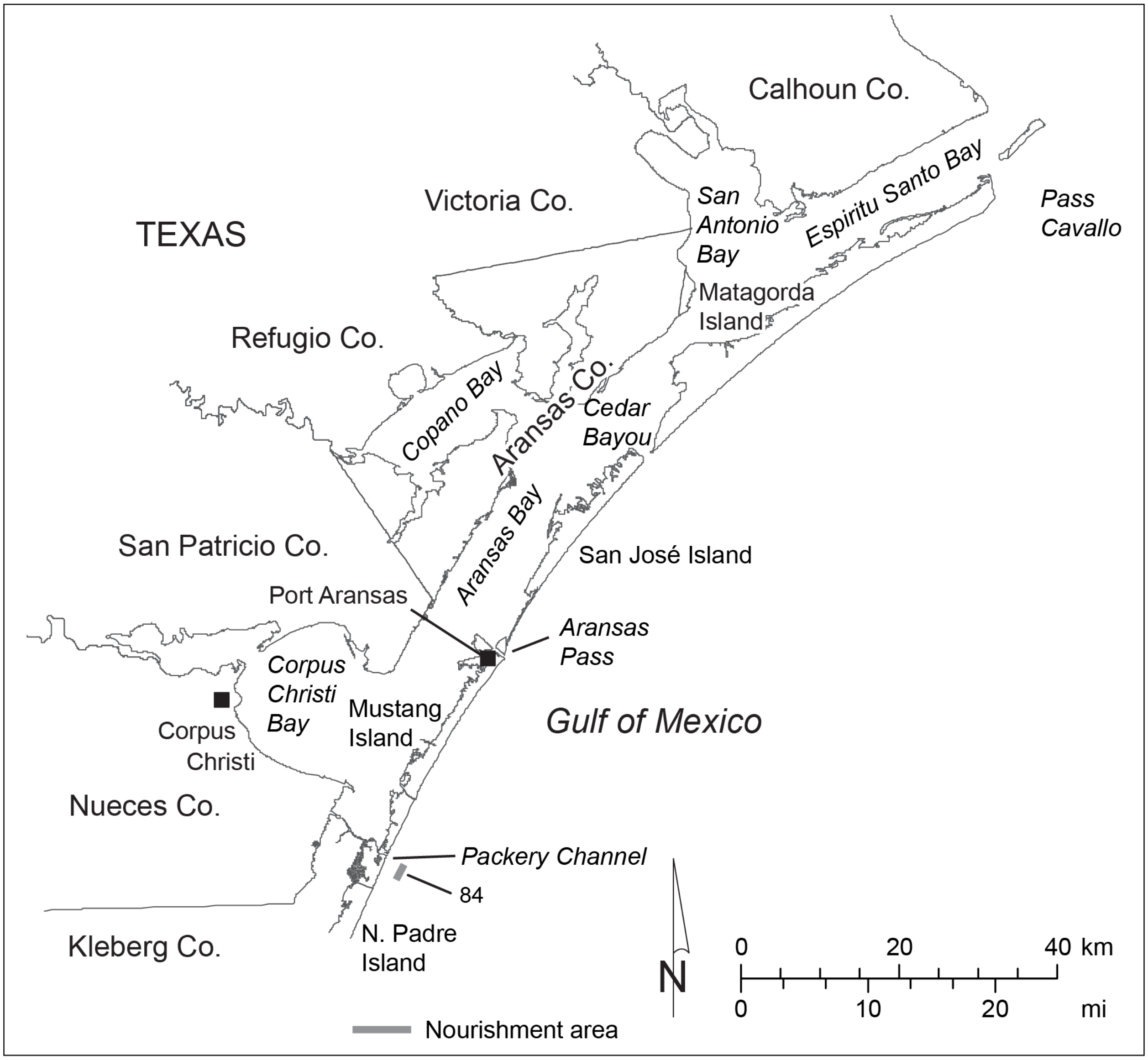

Figure B3. Locations of beach nourishment and dune restoration projects on the middle Texas coast.

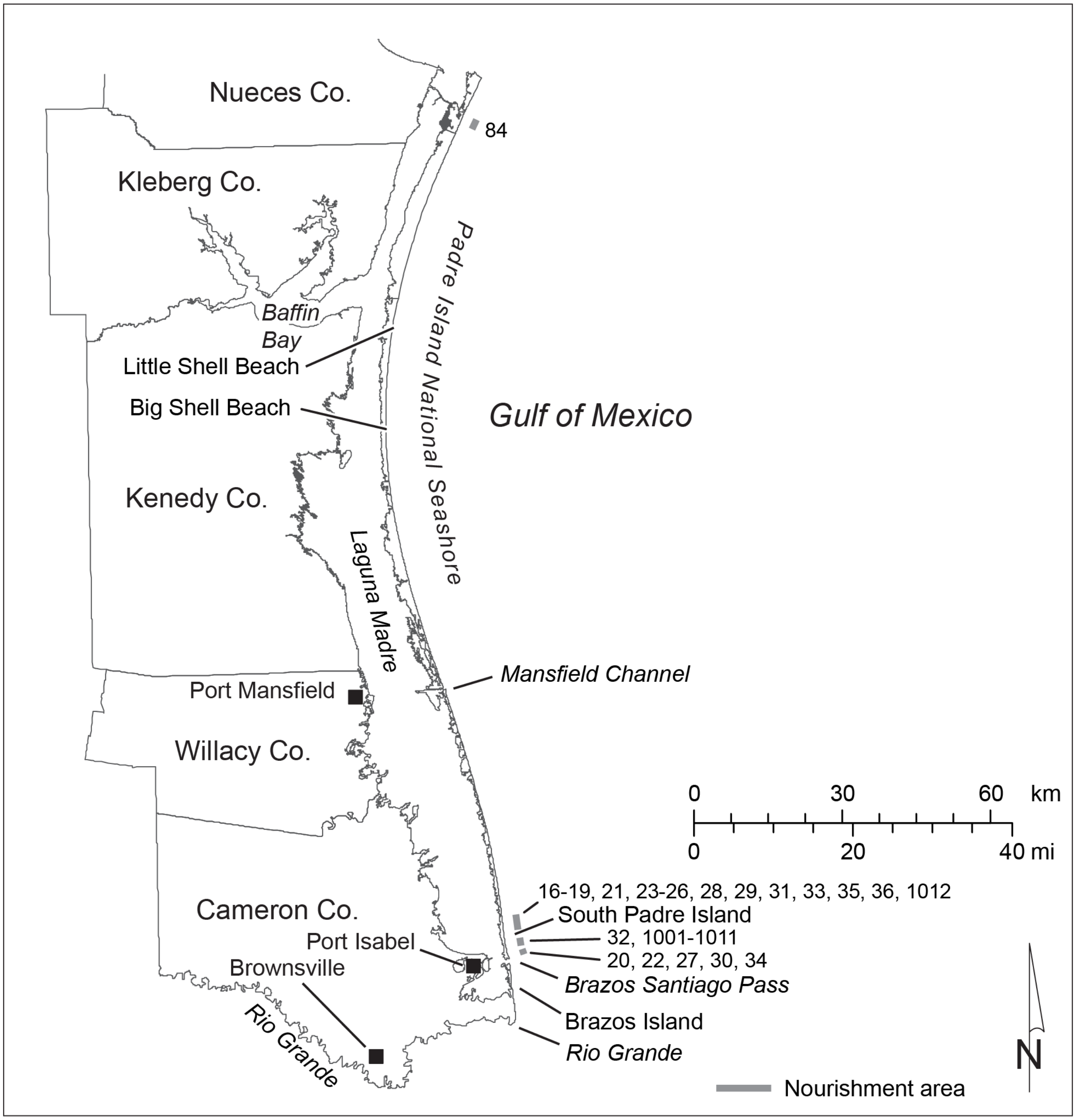

Figure B4. Locations of beach nourishment and dune restoration projects on the lower Texas coast.